Operation, Control, and Simulation of Modular Multilevel Converters with Embedded Energy Storage

by

Nuwan Madushanka Herath Herath Mudiyanselage

A thesis submitted to the Faculty of Graduate Studies of
The University of Manitoba
in partial fulfilment of the requirements for the degree of

MASTER OF SCIENCE

Department of Electrical and Computer Engineering
University of Manitoba
Winnipeg.

Copyright © 2019 by Nuwan Madushanka Herath Herath Mudiyanselage

Abstract

Modular Multilevel Converters (MMCs) with embedded storage have gained increasing appeal among researchers as a means of interconnecting energy storage into low- and medium-voltage grids (both AC and DC). A main setback regarding these converters has been their EMT simulation burden due to the complexity of the converter. This thesis presents a detailed equivalent model, which can be used to efficiently and accurately simulate MMCs with embedded storage without any loss of accuracy. Operation and control methods of these converters are also studied. The developed detailed equivalent model is validated against a detailed switching model implementation of a single phase MMC with embedded storage. An application case of the MMC with storage in a microgrid is also studied for simulation efficiency and the impact of energy storage on a network. A prototype MMC with embedded storage is also used to validate the simulation results developed from the detailed equivalent model. The thesis shows that the developed detailed equivalent model can produce accurate simulation results for MMCs with embedded storage on par with a conventional detailed switching model. The massive reduction of computing time achieved by the detailed equivalent model is validated using simulation cases for a small and large system. The waveforms obtained from a laboratory prototype setup further validate the accuracy of the detailed equivalent model.

Acknowledgments

This thesis has become a reality with the support of many individuals and organizations. I would like to pay my sincere gratitude to all of them.

First and foremost, I would like to express my gratitude to my academic advisor, Prof. Shaahin Filizadeh for the continuous guidance, encouragement, and advice given throughout my research. I would also like to convey my gratitude to Dr. Mohammad Toulabi for the valuable advice and suggestions given for my work.

Ms. Xianghua Shi is specially appreciated for consulting my hardware development and providing valuable feedback to build a working prototype.

A special thank you must be conveyed to Mr. Shrimal Koruwage, Mr. Cory Smit, and Mr. Zoran Trajkoski, for helping me with technical details in developing the prototype.

A special thank goes to Manitoba Hydro, MITACS, and NSERC for providing financial support to carry out my research.

Finally, I would like to thank my family and friends who were there to support me in numerous ways throughout my research.

Nuwan Herath

Dedication

to my

family,

teachers,

and friends.

Contents

Front Matter

Abstract……i

Acknowledgments……... ii

Dedication……...iii

Contents……..…… iv

List of Tables…….. vi

List of Figures……vii

List of Abbreviations……... x

Chapter 1: Introduction 1

1.1 Background……... 1

1.2 Problem Definition……5

1.3 Thesis Motivation…… 6

1.4 Organization of the Thesis…… 7

Chapter 2: Operating Principles of Modular Multilevel Converters with Embedded Energy Storage 8

2.1 Converter Structure……... 8

2.2 SM Structure……... 12

2.3 Operation of the Half-Bridge SM……13

2.4 Operation of the DC-DC Converter…… 16

2.5 Capacitor Voltage Balancing……...18

2.6 Converter Control Methods…….19

2.7 Converter-Grid Synchronization…….23

2.8 Summary…… 23

Chapter 3: Control and Protection of the MMC with Embedded Energy Storage 24

3.1 Active Power and AC Voltage Controller……...24

3.2 Controllers of the DC-DC Converter…….. 24

3.3 SOC Controller……27

3.4 DC Power Suppression Controller……... 29

3.5 Breaker Protection Schemes……30
3.6 Startup Procedure……31
3.7 Simulation Validation of Control and Operation……32
3.8 Summary ……37
Chapter 4: Detailed Equivalent Model of the Multivalve 38
4.1 Fundamentals of EMT Simulation……..38
4.2 EMT Model of the Battery…… 45
4.3 Derivation of the Thevenin Equivalent Circuit of a Multivalve…….48
4.4 Comparison and Validation of the Detailed Equivalent Model of MMC Multivalve… 53
4.5 Simulation of a Microgrid with an MMC with Embedded Storage……62
4.6 Summary……66
Chapter 5: Experimental Implementation and Verification 67
5.1 Parameters of the Converter……67
5.2 Half-bridge SM……... 69
5.3 Design of DC-DC converter……69
5.4 Observations from the Prototype……73
5.5 Comparison of Experimental Results with the EMT Simulation……75
5.6 Summary……79
Chapter 6: Contributions, Conclusions, and Future work 80
6.1 Contributions and Conclusions……... 80
6.2 Recommendations for Future Work……81
Appendix A 82
Appendix B 85
Appendix C 87
References 90

List of Tables

Table 3.1: Parameters of the simulated MMC……33
Table 3.2: Startup procedure time instants. ……33
Table 4.1: Parameters of the MMC with embedded storage ……...63
Table 5.1: Parameters of the experimental setup.……67
Table 5.2: DC-DC converter specifications.……69

List of Figures

Figure 1.1: Conventional battery storage grid interconnection method. ……2
Figure 1.2: Three-phase MMC structure. ……4
Figure 1.3: Popular sub-module topologies.……4
Figure 2.1: Structure of a single-phase MMC with energy storage. ……..9
Figure 2.2: (a) Model of the MMC with energy storage (b) SM with storage. ……10
Figure 2.3: SM topologies. ……12
Figure 2.4: Multilevel carriers. ……14
Figure 2.5: Nearest Level Control (NLC).……15
Figure 2.6: DC-DC converter operation. ……16
Figure 2.7: DC-DC converter waveforms.……..17
Figure 2.8: Power flow of an MMC with BESS.……20
Figure 2.9: Direct controllers.……20
Figure 2.10: Decoupled AC active power and AC voltage controller.……..22
Figure 2.11: Phase locked loop (PLL).……23
Figure 3.1: Direct controllers.……24
Figure 3.2: DC-DC converter of the SM. ……25
Figure 3.3: Current controller.……26
Figure 3.4: Voltage controller.……26
Figure 3.5: Implemented controller for the DC-DC converter.……27
Figure 3.6: Inter-arm SOC balancing controller.……29
Figure 3.7: Intra-arm SOC balancing controller.……29
Figure 3.8: DC power suppression controller.……29
Figure 3.9: AC breaker. ……30
Figure 3.10: Contactor on the DC-DC converter.……..31
Figure 3.11: Startup procedure. ……..31
Figure 3.12: AC power variation during startup.……...34
Figure 3.13: AC bus rms voltage during startup..……...34
Figure 3.14: AC line current during startup.……..34

Figure 3.15: Capacitor voltages during startup…..…….…….…….35
Figure 3.16: Battery currents during startup.……..…….…….…….35
Figure 3.17: Variation of SOC of top and bottom SMs.…….…….……..36
Figure 3.18: Power distribution of the converter.…….…….36
Figure 4.1: Representation of resistor.…….…….…….38
Figure 4.2: Representation of an inductor.…….…….……...39
Figure 4.3: Representation of a capacitor. …….…….……...41
Figure 4.4: MOSFET with an anti-parallel diode.…….…….……...42
Figure 4.5: State transition diagram for a MOSFET.…….……43
Figure 4.6: Example network.…….…….…….…….43
Figure 4.7: Admittance circuit of the example network. ……...…….……...44
Figure 4.8: Typical battery discharge curve. …….…….……...46
Figure 4.9: Battery discharge curve.…….…….…….……...47
Figure 4.10: Half-bridge SM with storage.…….…….……..49
Figure 4.11: EMT equivalent SM.…….…….…….……..49
Figure 4.12: SM with only the resistances to calculate Thevenin resistance.……49
Figure 4.13: Thevenin equivalent circuit of a multivalve.…….……51
Figure 4.14: Comparison at steady state.…….…….…….54
Figure 4.15: Comparison of average capacitor voltages at steady state. ……...55
Figure 4.16: Comparison at power reference change. …….……..56
Figure 4.17: Comparison of average capacitor voltages when power reference change.……..57
Figure 4.18: Comparison of average battery current when power reference change. ……...57
Figure 4.19: Comparison at line-to-ground fault.…….…….……58
Figure 4.20: Comparison of average capacitor voltages during line-to-ground fault.……...58
Figure 4.21: Comparison of average battery current during a line-to-ground fault.……..59
Figure 4.22: Comparison when fault is at the middle of multivalve. ……60
Figure 4.23: Capacitor voltages during a fault in the middle of the multivalve.……...60
Figure 4.24: Battery currents during a fault in the middle of the multivalve. ……...61
Figure 4.25: IEEE 34 bus system with the proposed MMC with BESS and switchable load.…..62
Figure 4.26: Bus voltage at load energization. …….…….……64

Figure 4.27: Power and voltage when the power reference is changed.……65
Figure 5.1: Schematic diagram of the prototype……68
Figure 5.2: Prototype setup…….…….…….…….68
Figure 5.3: Half-bridge SM…….…….…….…….69
Figure 5.4: DC-DC converter. …….…….…….…….71
Figure 5.5: Diode voltages.…….…….…….…….72
Figure 5.6: SM with the snubbers installed. …….…….……73
Figure 5.7: MMC ac voltage, load voltage and load current. …….……...74
Figure 5.8: MMC ac voltage, load voltage and top arm current.……...74
Figure 5.9: MMC ac voltage, load voltage and bottom arm current.…….74
Figure 5.10: Capacitor voltages. …….…….…….……75
Figure 5.11: Battery currents. …….…….…….…….75
Figure 5.12: Comparison of experimental setup with simulation model.……..77
Figure 5.13: Comparison of average capacitor voltages.…….…..……78
Figure 5.14: Comparison of battery currents.…….…….…..…….78
Figure A.1: Two states of the DC-DC converter.…….…….82

List of Abbreviations

AC	alternating current
APOD	alternate phase opposition disposition
BESS	battery energy storage system
CCM	continuous conduction mode
CPU	central processing unit
DC	direct current
EMT	electro-magnetic transient
FP	firing pulse
HVDC	high voltage direct current
IGBT	insulated gate bipolar transistor
LG	line to ground
LV	low voltage
MMC	modular multilevel converter
MOSFET	metal oxide semiconductor field effect transistor
MV	medium voltage
NiMH	Nickel-metal hydride
NLC	nearest level control
PCB	printed circuit board
PCC	point of common coupling
PD	phase disposition
PI	proportional integral
PLL	Phase locked loop
POD	phase opposition disposition
PWM	pulse width modulation
RC	resistor capacitor
RMS	root mean square
SM	sub module
SOC	state of charge
VSC	voltage source converter

Chapter 1: Introduction

1.1 Background

Since the beginning of commercial electrical power usage, power systems have been mainly dominated by grid-synchronized synchronous generators to provide power. Hydro, steam, and gas turbines have been the main prime movers, and they continue to be dominant to date [1]. Conventional generators with their turbines present large amounts of inertial mass, thus making primarily slow transients when disturbed. However, with growing concerns over protecting the environment, many governments and electrical companies around the world have started to take an interest in renewable energy sources. Increasingly, solar and wind energy systems are entering the electrical systems throughout the world [2]. Although solar and wind energy is freely available to harness, they are highly intermittent [3], [4]. Solar radiation on a given solar farm varies throughout the day. Wind speeds in a wind farm can also vary over a large range within a short period of time [5]. Additionally, renewable energy sources such as solar PV-based plants do not contain much inertia [6]. Thus, they do not provide any inherent means to dampen the transients occurring in power systems. These issues can be solved by incorporating energy storage in the electrical grid as energy storage is able to store additional generation during off-peak hours, provide a smooth power output to the grid during peak hours, and emulate inertia.

The electrical load on the electrical grid varies with the time of day. This is known as the daily load pattern. In most power systems, there is a high demand in the morning followed by a nearly constant (and low) load during the day. A high peak occurs at evening and a small load is observed during the night. This large variation of power demand is hard to handle with generation

in coal and nuclear power dominated electrical networks. Coal and nuclear plants operate at their peak efficiency when they operate at their rated power and they cannot ramp power up or down rapidly. Energy storage can be used in this kind of electrical grids to provide power during hours of high power demand and absorb excess power available in the grid during off-peak hours. This will allow base load generation sources to provide power at their peak efficiency [7].

Providing electrical power to rural communities has been a challenge to many utilities. Very long transmission lines are required to provide this power, and they are highly likely to be affected by various environmental causes. Remote communities tend to have local generation sources such as diesel-powered generation or solar PV power and/or wind generation. Proper introduction of energy storage can manage the local generation sources to provide continuous power [8], [9] with minimal adverse impact from polluting diesel generation. Energy storage could also gain some time for the maintenance groups to attend to a breakdown as well.

It has been made clear that energy storage in the electrical grid can make a vital difference to the performance of the network. However, the method and interface of energy storage also play vital roles. The most basic method of energy storage interface is shown in Figure 1.1 [10].

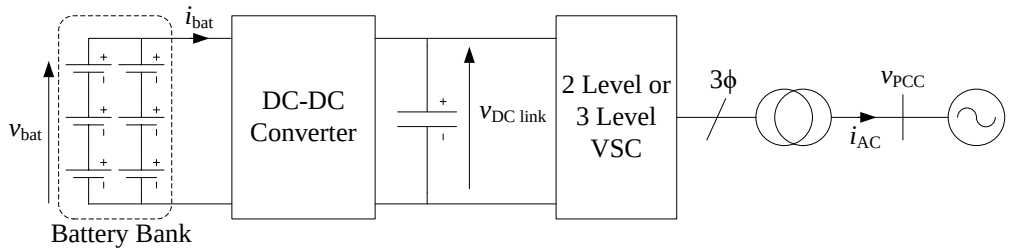


Figure 1.1: Conventional battery storage grid interconnection method.

The conventional method shown in Figure 1.1 has some distinct disadvantages. Long strings of batteries are connected in series to obtain the high DC voltage. Voltage distribution throughout the battery string may be uneven due to internal resistance of batteries and thus uneven

charging/discharging of batteries may occur resulting uneven aging [11]. A DC-DC converter is used to step up the battery voltage and maintain the DC link voltage. Operation of the DC-DC converter introduces additional power losses to the system. A two-level or three-level voltage source converter (VSC) is used to invert the DC power into AC. The output voltage waveform has mainly two or three levels in this kind of converters. Pulse-Width Modulation (PWM) switching techniques are used to generate an output following a sinusoidal waveform. However, these switchings introduce large amounts of high-frequency harmonics into the electrical system. Before connecting to the grid, these harmonics must be captured using appropriate filters. Usage of filters introduces more cost to the energy storage unit with additional requirements for space and maintenance.

To address the issues with the conventional method, researchers have taken an interest in Modular Multilevel Converter (MMC) structures. MMCs were initially introduced as a VSC for high voltage DC (HVDC) transmission [12]. The basic structure of an MMC is shown in Figure 1.2. A three-phase MMC consists of three phase-legs, and each phase leg consists of two multivalves and two arm inductors. A multivalve is a series-connected array of Sub-Modules (SM). A regular MMC SM has a capacitor parallel to a half-bridge switch setting, which allows to insert or bypass the capacitor from the multivalve (see Figure 1.3(a)).

In this thesis, the MMC in Figure 1.2 is changed to include energy storage units. A battery is connected to each SM capacitor via a DC-DC converter (see Figure 1.3(b)) [13]-[15]. This kind of MMC is called an MMC with embedded energy storage. A DC-DC converter is used to control the capacitor voltage of each SM. The same DC-DC converter can be used to control the charging/discharging currents of the batteries using additional control loops.

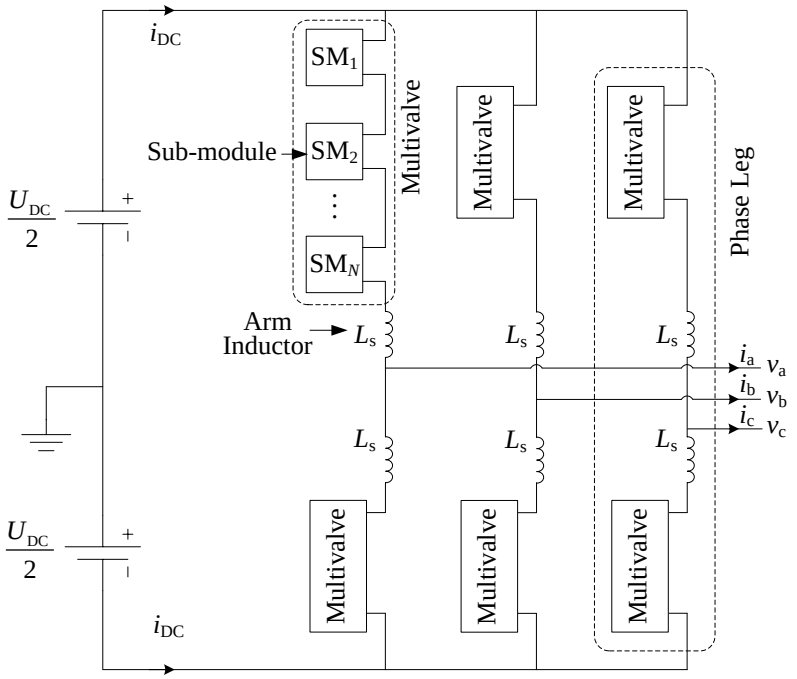


Figure 1.2: Three-phase MMC structure.

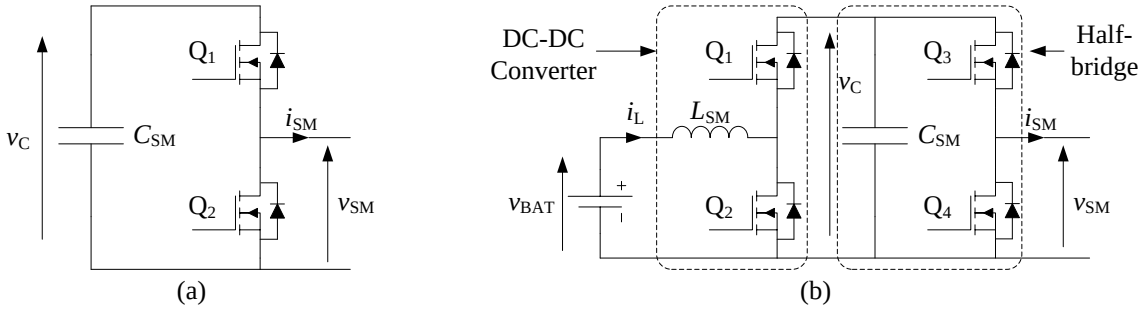


Figure 1.3: Popular sub-module topologies (a) half-bridge sub-module used in regular MMC (b) half-bridge sub-module with a connected DC-DC converter used in MMCs with energy storage.

This MMC topology allows distributing the battery bank into several small units at the SM level, thus reducing the voltage of the battery string and increasing controllability of charging and discharging of individual battery strings. This enhances the performance and lifetime of batteries as well. The AC output of the MMC has multiple steps and, therefore, the resulting harmonic contents are quite low. This enables efficient power transfer from batteries while removing expensive line filters. The MMC also has a DC link that enables the interconnection of

a DC and AC grid via a single converter. This kind of implementation is a main consideration in shipboard power systems [16], [17].

1.2 Problem Definition

Studies regarding conventional MMCs and MMCs with energy storage are mainly done using computer simulations. Since an MMC contains a large number of SMs and thus a large number of switching components, to study the operation of the converter researchers tend to use average-value models to reduce the computational burden of simulations. However average-value models are not sufficient to observe the behavior of the converter during a fault, control error, or other abnormal events. They do not provide detailed observations such as individual capacitor voltages, battery currents, switch currents, etc., which are essential in the converter design process. Electro-Magnetic Transient (EMT) simulations with detailed models need to be used to observe these kinds of behavior.

EMT simulations rely on viewing the electrical system as a combination of current sources and admittances. An MMC with energy storage has a large number of sub-modules in a phase arm, but normally not as many as in a conventional MMC in HVDC applications, as MMCs with embedded storage are generally connected to the medium voltage (MV) or low voltage (LV) power system. The EMT simulator has to convert all the switches (IGBTs and diodes), capacitors, and voltage sources, etc., in the MMC into an admittance network and solve for node voltages (this method of simulation is denoted as detailed switching model in this thesis). This will generate a large network and thus a large admittance matrix. Every time a switch operates, the EMT simulator reforms the admittance matrix and re-inverts it to solve for node voltages. In an MMC with energy storage, the DC-DC converters used to connect batteries operate at a frequency of few kHz. Thus,

the EMT solver needs to re-triangularize the admittance matrix a large number of times. This will require an immense amount of computation power and time. It will make the converter and controller design process a challenging task.

It is, therefore, clear that there is a need for an efficient simulation model for MMCs with energy storage. This thesis proposes a detailed equivalent model for an MMC multivalve with energy storage inspired by the work done in [18]. The new model proposes a Thevenin equivalent model for an MMC multivalve with energy storage without losing any information already available in a detailed EMT switching model.

This thesis also concentrates on an experimental MMC with energy storage. A small-scale prototype was developed in the lab. It is used to validate the detailed equivalent EMT simulation model as well as the operation of the MMC with a battery energy storage system (BESS).

1.3 Thesis Motivation

MMCs with energy storage have been a major improvement in the integration of battery energy storage into the grid. Their flexibility, voltage and power quality, and battery management are qualities that cannot be found in normal two-level and three-level VSC systems. This provided motivation to study the operation of such converters that can be used to deal with intermittencies of renewable energy generation, load leveling, etc. Study of this type of converters requires detailed EMT simulations. However, detailed switching modeling of such converters is tedious, slow, and inefficient. As a solution, a detailed equivalent model is developed. This model provides the same simulation results as a detailed switching EMT solver with a reduced computational load. Since the model does not lose any information available in a detailed EMT switching model, it is

named a “detailed equivalent model”. In this thesis, PSCAD/EMTDC EMT solver is used to implement the model. The development of a detailed equivalent model motivated verification of its performance using an experimental prototype MMC with the energy storage.

1.4 Organization of the Thesis

The thesis is organized as follows:

Chapter 2 introduces the principles of operation of MMCs with energy storage. A model of the MMC with energy storage will be presented as well. Chapter 3 concentrates on the control and protection of the MMC with energy storage and discusses a converter startup procedure. Chapter 4 develops a detailed equivalent model for the MMC multivalve with energy storage. The detailed equivalent model is compared with an example detailed switching simulation case developed in PSCAD/EMTDC. Connection of a three-phase MMC into a microgid is also studied for the comparison of simulation speed and impact on the network by energy storage. Chapter 5 presents experimental results obtained from the developed experimental MMC setup and compares the obtained results with the simulated detailed equivalent model. Chapter 6 concludes the thesis by discussing the contributions and conclusions, and proposes topics for future research.

Chapter 2: Operating Principles of Modular Multilevel Converters with Embedded Energy Storage

MMCs with energy storage share nearly the same converter structure with a regular MMC except for the energy storage interconnections to its SMs. This chapter will present in detail and analyze the converter structure and operation of MMCs with energy storage. A single-phase MMC is used for ease of understanding.

2.1 Converter Structure

Error! Reference source not found. shows a single-phase MMC with energy storage. A phase consists of two phase arms. Each arm conventionally has the same number (N) of SMs and they are connected in series. The two phase arms are interconnected using two arm inductors with L_A inductance. The converter is connected to the AC system via a line filter inductance of L_G.

During normal operation of the MMC, N capacitors are inserted between the DC link with U_{DC} voltage. Therefore, the nominal capacitor voltage, $v_{C,nom}$, is

$$v_{C,nom} = \frac{U_{DC}}{N} \tag{2.1}$$

However, this ideal voltage is not present in practice at all time (due to capacitor discharging, modulation method, etc.). An arm inductor can absorb the voltage difference in the loop and satisfy KVL. Due to this voltage mismatch, circulating currents are generated in MMCs. They do not enter the AC current (i_Σ). However, circulating currents flow into the other phase arms as well as the DC link. Proper sizing of arm inductors is required to limit circulating current and

reduce losses [19]. During a fault on the DC grid, the arm inductor can limit the rate of change of fault current thus giving more time for protection gear to operate.

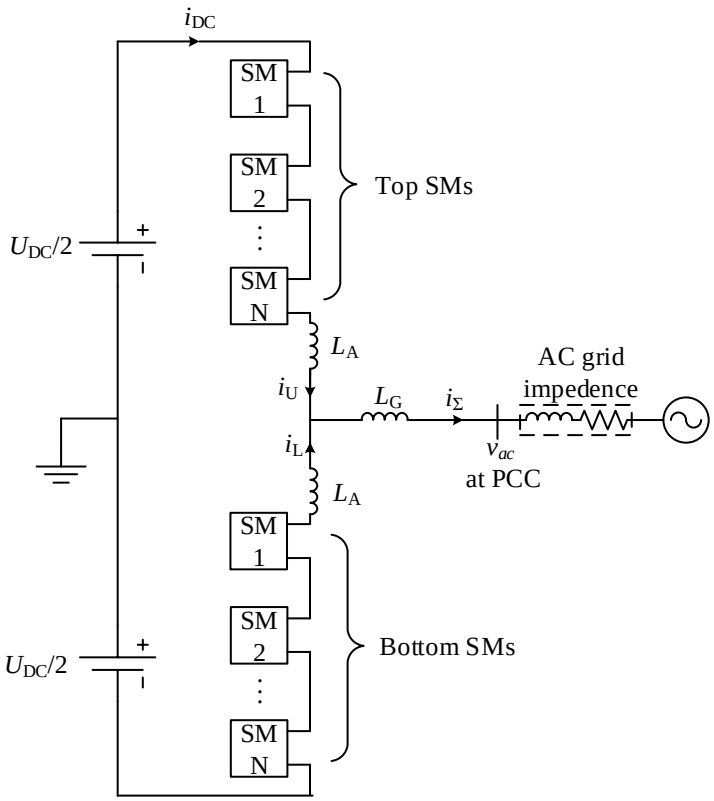


Figure 2.1: Structure of a single-phase MMC with energy storage.

To understand the operation of the MMC, power flow within the converter must be properly understood. A simplified model of the MMC with energy storage is used for this purpose (see Figure 2.2). All the SMs of an arm are assumed to be a single low-frequency voltage source, which produces non-negative voltages for simplicity. It is assumed that there is a large number of SMs to develop nearly sinusoidal waveforms. It is also assumed that power from batteries is equally distributed among SM units.

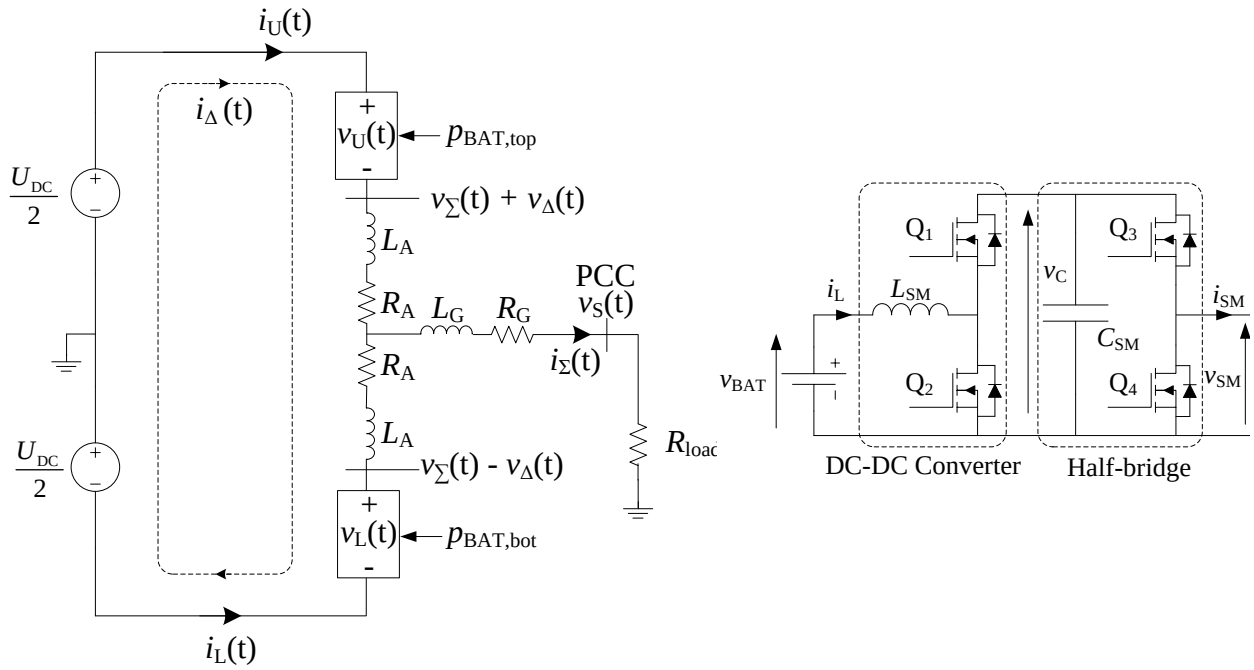


Figure 2.2: (a) Model of the MMC with energy storage (b) SM with storage.

The voltages $v_U(t)$ and $v_L(t)$ are developed by the upper and lower phase-arm multivalves, respectively. They can be expressed in terms of AC voltage, $v_\Sigma(t)$, ripple voltage, $v_\Delta(t)$, and DC link voltage, U_{DC}, as follows:

$$v_U(t) = \frac{U_{DC}}{2} - v_\Sigma(t) - v_\Delta(t) \tag{2.2}$$

$$v_L(t) = \frac{U_{DC}}{2} + v_\Sigma(t) - v_\Delta(t) \tag{2.3}$$

The AC current, $i_\Sigma(t)$, is driven by $v_\Sigma(t)$ and the circulating current, $i_\Delta(t)$, is driven by $v_\Delta(t)$. These voltages can be expressed as voltage drops across impedances and AC grid voltage, $v_S(t)$, as follows.

$$v_\Sigma(t) = v_S(t) + \left(R_G + \frac{R_A}{2}\right) i_\Sigma(t) + \left(L_G + \frac{L_A}{2}\right) \frac{d}{dt} i_\Sigma(t) \tag{2.4}$$

$$v_{\Delta}(t) = R_{A} i_{\Delta}(t) + L_{A} \frac{d}{dt} i_{\Delta}(t) \tag{2.5}$$

The phase arm currents $i_{U}(t)$ and $i_{L}(t)$ are composed of $i_{\Sigma}(t)$ and $i_{\Delta}(t)$, as shown below.

$$i_{U}(t) = \frac{i_{\Sigma}(t)}{2} + i_{\Delta}(t) \tag{2.6}$$

$$i_{L}(t) = \frac{i_{\Sigma}(t)}{2} - i_{\Delta}(t) \tag{2.7}$$

With (2.4) to (2.7), the power provided by the top and bottom SMs ($P_{OUT,U}$ and $P_{OUT,L}$) can be calculated:

$$\begin{aligned} P_{OUT,U} &= \langle v_{U}(t) \times -i_{U}(t) \rangle \\ &= \frac{-\langle U_{DC} i_{\Sigma}(t) \rangle}{4} - \frac{\langle U_{DC} i_{\Delta}(t) \rangle}{2} + \frac{\langle v_{\Sigma}(t) i_{\Sigma}(t) \rangle}{2} + \langle v_{\Sigma}(t) i_{\Delta}(t) \rangle + \frac{\langle v_{\Delta}(t) i_{\Sigma}(t) \rangle}{2} + \langle v_{\Delta}(t) i_{\Delta}(t) \rangle \end{aligned} \tag{2.8}$$

$$\begin{aligned} P_{OUT,L} &= \langle v_{L}(t) \times i_{L}(t) \rangle \\ &= \frac{\langle U_{DC} i_{\Sigma}(t) \rangle}{4} - \frac{\langle U_{DC} i_{\Delta}(t) \rangle}{2} + \frac{\langle v_{\Sigma}(t) i_{\Sigma}(t) \rangle}{2} - \langle v_{\Sigma}(t) i_{\Delta}(t) \rangle - \frac{\langle v_{\Delta}(t) i_{\Sigma}(t) \rangle}{2} + \langle v_{\Delta}(t) i_{\Delta}(t) \rangle \end{aligned} \tag{2.9}$$

The total power supplied by the SM battery units ($P_{OUT,TOTAL}$) is as follows.

$$P_{OUT,TOTAL} = -\langle U_{DC} i_{\Delta}(t) \rangle + \langle v_{\Sigma}(t) i_{\Sigma}(t) \rangle + 2 \langle v_{\Delta}(t) i_{\Delta}(t) \rangle \tag{2.10}$$

The first term in (2.10) represents the power drawn from the DC source to the MMC. The DC component of $i_{\Delta}(t)$ may be forced to zero by a controller to limit the power drawn from the DC source if desired. The second term represents the AC power sent across the point of common coupling (PCC). The last term is the average power across the arm inductors from circulating currents and is negligible. Thus, the power supplied by the batteries can be supplied to the AC grid. The work done in [13] mainly concentrates on the internal power flow of an MMC with energy storage. The work proves that inter-arm and inter-phase power transfer is possible.

Therefore, the MMC can be operated when a portion of the energy storage units are out of order. The same control techniques can be adapted to the MMC described in this thesis for more flexible operation.

2.2 SM Structure

There are basically two types of SMs used in MMCs with energy storage. Their schematic diagrams are shown in Figure 2.3.

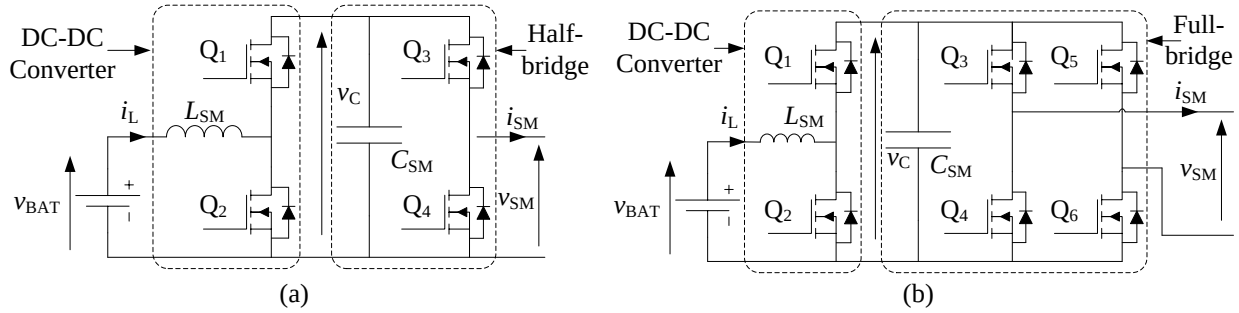


Figure 2.3: SM topologies (a) Half-bridge SM (b) Full bridge SM.

The half-bridge SM is the most commonly used SM topology [14]. Fewer switches make the SM less expensive and easy to control and produce low power losses. The SM output voltage (v_{SM}) can only be v_C or 0. During a fault at DC link, fault current from the AC grid flows to the DC side via the anti-parallel diode. However, in BESS applications, the likelihood of a DC fault is slim as the MMC will likely not be connected to a DC grid. The DC link may consist of a high impedance ground made with two capacitors. Thus, the half-bridge SM is more commonly used in MMCs with BESS.

The full-bridge is capable of producing 0, $+v_C$, and $-v_C$ at the SM output voltage (v_{SM}). Therefore, the same output voltage quality can be obtained with fewer SMs compared to a half-bridge SM. This SM can block DC fault current, as the SM capacitors are inserted in series with the fault current via the diodes. The additional power electronic components in the SM make it

more lossy, expensive, and complex to control. Authors of [20] have studied the use of full-bridge SMs along with half-bridge SMs in the same multivalve. This approach can be used to arrive at a compromise of handling DC fault current, power losses, and cost.

Since the half-bridge SM is the most cost-effective, low loss option for MMCs with BESS, this thesis concentrates on MMCs built only with half-bridge SMs [21]. The developed modeling method, however, may be readily extended to full-bridge SMs as well.

2.3 Operation of the Half-Bridge SM

As seen in the previous chapter, the SM contains a DC-DC converter and a half-bridge/full-bridge converter. The DC-DC converter is operated to maintain the capacitor voltage. The half-bridge/full-bridge converter is operated to produce the output voltage. This section will cover the operation of a half-bridge converter to produce the AC output voltage waveform.

2.3.1 PWM Methods

There are several switching techniques available to operate an MMC. Pulse-width modulation is among the most popular. To control N SMs in a multivalve, these methods generate N carrier waveforms, one carrier per SM. A reference signal, generated by an upstream control system, is then compared with the carriers. At a given instant of time, depending on the value of the reference signal compared to the carrier, SMs are inserted or bypassed. Phase disposition (PD), phase opposition disposition (POD), alternate phase opposition disposition (APOD), and phase shifted carrier waveforms are some of the most common multilevel carrier signals. For better output performance, all these carriers have relatively high frequencies compared with that of the reference, which results in higher losses [22]. Figure 2.4 shows the arrangement of multilevel carriers.

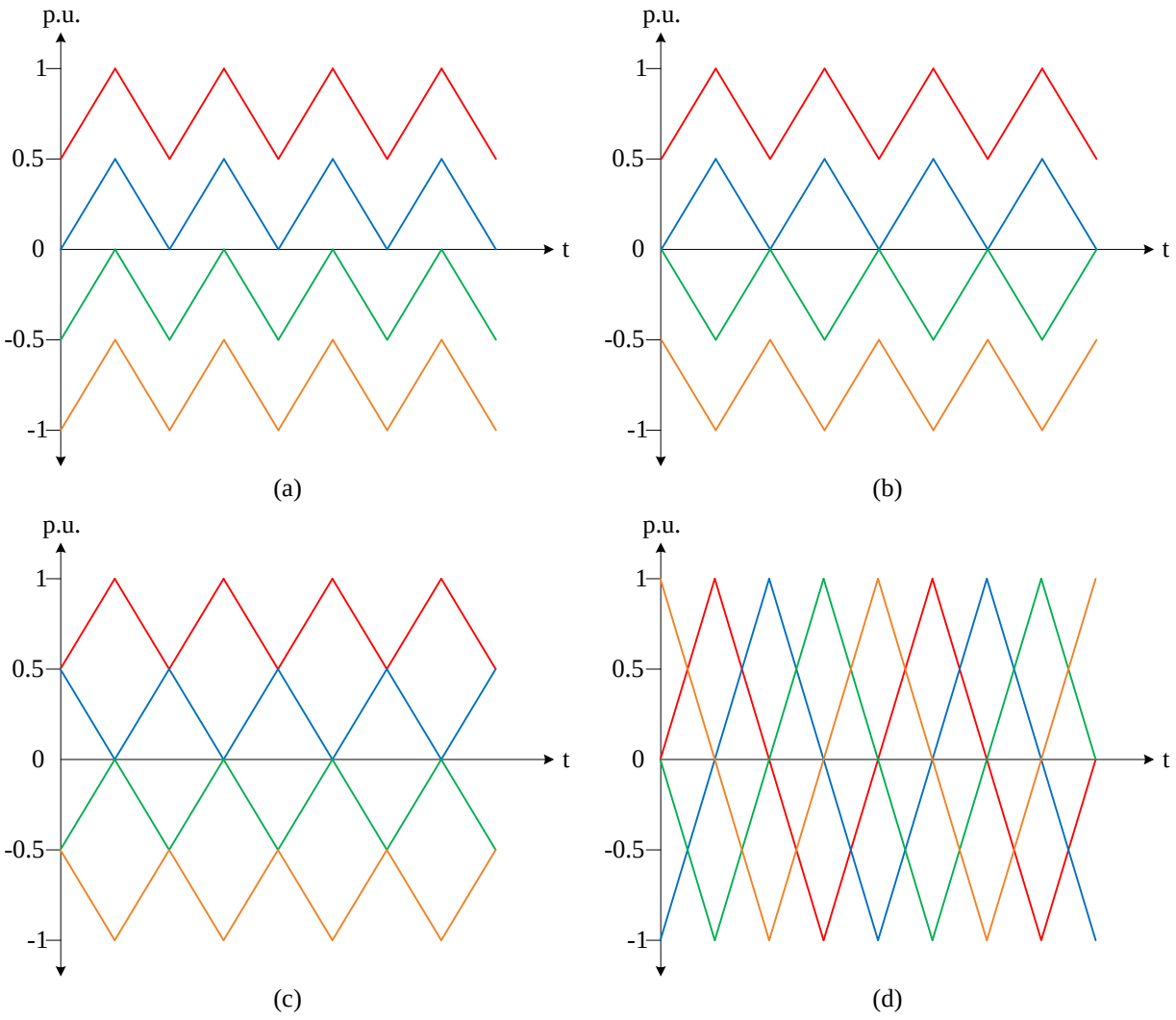


Figure 2.4: Multilevel carriers (a) PD (b) POD (c) APOD (d) phase shifted carriers.

2.3.2 Nearest Level Control (NLC)

Apart from the PWM methods, there are low-frequency switching techniques such as NLC. This control algorithm determines how many SMs need to be inserted by considering the present value of the reference signal (v_{ref}) and its relative value to the closest lower and upper voltages surrounding it that may be generated with the available SMs. As a result, a staircase waveform will be developed at the output (v_{out}) (Figure 2.5). Since the switching is done at system frequency (50 or 60 Hz), the switching losses are exceptionally low in this method. However, for

better output voltage quality and to develop a large number of steps, a large number of SMs is required. The algorithm for calculating the number of SMs (n) to be inserted at a given time and the output voltage (v_{OUT}) is as shown in (2.11) and (2.12).

For N SMs with a reference voltage v_{ref} and nominal capacitor voltage v_{CAP},

For even N, where $0 \le n \le \frac{N}{2}$

$$v_{OUT} = \begin{cases} nv_{CAP}; v_{ref} < \left(n + \frac{1}{2}\right)v_{CAP} \\ (n+1)v_{CAP}; v_{ref} > \left(n + \frac{1}{2}\right)v_{CAP} \end{cases} \tag{2.11}$$

For odd N where $0 \le n \le \frac{N-1}{2}$

$$v_{OUT} = \begin{cases} \left(n - \frac{1}{2}\right)v_{CAP}; v_{ref} < nv_{CAP} \\ \left(n + \frac{1}{2}\right)v_{CAP}; v_{ref} > nv_{CAP} \end{cases} \tag{2.12}$$

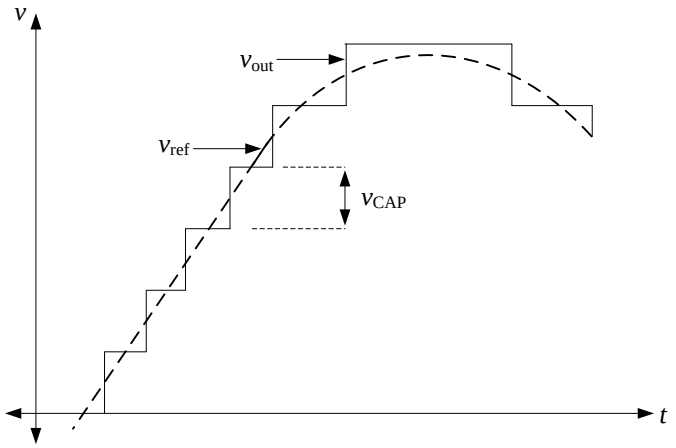


Figure 2.5: Nearest Level Control (NLC)

In this thesis, NLC is used due to its simplicity and low losses.

2.4 Operation of the DC-DC Converter

A battery is connected to each half-bridge/full-bridge via a DC-DC converter. The converter considered in this thesis is a bi-directional DC-DC converter. The converter operates in boost mode when sending power from the battery to the SM capacitor. The converter is operated in buck mode when the batteries are charged from the power coming from the capacitor side (see Figure 2.6).

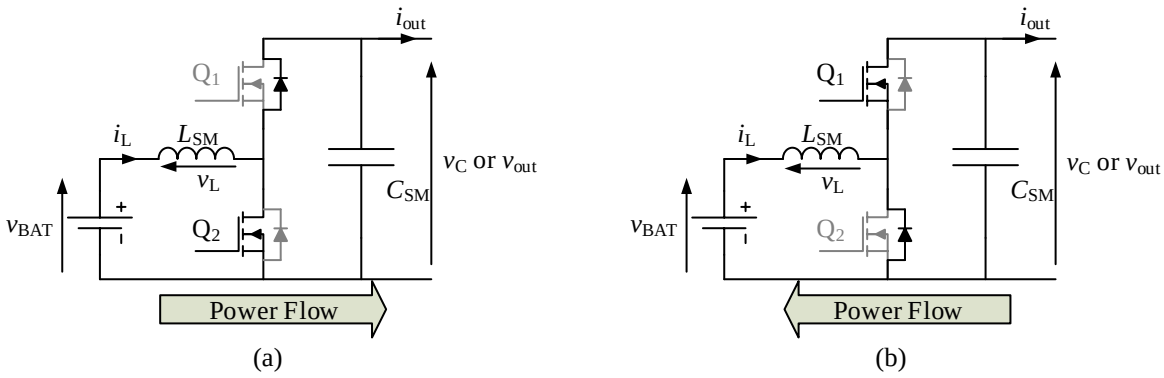


Figure 2.6: DC-DC converter operation (a) boost mode (b) buck mode.

To operate the converter, firing pulses are sent to the MOSFETs Q_1 or Q_2. The firing pulses are generated by comparing the DC duty value (D) (which is defined between 0 to 1.0) with a triangular waveform of $f_{DC\text{-}DC}$ frequency varying between 0 and 1. The firing pulse (FP) given to the converter is as in (2.13); T is the period of the switching signal.

$$\text{FP} = \begin{cases} 1 & 0 < t \le DT \\ 0 & DT < t \le T \end{cases} \tag{2.13}$$

In boost mode, firing pulses are sent only to Q_2 while in buck mode firing pulses are sent to Q_1. The MOSFET that is not issued a firing pulse has its gate short circuited with its source (0 firing pulse issued). In both situations, the inductor current is carried by a MOSFET and the

complementary diode. Figure 2.7 shows the inductor current and inductor voltage waveforms in boost and buck modes with parameters defined in Figure 2.6.

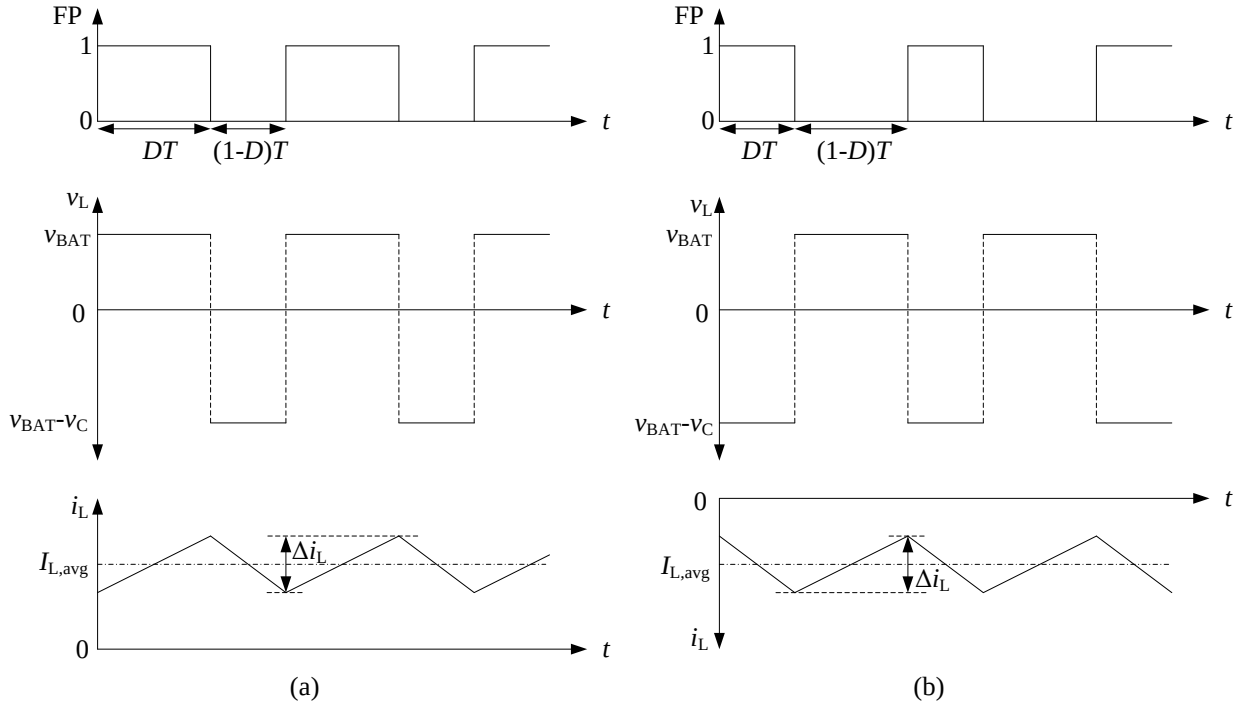


Figure 2.7: DC-DC converter waveforms (a) boost action (b) buck action.

Selecting an inductor with suitable inductance is vital for the proper operation of the converter. The inductance must be selected such that the inductor ripple can be tolerated by the battery. Equations (2.14)-(2.16) show how to calculate the inductance for a known current ripple. For an inductor

$$v_{\mathrm{L}} = L\frac{di_{\mathrm{L}}}{dt} \tag{2.14}$$

For a small-time period Δt with constant inductor voltage v_{L}:

$$v_{\mathrm{L}} = L\frac{\Delta i_{\mathrm{L}}}{\Delta t} \tag{2.15}$$

Considering the time period $0 < t \le DT$

$$v_{\mathrm{BAT}} = L_{\mathrm{SM}} \frac{\Delta i_{\mathrm{L}}}{DT}$$

$$L_{\mathrm{SM}} = \frac{v_{\mathrm{BAT}} DT}{\Delta i_L} \tag{2.16}$$

Generally and for practicality, inductor current ripple is allowed to be 10-20% of the rated average inductor current.

2.5 Capacitor Voltage Balancing

During the operation of the MMC, capacitors in all SMs must have an almost equal voltage. At a given arm, in a multivalve, only a fraction of the SMs are inserted depending on the modulation signal. If only the same SMs are inserted during these instants, the voltage of the SMs used will drastically change. This is a matter that has to be properly dealt with.

The sorting algorithm described in [23] is the most popular method used to balance the SM capacitor voltages. The algorithm requires the multivalve current and individual capacitor voltages as inputs. The modulation method or NLC calculates how many SMs need to be inserted in a multivalve at a given time. The algorithm then inserts the SMs with the lowest capacitor voltages when the multivalve current is positive (positive current: current into the multivalve at positive voltage end). The multivalve current will charge the capacitors. Conversely, when the current is negative the SMs with the highest voltage will be inserted and the capacitor voltage will be reduced. To avoid unnecessary switching of SMs, the algorithm is only activated when there is a change in the number of SMs being inserted or if there is not a level change for a long time. Other than the sorting algorithm, there are other methods based on PWM schemes, closed-loop control, and predictive control to balance the capacitor voltages as shown in [24]-[26].

2.6 Converter Control Methods

The MMC with BESS typically connects to the AC grid at a controlled active power and AC voltage mode (PV bus at the connecting node). It may be configured as an active and reactive power source as well (PQ bus at the connecting node). However, as an application to improve AC voltage in medium voltage (MV) networks and supplying a defined amount of power for load leveling, the PV bus application presents the most practical use.

There are basically two methods to control the MMC with BESS as a PV bus as follows.

1. Direct control method.
2. Decoupled control method.

2.6.1 Direct Control of an MMC with BESS

The single-phase AC voltage amplitude can be expressed using the modulation index *m* as follows;

$$\hat{v}_{\mathrm{AC}} = m\frac{U_{\mathrm{DC}}}{2} \tag{2.17}$$

Since the DC link voltage, U_{DC}, is kept constant, the AC voltage magnitude is proportional to the modulation index. AC voltage can be controlled by changing the modulation index.

In the MMC, the user has direct control of the voltage behind the arm inductor. This is close in magnitude to the voltage at the point of common coupling (PCC) if the voltage drop along the path is ignored.

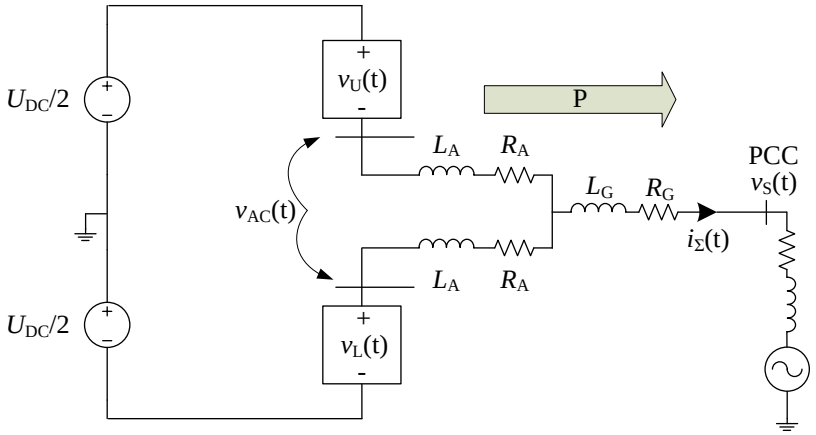


Figure 2.8: Power flow of an MMC with BESS.

Using the notion of power flow through an impedance, an expression can be derived for the active power flow from the MMC to the AC grid using Figure 2.8 as given in (2.18). In this equation, δ is called the "power angle", which is the phase difference between v_{AC} and v_S, and f_{AC} is the AC grid frequency.

$$P_{AC} = \frac{|v_{AC}||v_S|\sin\delta}{2\pi f_{AC}\left(L_G + \frac{L_A}{2}\right)} \tag{2.18}$$

As seen from (2.18) the active power can be controlled by changing $|v_{AC}|$ and/or δ. In normal operation, the AC voltage needs to be kept nearly constant. Thus, power can be controlled by changing δ. Proportional-integral (PI) controllers shown in Figure 2.9 can be used to control the AC voltage at the desired value. However, a change in one parameter affects the other parameter since they are not decoupled.

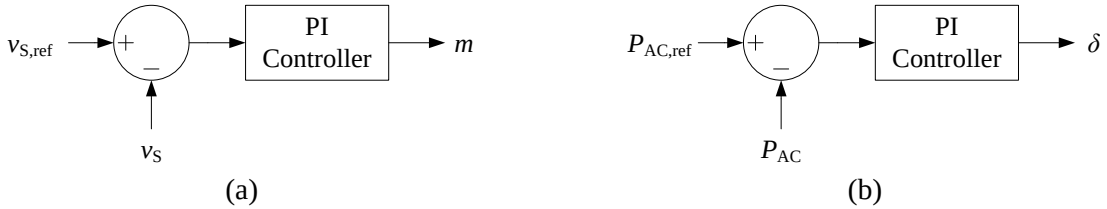


Figure 2.9: Direct controllers (a) AC voltage controller (b) AC active power controller.

2.6.2 Decoupled Control of an MMC with BESS

In this method, voltages and currents of the MMC are transformed into a rotating synchronous frame [27]. The transformation used is known as "Park's transformation" (2.19). In this frame, the three-phase domain (abc) quantities are represented in dqo domain. θ is selected to be ωt where ω is the system frequency. In practice θ is locked to the voltage at PCC using a phase locked-loop (PLL).

$$\begin{pmatrix} x_{\mathrm{d}} \\ x_{\mathrm{q}} \\ x_{0} \end{pmatrix} = \frac{2}{3} \begin{pmatrix} \cos\theta & \cos\left(\theta - \frac{2\pi}{3}\right) & \cos\left(\theta + \frac{2\pi}{3}\right) \\ \sin\theta & \sin\left(\theta - \frac{2\pi}{3}\right) & \sin\left(\theta + \frac{2\pi}{3}\right) \\ 0.5 & 0.5 & 0.5 \end{pmatrix} \begin{pmatrix} x_{\mathrm{a}} \\ x_{\mathrm{b}} \\ x_{\mathrm{c}} \end{pmatrix} \tag{2.19}$$

The active power (P_{m}) and reactive power (Q_{m}) supplied by the converter can be calculated from the three-phase quantities at the PCC.

$$P_{\mathrm{m}} = v_{\mathrm{S,a}} i_{\mathrm{a}} + v_{\mathrm{S,b}} i_{\mathrm{b}} + v_{\mathrm{S,c}} i_{\mathrm{c}} \tag{2.20}$$

$$Q_{\mathrm{m}} = v_{\mathrm{S,bc}} i_{\mathrm{a}} + v_{\mathrm{S,ca}} i_{\mathrm{b}} + v_{\mathrm{S,ab}} i_{\mathrm{c}} \tag{2.21}$$

Neglecting resistance, from Figure 2.8 it can be derived that

$$\left(v_{\mathrm{AC}}\right)_{\mathrm{abc}} = \left(v_{\mathrm{S}}\right)_{\mathrm{abc}} + \left(\frac{L_{\mathrm{A}}}{2} + L_{\mathrm{G}}\right) \frac{d\left(i_{\Sigma}\right)_{\mathrm{abc}}}{dt} \tag{2.22}$$

Park's transformation can be used to modify (2.20)-(2.22) as follows. In these equations "T" is the Park's transform.

$$\left(i_{\Sigma}\right)_{\mathrm{dq0}} = T\left(i_{\Sigma}\right)_{\mathrm{abc}} \tag{2.23}$$

$$\left(v_{\mathrm{S}}\right)_{\mathrm{dq0}} = T\left(v_{\mathrm{S}}\right)_{\mathrm{abc}} \tag{2.24}$$

$$P_{\mathrm{m}} = \frac{3}{2} v_{\mathrm{S,d}} i_{\mathrm{d}} + \frac{3}{2} v_{\mathrm{S,q}} i_{\mathrm{q}} + v_{\mathrm{S,0}} i_{0} \tag{2.25}$$

$$Q_{\mathrm{m}} = \frac{3}{2} v_{\mathrm{S,d}} i_{\mathrm{q}} - \frac{3}{2} v_{\mathrm{S,q}} i_{\mathrm{d}} \tag{2.26}$$

$$\left(v_{\mathrm{AC}}\right)_{\mathrm{dq0}} = \left(v_{\mathrm{S}}\right)_{\mathrm{dq0}} + \left(\frac{L_{\mathrm{A}}}{2} + L_{\mathrm{G}}\right) T \frac{d\left(T^{-1}\left(i_{\Sigma}\right)_{\mathrm{dq0}}\right)}{dt}$$

$$\left(v_{\mathrm{AC}}\right)_{\mathrm{dq0}} = \left(v_{\mathrm{S}}\right)_{\mathrm{dq0}} + \left(\frac{L_{\mathrm{A}}}{2} + L_{\mathrm{G}}\right) \frac{d\left(i_{\Sigma}\right)_{\mathrm{dq0}}}{dt} + \left(\frac{L_{\mathrm{A}}}{2} + L_{\mathrm{G}}\right) \omega \begin{pmatrix} 0 & 1 & 0 \\ -1 & 0 & 0 \\ 0 & 0 & 0 \end{pmatrix} \left(i_{\Sigma}\right)_{\mathrm{dq0}} \tag{2.27}$$

In a balanced system, the zero-sequence parameter (x_0) can be neglected. A decoupled controller can be designed as shown in Figure 2.10 using (2.23)-(2.27). In this method, to control each parameter, two PI controllers are required. Tuning the gains of these PI controllers can become complex. Thus, in this thesis direct control is used to control the MMC for the sake of simplicity. This choice has no practical bearing on the applicability and usefulness of the detailed equivalent model that is developed for the MMC.

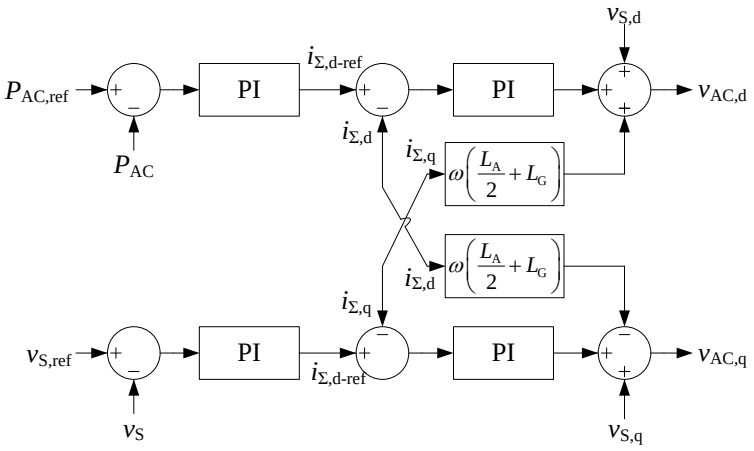


Figure 2.10: Decoupled AC active power and AC voltage controller.

2.7 Converter-Grid Synchronization

For proper operation of the MMC with BESS, the phase angle at the PCC must be known to define the power angle δ and to derive the dq0 quantities. A PLL is used to obtain the phase angle at the PCC. The PLL synchronizes to the grid frequency and an integrator derives the phase angle. The phase angle is matched to the phase angle of the voltage using a PI controller. A block diagram of a simple PLL is shown in Figure 2.11. This PLL is used throughout in this thesis.

Proper synchronization is vital to avoid any high inrush current that may flow from/to the converter at its startup. A good PLL scheme provides good synchronization means.

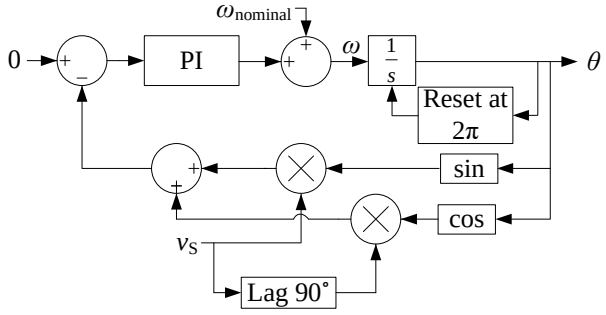


Figure 2.11: Phase locked loop (PLL)

2.8 Summary

In this chapter, an overall review of the operation of the MMC was provided. The power flow of the MMC with BESS was analyzed using a low-frequency averaged model. An overview of the commonly used SMs in MMC with BESS was done and the switching techniques used to operate the SMs were also reviewed. The importance of the DC-DC converter in each SM was discussed by analyzing its buck and boost operation. Active power and AC bus voltage control methods were reviewed elaborating their benefits and drawbacks. Finally, the importance of a PLL for MMC was studied with a suitable PLL structure.

Chapter 3: Control and Protection of the MMC with Embedded Energy Storage

3.1 Active Power and AC Voltage Controller

In this thesis, direct control of active power and AC voltage is done as described in Section 2.6.1. The AC voltage controller is slightly changed to introduce the modulation index at steady state (m_{ss}). This will make the control fast as the PI controller can arrive at the steady state to cancel the error very rapidly. However, this method cannot be used in the power controller, as the AC power command needs to be changed to various values during normal operation of the MMC with BESS.

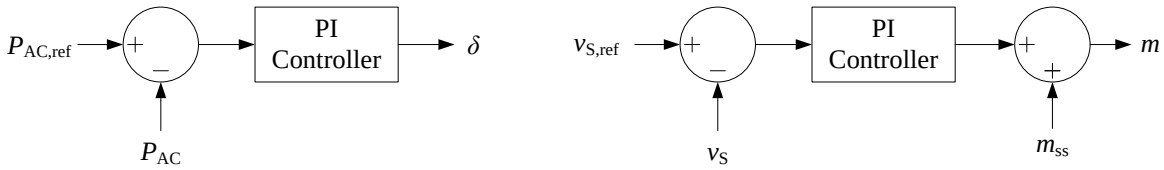


Figure 3.1: Direct controllers (a) AC active power controller (b) AC voltage controller.

When tuning the controllers large time constants and small proportional gains are selected for the PI controllers to avoid any sudden change in power or voltage.

3.2 Controllers of the DC-DC Converter

The DC-DC converter in each SM is used to control the voltage of each SM capacitor. This can be done using two control loops: one internal control loop to control the inductor current and one outer control loop to control the capacitor voltage. Having two control loops slows down the response of the DC-DC converter, but the control over the inductor current is much more advantageous than not having any control. Limiters can be imposed in the current controller that

will avoid high currents to be drawn from the battery. This will enhance the lifetime and performance of the battery.

As the converter switches are always operated in a saturated mode, the DC-DC converter is inherently non-linear. In order to use analog control techniques such as PI controllers, a linearized model of the converter is needed. Appendix A shows linearization around an operating point for the boost converter. Following the same fundamentals, the linearized model for the buck converter can be derived.

From Appendix A, Laplace domain equations for the boost converter can be derived as in (3.1) and (3.2). Figure 3.2 is used to introduce the Laplace parameters used in the converter. $D(s)$, $I_{out}(s)$, $I_L(s)$, $V_C(s)$, and $V_{BAT}(s)$ are the Laplace transforms of the duty ratio, output current, inductor current, capacitor voltage, and battery voltage, respectively. D_o, $I_{L,o}$, $V_{C,o}$ are the operating point values of duty ratio, inductor current, and capacitor voltage.

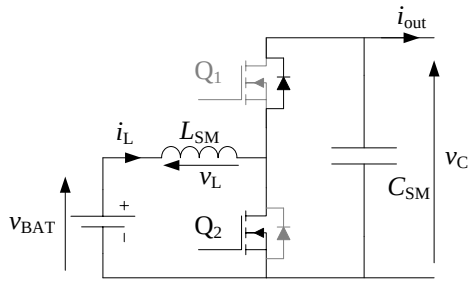


Figure 3.2: DC-DC converter of the SM.

$$L_{SM}sI_L(s) = V_{BAT}(s) - (1-D_o)V_C(s) + V_{C,o}D(s) \tag{3.1}$$

$$C_{SM}sV_C(s) = (1-D_o)I_L(s) - I_{L,o}D(s) - I_{out}(s) \tag{3.2}$$

3.2.1 Current Controller

The current controller can be designed as shown in Figure 3.3 using (3.1).

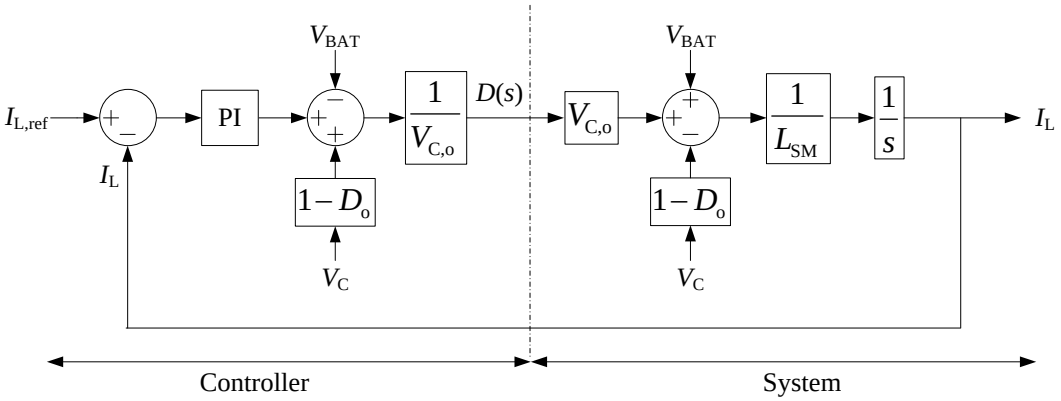


Figure 3.3: Current controller.

The above implementation cancels out all feedforward terms and makes the controller fast. Tuning of the current controller PI gains should be carried out such that the poles of the current controller lie on the negative real axis and slower than the switching frequency. This ensures the stability of the controller. Hence, in this thesis, the two poles are placed at $1/10^{th}$ and $1/40^{th}$ of the DC-DC converter switching frequency [28], [29].

3.2.2 Voltage Controller

The voltage controller can be designed as shown in Figure 3.4 using (3.2).

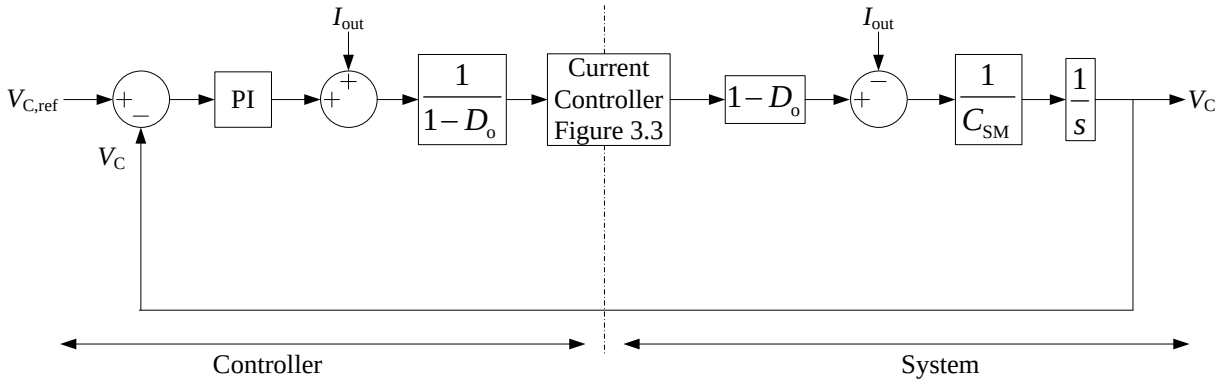


Figure 3.4: Voltage controller.

The voltage controller is also tuned such that the poles of the controller lie on the negative real axis of the complex plane. The poles of the voltage controller need to be comparatively slower than the system frequency to filter out the low-frequency voltage ripple in the capacitor voltage.

3.2.3 Controller Structure Used in the Thesis

The current controller and voltage controller discussed in Sections 3.2.1 and 3.2.2 are slightly changed in this thesis. All the existing feedforward terms are not used in the controller implementation. This reduces the need for additional measurements. An additional current reference is added to the control loop based on the power command per SM. The power command is generated by the state of charge (SOC) balancing controllers, which are introduced in a later section. An additional limiter block is used for the inductor current reference to prevent it from being excessively large.

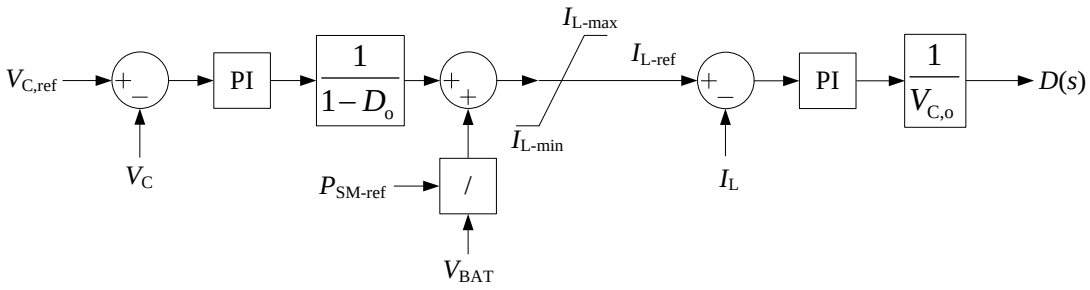


Figure 3.5: Implemented controller for the DC-DC converter.

3.3 SOC Controller

The MMC has batteries in each of the SM. When discharging the batteries, care must be taken to discharge all the batteries equally, so that the aging of batteries is uniform. The state of charge (SOC) describes the amount of charge left in a battery. Section 4.2 gives a detailed explanation of SOC, its measuring methods, and its relationship to voltage. The charge of a battery is quantified in Ampere-hours (Ah). The charge used from the battery can be measured by

integrating the current drawn from the battery over time. For a battery with a full charge of Q_{full} and current $i(t)$ drawn from it, the SOC is

$$SOC = \frac{Q_{\text{full}} - \int i(t)dt}{Q_{\text{full}}} \times 100\% \tag{3.3}$$

For a single-phase MMC with N SMs per arm, the following terms regarding the SOC must be defined for simplicity:

- $SOC_{\text{ph_avg}}$: Average SOC of a phase of the MMC.
- SOC_j (j = p for top, j = n for bottom): Average SOC of a phase arm of the MMC.
- SOC_{jk} (k = 1 to N): Individual SOC of each battery.
- P_{load}: AC power reference.
- P_j: Power reference for the phase arm.
- P_{jk}: Power reference for individual SM.
- N: Number of SMs in a phase arm.

The terms are related as follows.

$$SOC_j = \frac{\sum_{k=1}^{N} SOC_{jk}}{N} \tag{3.4}$$

$$SOC_{\text{ph_avg}} = \frac{SOC_{\text{p}} + SOC_{\text{n}}}{2} \tag{3.5}$$

3.3.1 Inter-Arm SOC Balancing Controller

The SOC of each phase arm is driven to match the $SOC_{\text{ph_avg}}$ using a proportional controller [30]. Figure 3.6 shows the proposed control diagram.

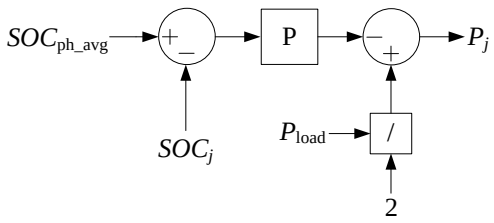


Figure 3.6: Inter-arm SOC balancing controller.

3.3.2 Intra-Arm SOC Balancing Controller

Similar to the inter-arm SOC balancing controller, the SOC of each battery is driven to match the average SOC of the phase arm by adjusting the power reference using a proportional controller. Figure 3.7 shows the proposed controller.

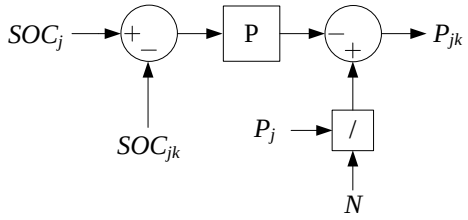


Figure 3.7: Intra-arm SOC balancing controller.

3.4 DC Power Suppression Controller

In this thesis, the MMC with storage is operated only as a battery power integration into the AC grid. Therefore, it is important to control any net power drawn from the DC side (external to the MMC) to zero. The DC power suppression controller observes the average DC current and regulates it to zero by adjusting the SM capacitor voltage around its nominal value.

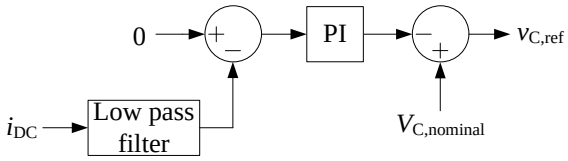


Figure 3.8: DC power suppression controller.

This controller ensures that no net power is drawn from the DC link, and the power sent to the AC grid is supplied solely by the energy storage units in each SM.

3.5 Breaker Protection Schemes

3.5.1 AC Breaker with Pre-Insertion Resistor

In the startup procedure mentioned in the following section, the AC grid is used to initially charge the SM capacitors to the nominal voltage. The connection of the MMC with the AC grid is done via a breaker with a pre-insertion resistor. A schematic diagram of the breaker is shown in Figure 3.9. When the breaker is closed, the resistor is inserted to the current path by closing S1. After some time when the current transients have died out, the resistor is bypassed by closing S2. The value of the pre-insertion resistor is best chosen via computer simulations as the value changes with each converter. In the developed experimental prototype, this arrangement is followed by a series thermal-magnetic breaker to trip and protect the MMC in case of any faults.

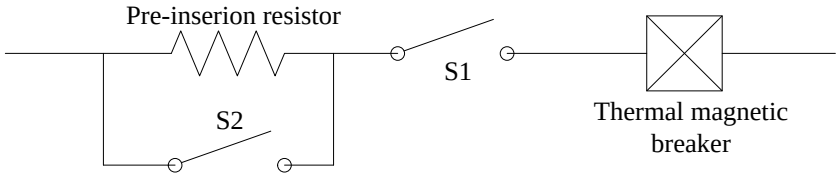


Figure 3.9: AC breaker.

3.5.2 DC Link Contactor with Pre-Insertion Resistor

Similar to the AC breaker in Section 3.5.1, a DC contactor is used to connect the MMC with DC link voltage sources. The pre-insertion resistor will limit the inrush current drawn to charge the capacitors. After the initial current, the pre-insertion resistor is bypassed.

3.5.3 DC Contactor on SMs

Due to the existence of the anti-parallel diodes in the DC-DC converter switches, even though the firing pulses are blocked for the DC-DC converter, a current may be drawn from the battery at a fault scenario or when the capacitor voltage is lower than the battery voltage. Thus, it

is recommended to have a disconnector to isolate the batteries from the MMC when desired. The DC contactor at the input of the DC-DC converter fulfills this aim. Figure 3.10 shows the connection of the contactor.

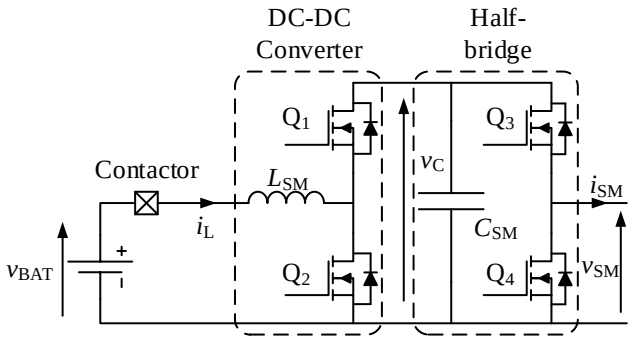


Figure 3.10: Contactor on the DC-DC converter.

3.6 Startup Procedure

The MMC with energy storage has a large capacitance within the converter. Therefore, when the MMC is fully discharged, care must be taken to avoid large inrush currents that may occur due to the charging of capacitors during startup. A proper startup procedure could gradually charge the capacitor before connecting the MMC to the AC grid. During this procedure, the controllers associated with the operation of MMC need to be engaged in a coordinated manner. Figure 3.11 shows such a startup procedure developed for the MMC with energy storage. This is a further development of the work done in [31].

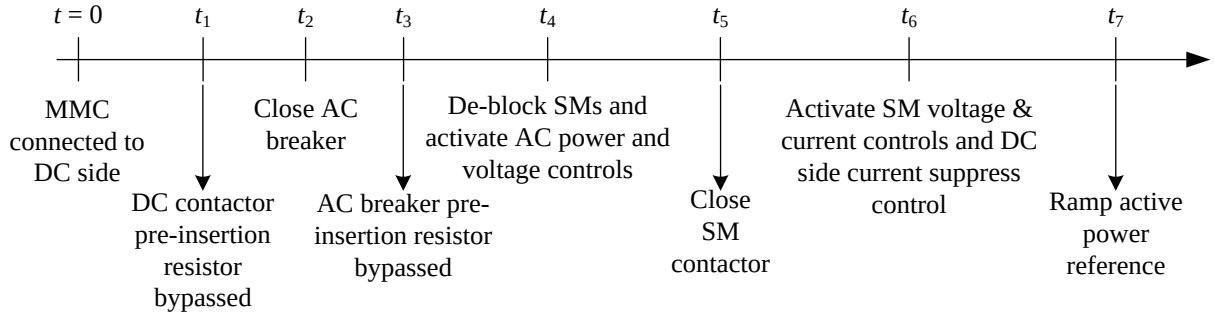


Figure 3.11: Startup procedure.

The DC source is connected to the MMC at t_0 through the DC relay. At t_1 the pre-insertion resistor of DC breaker will be bypassed. Then the converter is connected to the AC grid via the AC breaker at t_2. The pre-insertion resistor of the AC breaker is bypassed after SM capacitor voltage has reached a steady state at t_3. After voltage transients in SM capacitors have died out, the MMC is deblocked at t_4. The active power and voltage controllers are activated, and the modulation index is initialized to m_{SS}. This procedure concludes the charging of SM capacitors to the nominal voltage. Next, at t_5 batteries are connected to the SM by closing the contactors in each SM. Firing pulses for the DC-DC converter are still not issued and no current will be drawn from the batteries as the capacitor voltage is higher than the battery voltage. Soon after the contactor is closed SM capacitor voltage controllers and inductor current controllers are activated at t_6. At this point, the MMC is ready to provide power. The active power reference can be gradually ramped up to its desired value.

3.7 Simulation Validation of Control and Operation

An example single-phase MMC with BESS was simulated in PSCAD/EMTDC to validate the operation of the MMC and its proposed controls (PSCAD/EMTDC is a power system ElectroMagnetic Transients simulator. The software uses a graphical user interface to construct circuits. The software also provides the capability to develop user defined components using FORTRAN language). The parameters of the converter are presented in Table 3.1. Appendix B gives guidelines to select the parameters to match the converter ratings.

The MMC is simulated from an initially discharged condition to the rated power operation. Figures 3.12-3.18 show the PSCAD/EMTDC simulation results. Simulations are carried out at a 5 μs time step for 6 s. Table 3.2 shows the time instants described in Section 3.6.

Table 3.1: Parameters of the simulated MMC

Symbol	Value	Description
v_S	230 V	AC grid voltage
U_{DC}	800 V	DC link voltage
S_{RATED}	20 kVA	Rated apparent power
$P_{AC\text{-}RATED}$	15 kW	Rated active power
N	10	Number of SMs per arm
f_{SYS}	60 Hz	AC system frequency
f_{DCDC}	15 kHz	DC-DC converter switching frequency
L_G	4.24 mH	Grid interface inductance
R_G	0.01 Ω	Grid interface resistance
L_A	2.12 mH	Arm inductance
R_A	0.01 Ω	Arm resistance
C_{SM}	12 mF	SM capacitance
L_{SM}	1 mH	SM DC-DC converter inductance
V_{BAT}	60 V	Battery nominal voltage
$R_{AC,PRE\text{-}INS}$	10 Ω	AC breaker pre-insertion resistor
$R_{DC,PRE\text{-}INS}$	50 Ω	DC contactor pre-insertion resistor

Table 3.2: Startup procedure time instants.

Instant	Time [s]	Instant	Time [s]
t_0	0.50	t_4	2.50
t_1	0.08	t_5	3.50
t_2	1.50	t_6	3.51
t_3	2.00	t_7	3.55

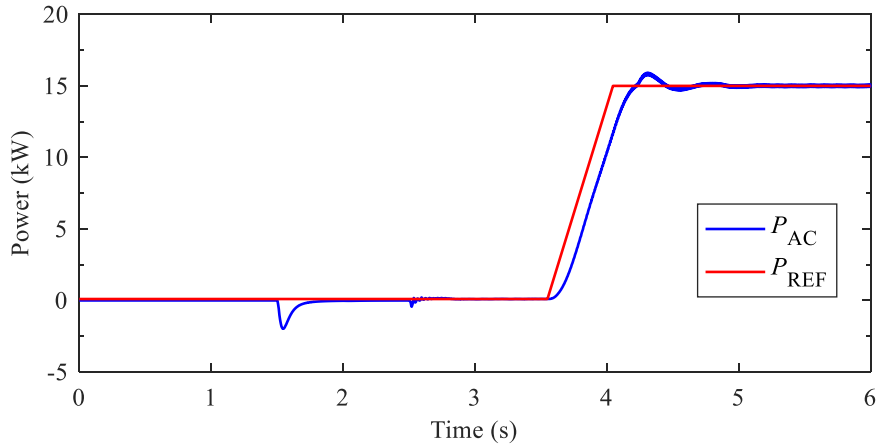


Figure 3.12: AC power variation during startup.

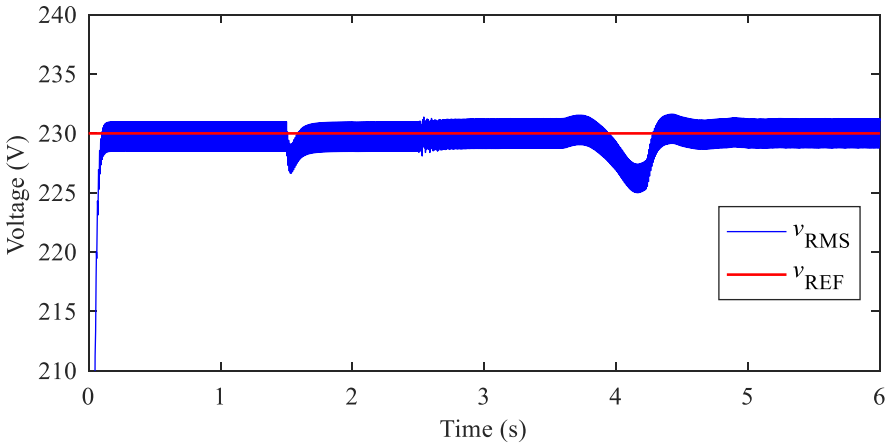


Figure 3.13: AC bus rms voltage during startup.

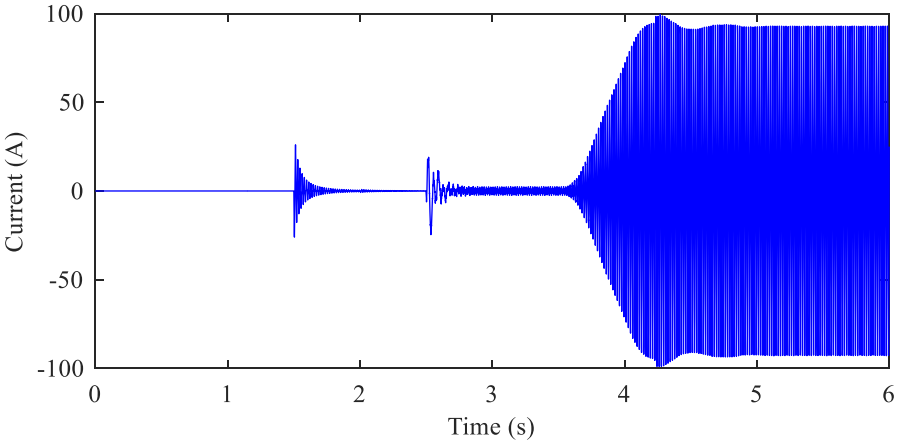


Figure 3.14: AC line current during startup.

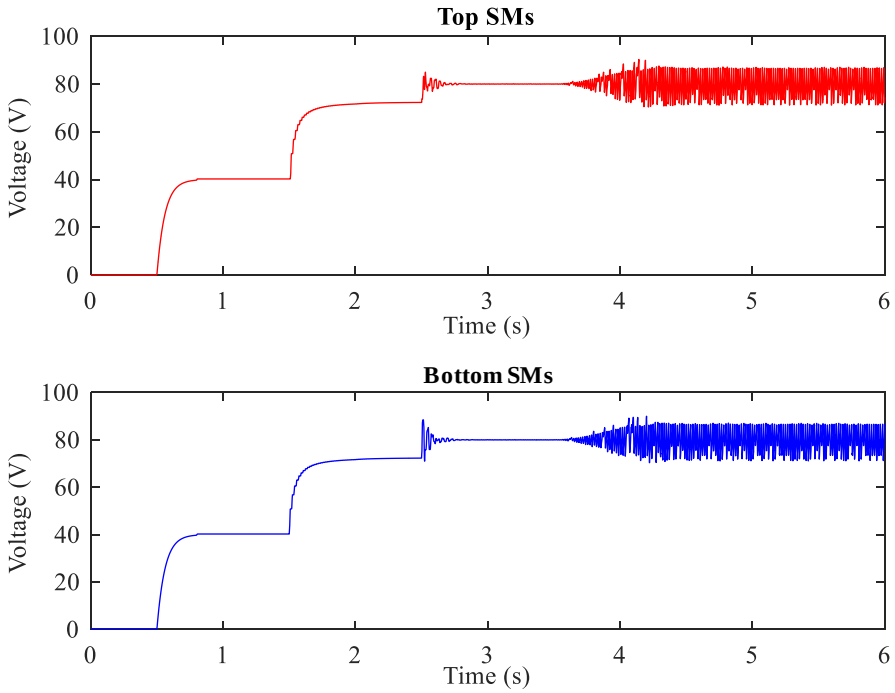


Figure 3.15: Capacitor voltages during startup.

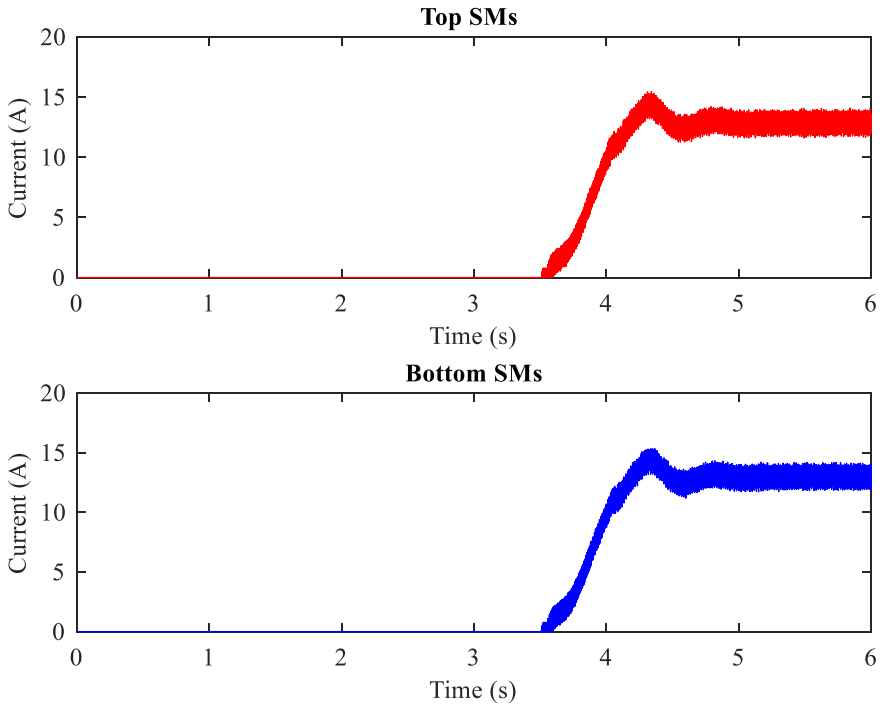


Figure 3.16: Battery currents during startup.

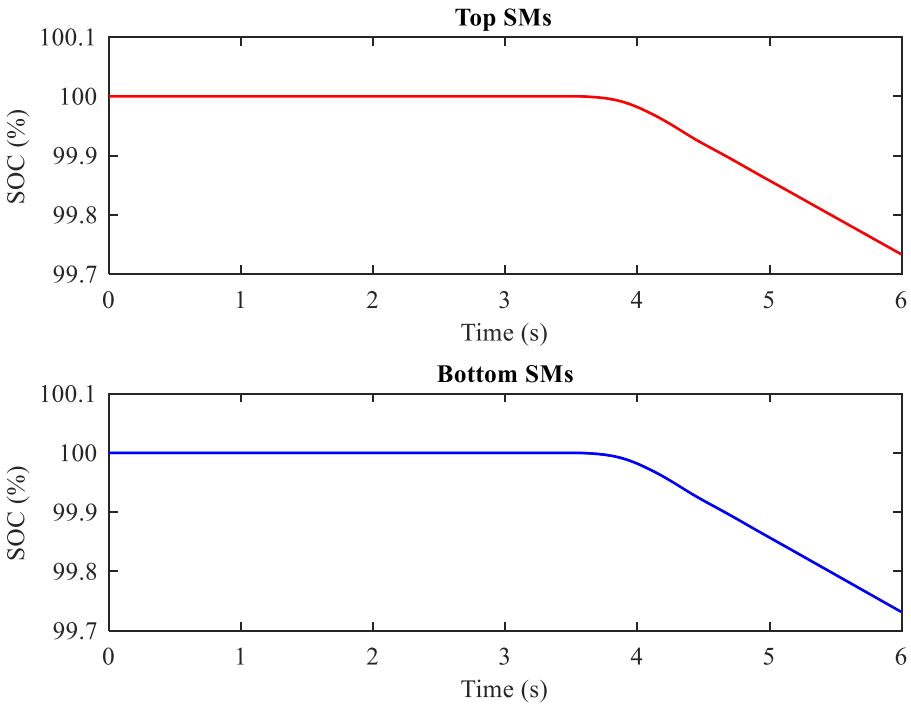


Figure 3.17: Variation of SOC of top and bottom SMs.

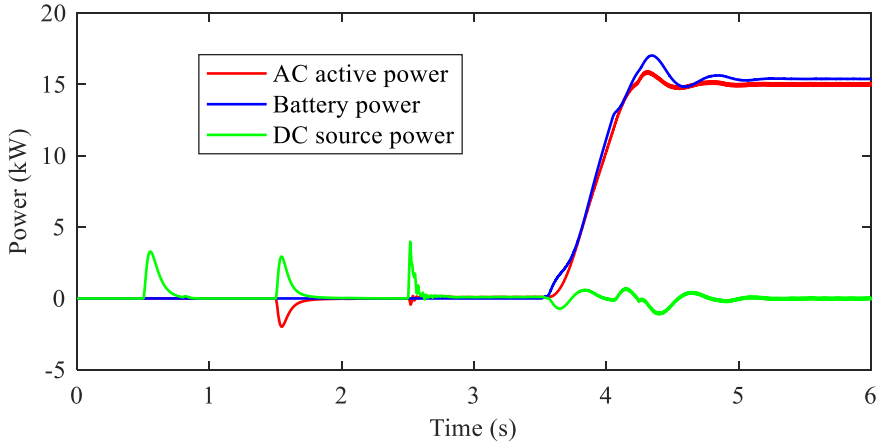


Figure 3.18: Power distribution of the converter.

The AC power reference is kept at 0 kW until 3.55 s and then gradually ramped up to 15 kW. AC voltage reference is kept at 230 V throughout the simulation. Figure 3.12- Figure 3.13 show that the direct controllers used to regulate AC power and AC voltage are working as expected. The AC power controller has been tuned with a large time constant so that it does not

vary rapidly. As expected, the voltage and power affect each other in this mode of control. The line current plot of Figure 3.14 indicates that the peak inrush current is about 25 A, which is much lower than the rated peak current of 93 A. Therefore, the breakers with pre-insertion resistors and the startup mechanism have worked to provide the intended service. Figure 3.15 shows that the capacitor voltages do not exceed their normal operating values during startup and arrive at steady state voltage of 80 V in normal operation. The battery currents shown in Figure 3.16 show that only the inductor current ripple is present on top of the DC component. The DC-DC converter has been able to eliminate the large fundamental frequency component available at AC side from penetrating into the battery. Figure 3.17 indicates that SOC of batteries in top and bottom SMs decay equally with time due to SOC balancing controllers. Finally, Figure 3.18 shows that the DC power suppression controller has regulated the power transfer from the DC link to zero and the MMC operates with an efficiency of 95.5% (this figures excludes switching losses that are not modeled).

3.8 Summary

In this chapter, the AC voltage controller and the active power controller used in the thesis were discussed in detail. The controller design process to regulate the capacitor voltage was also presented. The protection scheme introduced the breakers and relays used to isolate AC grid, DC link, and batteries at different moments. A startup procedure to charge the capacitors and limit any inrush current was presented. Finally, an example single-phase MMC with BESS was given along with its component values. The converter was simulated in PSCAD/EMTDC and the operation of each control aspect was validated via simulation analysis.

Chapter 4: Detailed Equivalent Model of the Multivalve

4.1 Fundamentals of EMT Simulation

An electrical network is a collection of resistors, inductors, capacitors, voltage and current sources, switches, dynamic devices, etc. To observe and understand transient behavior of these networks, ElectroMagnetic Transients (EMT) simulations are carried out. Since transients often include high frequencies (in the kHz range), the simulation of these networks needs to be carried out with a particularly small-time step, normally in the order of a few micro-seconds.

The basis of an EMT simulation is to convert the complex electrical network into a network consisting only of conductances and current sources [32]. Sections 4.1.1 to 4.1.4 show how to represent a resistance, inductance, capacitance, and a switch by their admittance and current source combination. Models for dynamic devices and other elements have been developed and are well documented [32].

4.1.1 Representation of a Resistor

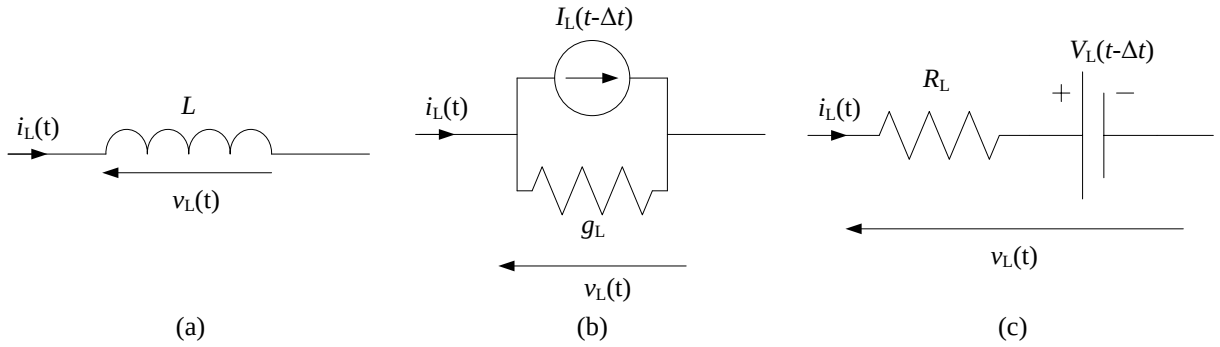


Figure 4.1: Representation of resistor (a) general (b) equivalent conductance.

The conductance is the reciprocal of the resistance (its admittance and conductance are equal since admittance is only real).

$$Y = G = \frac{1}{R} \tag{4.1}$$

4.1.2 Representation of an Inductor



(a) (b) (c)

Figure 4.2: Representation of an inductor (a) general (b) Norton equivalent circuit (c) Thevenin equivalent circuit.

The voltage across an inductor can be written as follows.

$$v_L = L\frac{di_L}{dt} \tag{4.2}$$

Hence the inductor current can be calculated as follows.

$$i_L(t) = \frac{1}{L}\int_{\tau=0}^{t} v_L(\tau)d\tau + i_L(0) \tag{4.3}$$

To determine the inductor current at each time step, the inductor voltage is integrated over the time step. The trapezoidal method is used for the integration for its accuracy and also its ability to preserve stability for linear systems [33]. Trapezoidal method applied to integrate a general function $f(t)$ over a Δx period is shown in (4.4). The expression after applying trapezoidal rule to (4.3) is presented in (4.5), where Δt is the simulation time step.

$$\int_{t=x-\Delta x}^{x} f(t)dt \approx \frac{f(x)+f(x-\Delta x)}{2}\cdot\Delta x \tag{4.4}$$

$$i_L(t) = i_L(t-\Delta t) + \frac{1}{L}\left(\frac{v_L(t)+v_L(t-\Delta t)}{2}\right)\cdot\Delta t \tag{4.5}$$

Rearranging terms of (4.5) yields

$$i_{\mathrm{L}}(t)=\left(\frac{\Delta t}{2L}\right)v_{\mathrm{L}}(t)+\left\{i_{\mathrm{L}}(t-\Delta t)+\frac{\Delta t}{2L}v_{\mathrm{L}}(t-\Delta t)\right\} \tag{4.6}$$

which may be written as

$$i_{\mathrm{L}}(t)=g_{\mathrm{L}}v_{\mathrm{L}}(t)+I_{\mathrm{L}}(t-\Delta t) \tag{4.7}$$

where g_{L} is the equivalent conductance and $I_{\mathrm{L}}(t\text{-}\Delta t)$ is the equivalent current source in parallel to the conductance as shown in Figure 4.2(b). The magnitude of the current source is solely dependent on the inductor current and voltages of the previous time step. Thus, the current source is also known as the "history term" in general.

The Norton equivalent circuit of the inductor shown in Figure 4.2(b) can be also represented as a Thevenin voltage equivalent. Equation (4.6) can be manipulated to represent it as a voltage source.

$$v_{\mathrm{L}}(t)=\left(\frac{2L}{\Delta t}\right)i_{\mathrm{L}}(t)+\left\{-\frac{2L}{\Delta t}i_{\mathrm{L}}(t-\Delta t)-v_{\mathrm{L}}(t-\Delta t)\right\} \tag{4.8}$$

which is

$$v_{\mathrm{L}}(t)=R_{\mathrm{L}}i_{\mathrm{L}}(t)+V_{\mathrm{L}}(t-\Delta t) \tag{4.9}$$

R_{L} is the Thevenin resistor and $V_{\mathrm{L}}(t\text{-}\Delta t)$ is the Thevenin voltage source. This representation is shown in Figure 4.2(c).

4.1.3 Representation of a Capacitor

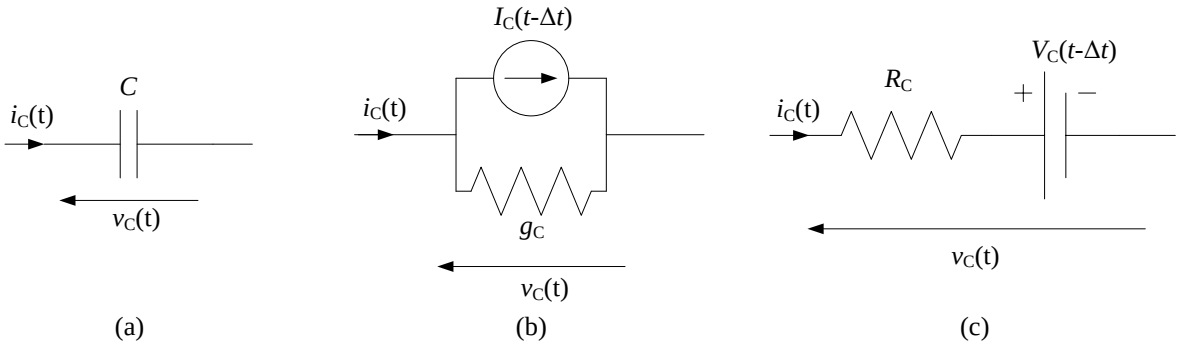


Figure 4.3: Representation of a capacitor (a) general (b) Norton equivalent circuit (c) Thevenin equivalent circuit.

The current through a capacitor can be represented as in (4.10).

$$i_C(t) = C\frac{dv_C(t)}{dt} \tag{4.10}$$

Integrating the capacitor current over the simulation time step as in Section 4.1.2 yields

$$v_C(t) = v_C(t-\Delta t) + \frac{1}{C}\left(\frac{i_C(t)+i_C(t-\Delta t)}{2}\right)\cdot\Delta t \tag{4.11}$$

$$i_C(t) = \left(\frac{2C}{\Delta t}\right)v_C(t) + \left\{-i_C(t-\Delta t) - \frac{2C}{\Delta t}v_C(t-\Delta t)\right\} \tag{4.12}$$

which may be written as

$$i_C(t) = g_C v_C(t) + I_C(t-\Delta t) \tag{4.13}$$

where g_C is the equivalent conductance and $I_C(t\text{-}\Delta t)$ is the equivalent current source in parallel to the conductance as shown in Figure 4.3(b). Similar to the inductor, the Thevenin equivalent circuit of the capacitor can be derived from (4.12).

$$v_C(t) = \left(\frac{\Delta t}{2C}\right)i_C(t) + \left\{\frac{\Delta t}{2C}i_C(t-\Delta t) + v_C(t-\Delta t)\right\} \tag{4.14}$$

which may be shown as

$$v_C(t) = R_C i_C(t) + V_C(t-\Delta t) \tag{4.15}$$

R_C is the Thevenin resistor and $V_C(t-\Delta t)$ is the Thevenin voltage source. This representation is shown in Figure 4.3(c).

4.1.4 Representation of a Power Electronic Switch

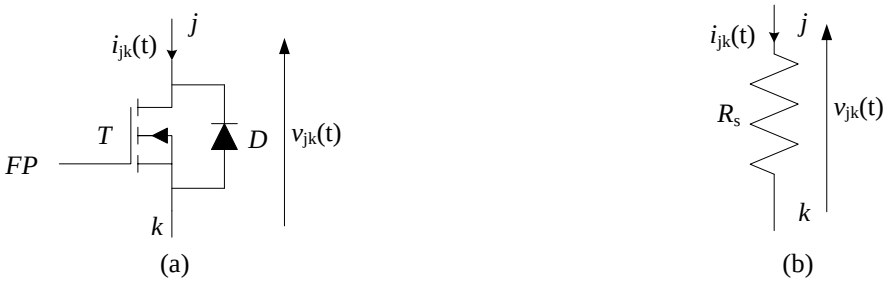


Figure 4.4: MOSFET with an anti-parallel diode (a) general (b) model in EMT.

A power electronic switch operates in its saturated on and off states. For an ideal switch, the voltage across the switch ($v_{jk}(t)$) is zero when the switch is on (saturated state) and the switch current ($i_{jk}(t)$) is a finite value. When the switch is off, the current is zero and the voltage across the switch is a finite value. These are the only operating conditions of a switch if the short-term transients during state transitions are ignored. Therefore, the switch can be ideally represented as an infinite conductance (zero resistance) when on and a zero conductance (infinite resistance) when off. However, in real switches, there is a small current through the switch when the switch is off, and a small voltage difference exists across the switch when the switch is on. Therefore, the switch is modeled as a large conductance (small resistance R_{on}) when the switch is on and a small conductance (large resistance R_{off}) when the switch is off.

A MOSFET is turned on when the voltage across its source-drain is positive and a firing pulse (*FP*) is present at its gate (*FP* = 1). The MOSFET turns off when the *FP* is taken away (*FP* = 0). However, in a MOSFET with an anti-parallel diode (Figure 4.4(a)), the diode may turn on if the switch current i_{jk} is negative. Therefore, to determine the proper resistance of the switch used

in the EMT model (Figure 4.4(b)), a state transition diagram shown in Figure 4.5 needs to be implemented.

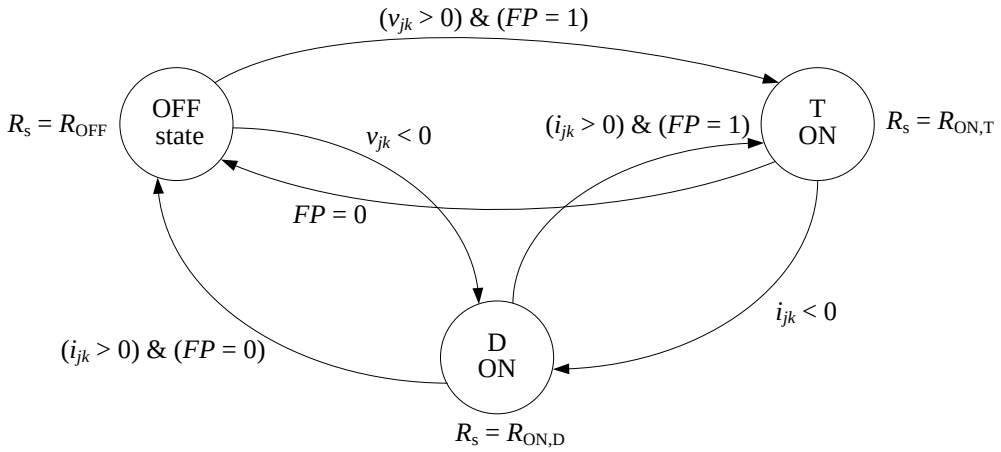


Figure 4.5: State transition diagram for a MOSFET.

4.1.5 EMT Solution of an Electric Network

The circuit shown in Figure 4.6 is used as an example to demonstrate the EMT solution process.

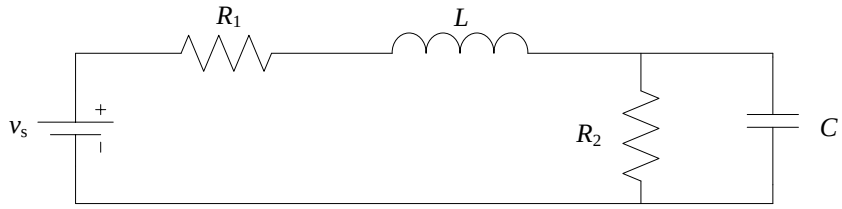


Figure 4.6: Example network.

Initially, the electrical network is represented using only admittances and current sources. The voltage source can be converted to a current source using the series resistor R_1 (Modified Nodal Analysis (MNA) presents a method to use an ideal voltage source in EMT simulations when a series resistor is not present [34]). Figure 4.7 shows the network presented using admittances and current sources only.

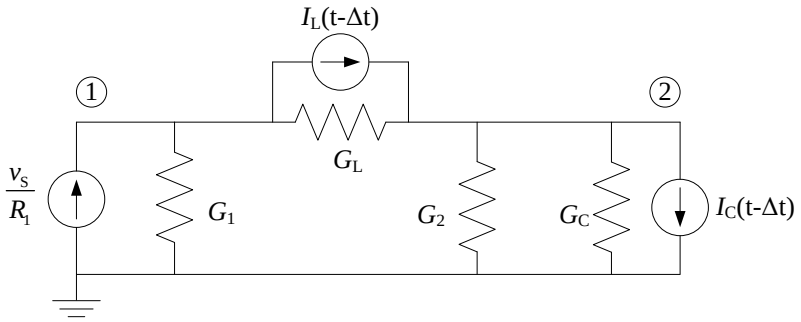


Figure 4.7: Admittance circuit of the example network.

KCL equations are written for each node except the ground node (ground node may be selected as any node in the circuit.) In Figure 4.7, v_x denotes the voltage of node x relative to the ground.

KCL for node 1

$$G_1 v_1 + G_L\left(v_1 - v_2\right) - \frac{v_S}{R_1} + I_L\left(t - \Delta t\right) = 0 \tag{4.16}$$

or

$$\left(G_1 + G_L\right) v_1 - G_L v_2 = \frac{v_S}{R_1} - I_L\left(t - \Delta t\right) \tag{4.17}$$

KCL for node 2

$$G_C v_2 + G_2 v_2 + G_L\left(v_2 - v_1\right) + I_C\left(t - \Delta t\right) - I_L\left(t - \Delta t\right) = 0 \tag{4.18}$$

or

$$-G_L v_1 + \left(G_2 + G_L + G_C\right) v_2 = I_L\left(t - \Delta t\right) - I_C\left(t - \Delta t\right) \tag{4.19}$$

The equations (4.17) and (4.19) have a general structure. For node 1, it is as follows.

$$\begin{aligned} &v_1\left(\text{sum of all conductances incident on node 1}\right) \\ &+v_2\left(\text{-conductances between node 1 and 2}\right) = \text{Current source incident at node 1} \end{aligned} \tag{4.20}$$

Using (4.17) and (4.19), the admittance matrix for the circuit can be formed as follows.

$$\begin{pmatrix} (G_1+G_L) & -G_L \\ -G_L & (G_2+G_L+G_C) \end{pmatrix} \begin{pmatrix} v_1 \\ v_2 \end{pmatrix} = \begin{pmatrix} \frac{v_S}{R_1} - I_L(t-\Delta t) \\ I_L(t-\Delta t) - I_C(t-\Delta t) \end{pmatrix} \quad (4.21)$$

Equation (4.21) is in the standard form as in (4.22) with **Y** being the admittance matrix, **V** being the node voltage and **J** being the current vector incident on the node.

$$\mathbf{YV} = \mathbf{J} \quad (4.22)$$

The voltage at each node at time *t* can be obtained by solving (4.22) as shown in (4.23). After obtaining the voltage vector, the new branch currents for the time instant ($t+\Delta t$) can be calculated. The voltage vector for ($t+\Delta t$) is calculated by solving (4.22) again with the current vector at ($t+\Delta t$). This process is continued until the simulation duration expires.

$$\mathbf{V} = \mathbf{Y}^{-1}\mathbf{J} \quad (4.23)$$

4.2 EMT Model of the Battery

A battery is a chemical energy storage equipment. Various kinds of batteries are available in the market. However, all of them can be basically modeled as a DC voltage source behind a resistor. When the battery is drained, the chemical energy stored in the battery reduces, and thus the voltage produced by the battery decays. In systems that consider the energy provided by a BESS, proper emulation of this voltage decay is important. To keep track of the discharge of the battery, its state of charge (SOC) is used. SOC is actually the percentage energy available in the battery (full SOC= 100%, empty SOC = 0%). Different methods such as chemical and voltage methods, coulomb counting, and Kalman filtering methods are available to measure the SOC of a battery [35]. Coulomb counting is one of the easiest methods to determine the SOC with relatively good accuracy. This method integrates the current drawn from the battery over time and determines

the SOC. For a battery with Q_{full} capacity in Ampere-hours (Ah) with a current $i(t)$ drawn from the battery, the SOC can be represented as (4.24).

$$SOC = \frac{Q_{\text{full}} - \int i(t)dt}{Q_{\text{full}}} \times 100\% \tag{4.24}$$

Depending on the battery chemistry, each battery type has a unique discharge curve. Different battery models based on SOC have been developed to obtain the discharge characteristics of batteries [36]. Shepherd model [37], [38] is a battery model capable of representing the discharge characteristics with a reasonably high level of accuracy. The battery voltage based on Shepherd model can be represented as in (4.25).

$$v_{\text{bat}} = E_0 - K\frac{Q_{\text{full}}}{Q_{\text{full}} - \int i(t)dt} + Ae^{-B\int i(t)dt} \tag{4.25}$$

where E_0, K, A, and B are the battery constant voltage, polarization constant, exponential voltage amplitude constant, and time constant inverse respectively. The equations (4.26) – (4.30) derive the relationship between parameters found on a typical discharge curve of a battery (Figure 4.8) and the above constants. Reference [38] gives a detailed description of these constants.

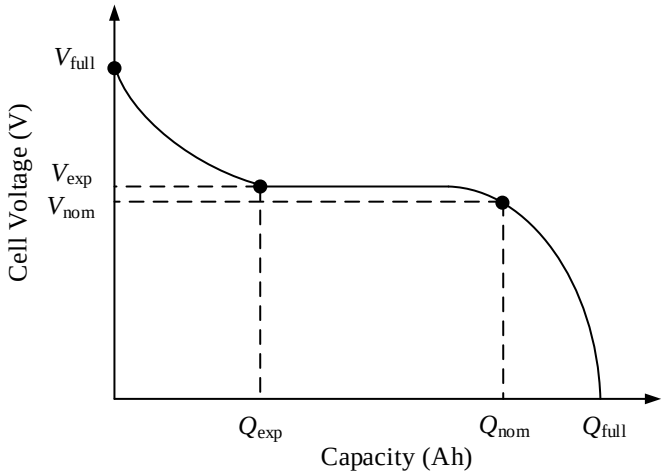


Figure 4.8: Typical battery discharge curve.

$$A = V_{\text{full}} - V_{\text{exp}} \tag{4.26}$$

$$B = \frac{2.3}{Q_{\text{exp}}} \tag{4.27}$$

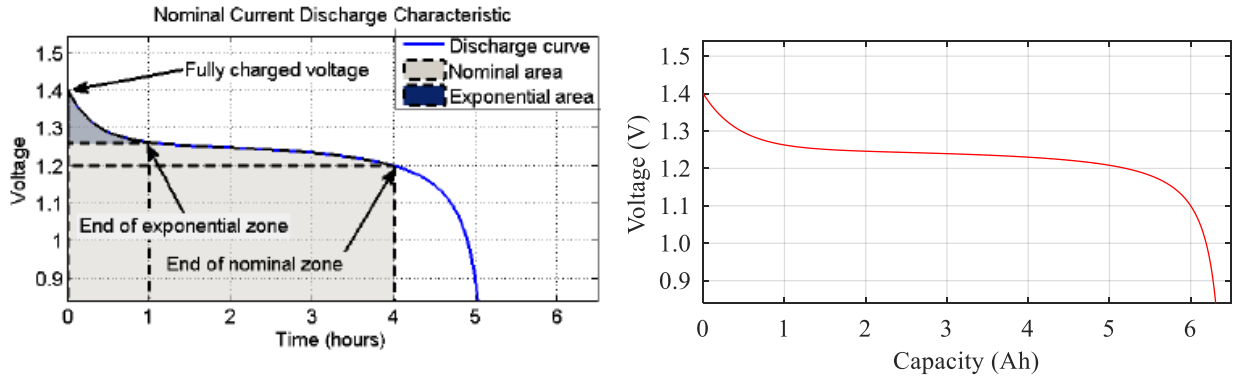
$$K = 0.065 * \left[V_{\text{full}} - V_{\text{nom}} + A\left(e^{-B \bullet Q_{\text{nom}}} - 1\right) \right] * \frac{Q_{\text{full}} - Q_{\text{nom}}}{Q_{\text{nom}}} \tag{4.28}$$

$$R_{\text{bat}} = V_{\text{nom}} \left(\frac{1 - v}{0.2 * Q_{\text{nom}}} \right) \tag{4.29}$$

$$E_0 = V_{\text{full}} + K + R_{\text{bat}} * i - A \tag{4.30}$$

In these equations, R_{bat}, v, and i are the battery internal resistance, battery efficiency and the nominal current used to test the steady-state discharge of the battery. Q_{exp} and Q_{nom} are the discharged capacity at V_{exp} and V_{nom} respectively as shown in Figure 4.8.

Using (4.26)–(4.30) a battery can be accurately modeled using its discharge curve. An EMT program can be simply written to control the voltage of a voltage source behind the internal resistance R according to (4.25). The discharge curve of Panasonic HHR650D3 NiMH battery was simulated using the developed EMT model. Figure 4.9 shows the discharge curve of the battery obtained by the reference [37] and the EMT model.



(a) (b)

Figure 4.9: Battery discharge curve (a) figure taken from [37] (b) EMT model.

The model perfectly tracks the voltage in the start of discharge and at the mid region. However, it shows some deviation when the battery is close to full discharge. This may be due to the high discharge current used in EMT simulation to obtain results within a reasonable simulation time and errors in extracting V_{nom}, V_{exp}, Q_{nom} and Q_{exp}.

4.3 Derivation of the Thevenin Equivalent Circuit of a Multivalve

For EMT simulation of an MMC with BESS, the full electric network composed of capacitors, inductors, switches, and voltage sources needs to be converted to an admittance matrix based on the theory discussed in Sections 4.1 and 4.2. Since an MMC with BESS has a considerable number of SMs, and at least four switches in each SM, this will form a large admittance matrix. This matrix needs to be reinverted whenever any change in the admittance at any branch occurs. Since switching of SMs and the DC-DC converter happens at high frequencies, it calls for an excessive number of admittance matrix inversions during the simulation period. To fulfill this, a massive computational power is required, and the cost of simulation will be high.

As a solution for this burden, the multivalve in the MMC with BESS can be reduced to a single Thevenin voltage source behind a Thevenin impedance without losing any information available in a detailed EMT implementation of a multivalve. The rest of Section 4.3 presents the derivation of the detailed equivalent model and its validation.

The schematic diagram of a typical half-bridge SM with energy storage is shown in Figure 4.10. This schematic diagram can also be represented using EMT equivalent Thevenin voltage sources and resistances (see Section 4.1 and 4.2) as in Figure 4.11. The simulation time step is Δt.

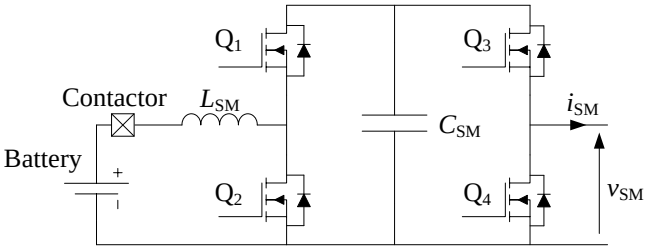


Figure 4.10: Half-bridge SM with storage.

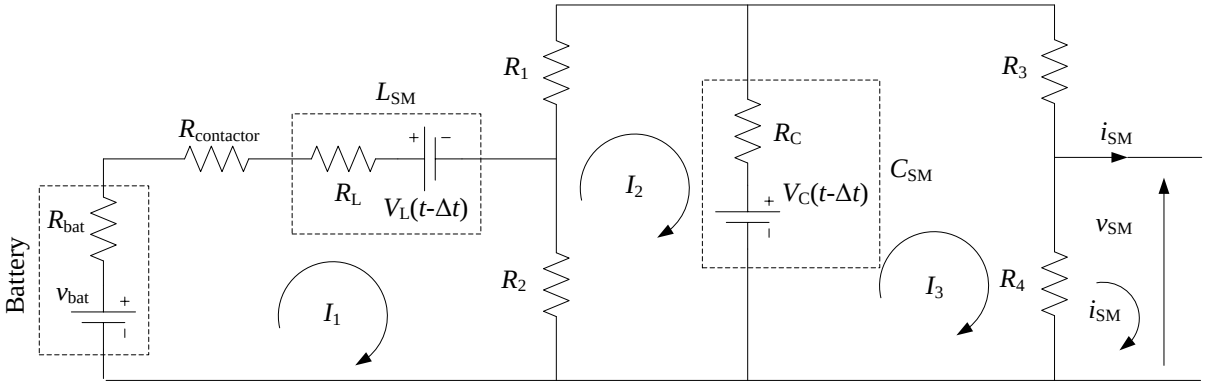


Figure 4.11: EMT equivalent SM.

In Figure 4.11 $R_{\mathrm{L}} = \dfrac{2L_{\mathrm{SM}}}{\Delta t}$ and $R_{\mathrm{C}} = \dfrac{\Delta t}{2C_{\mathrm{SM}}}$. The Thevenin equivalent resistance of the SM is the equivalent resistance seen across the output of the SM when all the voltage sources are short-circuited as shown in Figure 4.12.

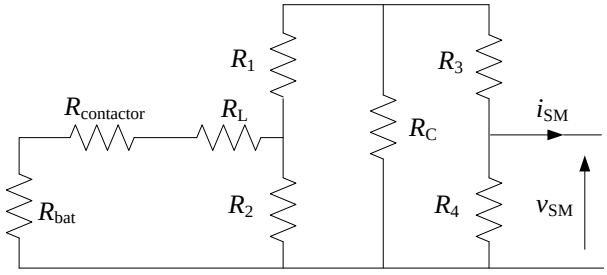


Figure 4.12: SM with only the resistances to calculate Thevenin resistance.

The SM Thevenin resistance $R_{\mathrm{SM,thev}}$ is as in (4.31).

$$R_{\mathrm{SM,thev}} = R_4 \,//\left\{R_3 + \left[R_{\mathrm{C}} \,//\left(R_1 + \left\{R_2 \,//\left[R_{\mathrm{bat}} + R_{\mathrm{contactor}} + R_{\mathrm{L}}\right]\right\}\right)\right]\right\} \tag{4.31}$$

The value of the Thevenin equivalent voltage source is the SM open circuit voltage across R_4 (i_{SM} = 0). This can be done by first solving the loop currents I_1, I_2 and I_3 of Figure 4.11.

For loop 1

$$\underbrace{\left(R_{bat}+R_{contactor}+R_L+R_2\right)}_{a}I_1-R_2I_2=v_{bat}-V_L\left(t-\Delta t\right) \tag{4.32}$$

For loop 2

$$R_2I_1-\underbrace{\left(R_C+R_2+R_1\right)}_{b}I_2+R_CI_3=V_C\left(t-\Delta t\right) \tag{4.33}$$

For loop 3

$$R_CI_2-\underbrace{\left(R_3+R_4+R_C\right)}_{c}I_3=-V_C\left(t-\Delta t\right)-R_4i_{SM} \tag{4.34}$$

Solving (4.32 – 4.34)

$$I_1=\frac{v_{bat}-V_L(t-\Delta t)}{a}+\frac{R_2}{a}d \tag{4.35}$$

$$I_2=d \tag{4.36}$$

$$I_3=\frac{V_C(t-\Delta t)+R_4i_{SM}}{c}+\frac{R_C}{c}d \tag{4.37}$$

where

$$d=\frac{a\left(c-R_C\right)V_C(t-\Delta t)-cR_Cv_{bat}+cR_CV_L(t-\Delta t)-aR_CR_4i_{SM}}{cR_2^2-abc+aR_C^2} \tag{4.38}$$

For open circuit SM (i_{SM} = 0)

$$I_1=\frac{v_{bat}-V_L(t-\Delta t)}{a}+\frac{R_2}{a}e \tag{4.39}$$

$$I_2=e \tag{4.40}$$

$$I_3 = \frac{V_C(t-\Delta t)}{c} + \frac{R_C}{c} e \tag{4.41}$$

where

$$e = \frac{a\left(c - R_C\right)V_C(t-\Delta t) - cR_C v_{bat} + cR_C V_L(t-\Delta t)}{cR_2^2 - abc + aR_C^2} \tag{4.42}$$

thus

$$v_{SM,thev} = R_4 I_3 = R_4\left[\frac{V_C(t-\Delta t)}{c} + \frac{R_C}{c} e\right] \tag{4.43}$$

The Thevenin equivalent of an SM is achieved as above. The multivalve of the MMC is a series connection of SMs as shown in Figure 4.13. The Thevenin equivalent of the multivalve can be achieved by summing up the individual Thevenin voltage sources and Thevenin resistances of each SM, respectively (4.44 and 4.45).

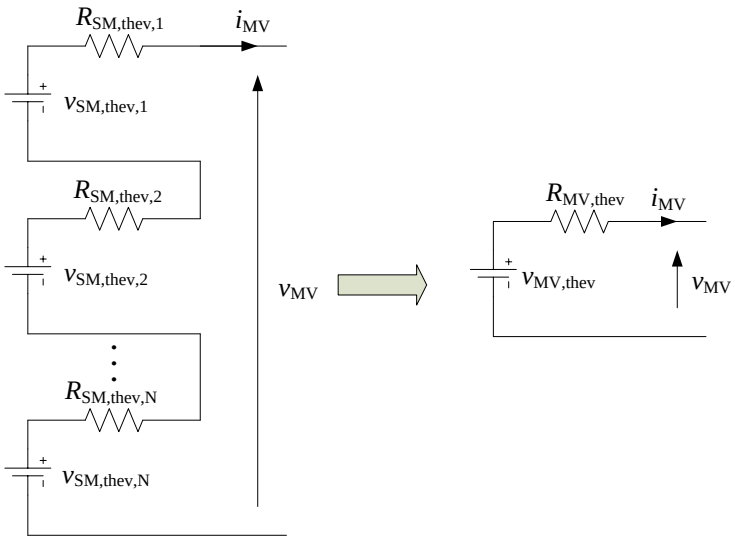


Figure 4.13: Thevenin equivalent circuit of a multivalve.

$$v_{MV,thev} = \sum_{i=1}^{N} v_{SM,thev,i} \tag{4.44}$$

$$R_{MV,thev} = \sum_{i=1}^{N} R_{SM,thev,i} \tag{4.45}$$

Therefore, a single voltage source behind a resistor is introduced to the EMT solver to represent the multivalve. This process will greatly reduce the number of nodes in the electrical network and thus the admittance matrix.

Even though the network is simplified to a simple voltage source behind a resistor, no details about the individual SMs is lost. The EMT solver outputs the multivalve current (i_{MV}) during the solution process. Since all the SMs are placed in series, the multivalve current is actually the SM's current. Based on (4.35) – (4.37) and the stored information of resistor values, the loop currents (I_1, I_2, and I_3) in each SM can be individually calculated. Therefore, any parameter in the SM can be easily calculated. For instance, the SM inductor current (i_{L}) and SM capacitor voltage (v_{C}) are calculated as shown in (4.46) and (4.47).

$$i_{\mathrm{L}} = I_1 \tag{4.46}$$

$$v_{\mathrm{C}} = V_{\mathrm{C}}(t - \Delta t) + R_{\mathrm{C}}\left(I_2 - I_3\right) \tag{4.47}$$

4.4 Comparison and Validation of the Detailed Equivalent Model of MMC Multivalve

The accuracy of the model developed in Section 4.3 is verified against a detailed switching implementation of the MMC with BESS. The PSCAD/EMTDC v4.6.2 was used to validate the model. The model was developed in FORTRAN as a custom component inside the PSCAD software. The model is validated in steady-state operation, AC power control reference change, AC line solid line-to-ground fault, and a fault occurring inside a multivalve where two SMs interconnect. The same MMC described in Section 3.7 is used for validation purposes.

4.4.1 Comparison at Steady State

The single phase MMC representations developed both in detailed switching model and in detailed equivalent model were allowed to arrive at steady state. Then the parameters were compared with each other. Figure 4.14(a)-(f) show the MMC terminal voltages, AC voltage at the PCC, and AC line current. Complete overlap of these waveforms were observed (the results are separately plotted to show the two waveforms distinctly). Average capacitor voltages shown in Figure 4.15 show perfect conformity in predicting capacitor voltage.

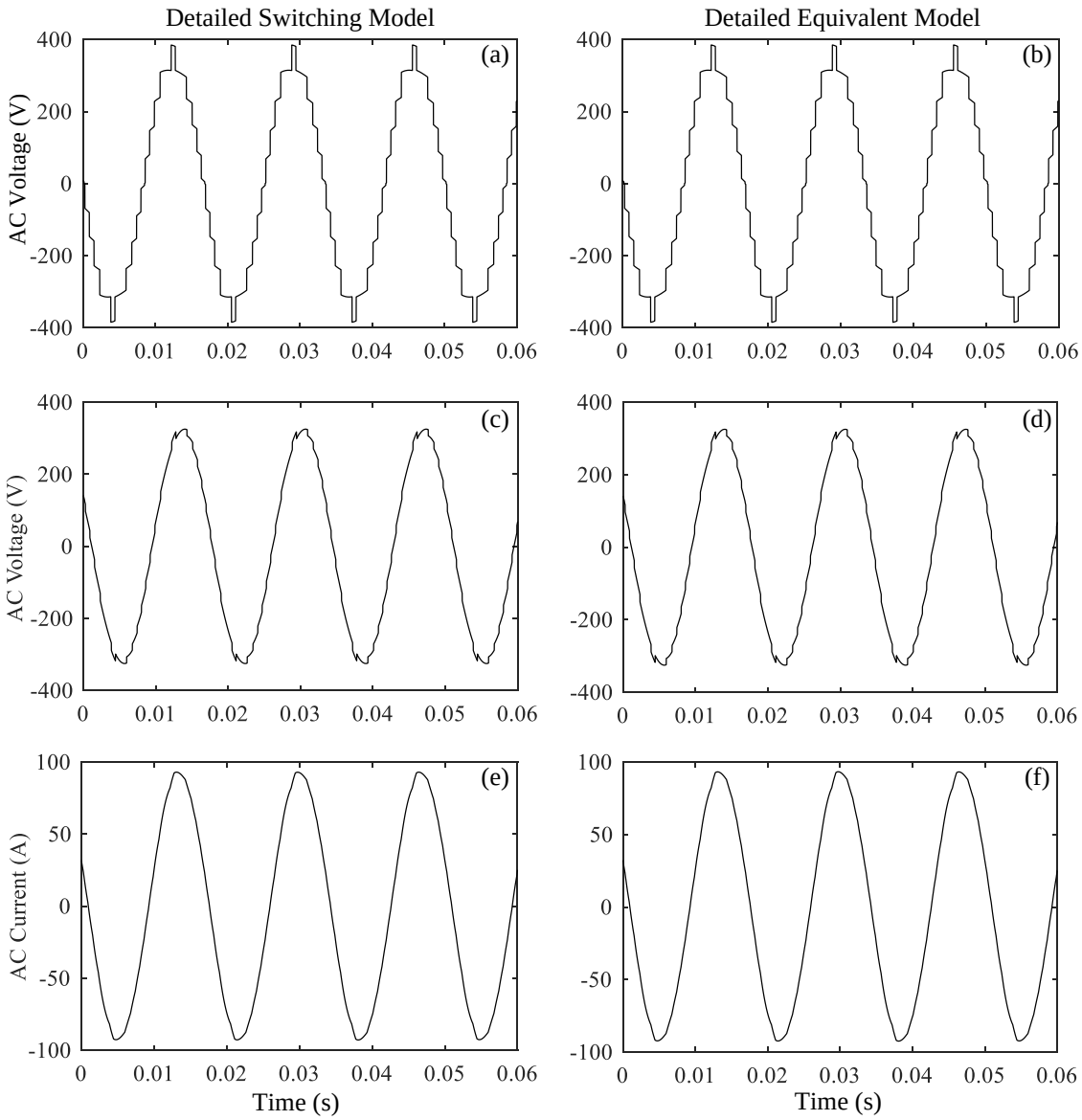


Figure 4.14: Comparison at steady state: (a)-(b) MMC AC terminal voltage, (c)-(d) Voltage at PCC, (e)-(f) AC line current.

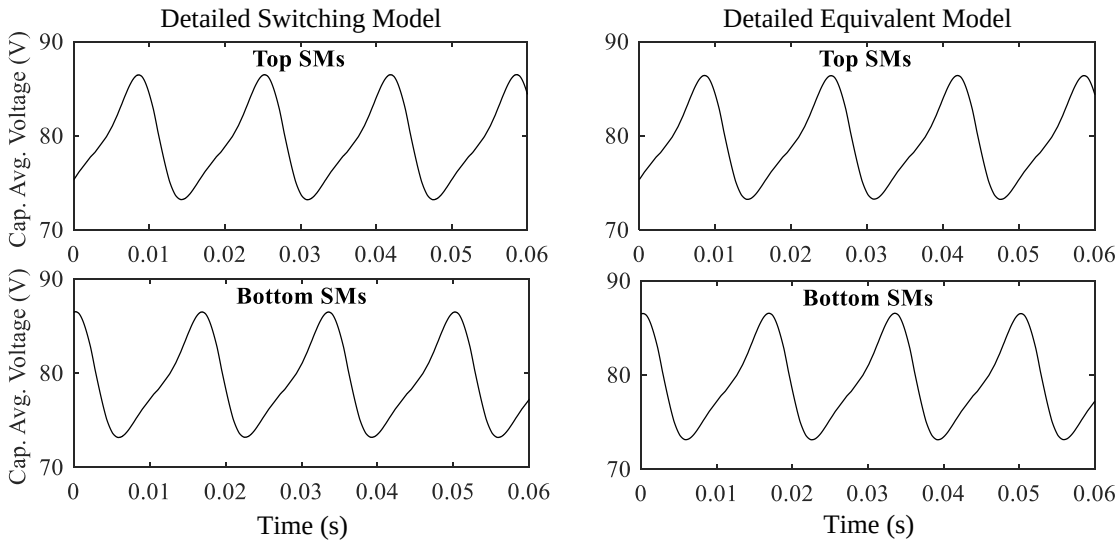


Figure 4.15: Comparison of average capacitor voltages at steady state.

4.4.2 Comparison with an AC Power Reference Change

The MMC was tested for a change in one controller reference. The response to a power command step change from 15 kW to 10 kW was used to check whether or not the detailed equivalent model accurately tracks the transient occurring due to a control command change. Figure 4.16 show the active power variation, RMS voltage variation, and converter terminal voltage when the power reference change. It could be observed that the detailed equivalent model tracks the transients perfectly. Similarly Figure 4.17 and Figure 4.18 show the average capacitor voltage and average battery current. The model is capable of tracking the capacitor voltage and battery current during transient.

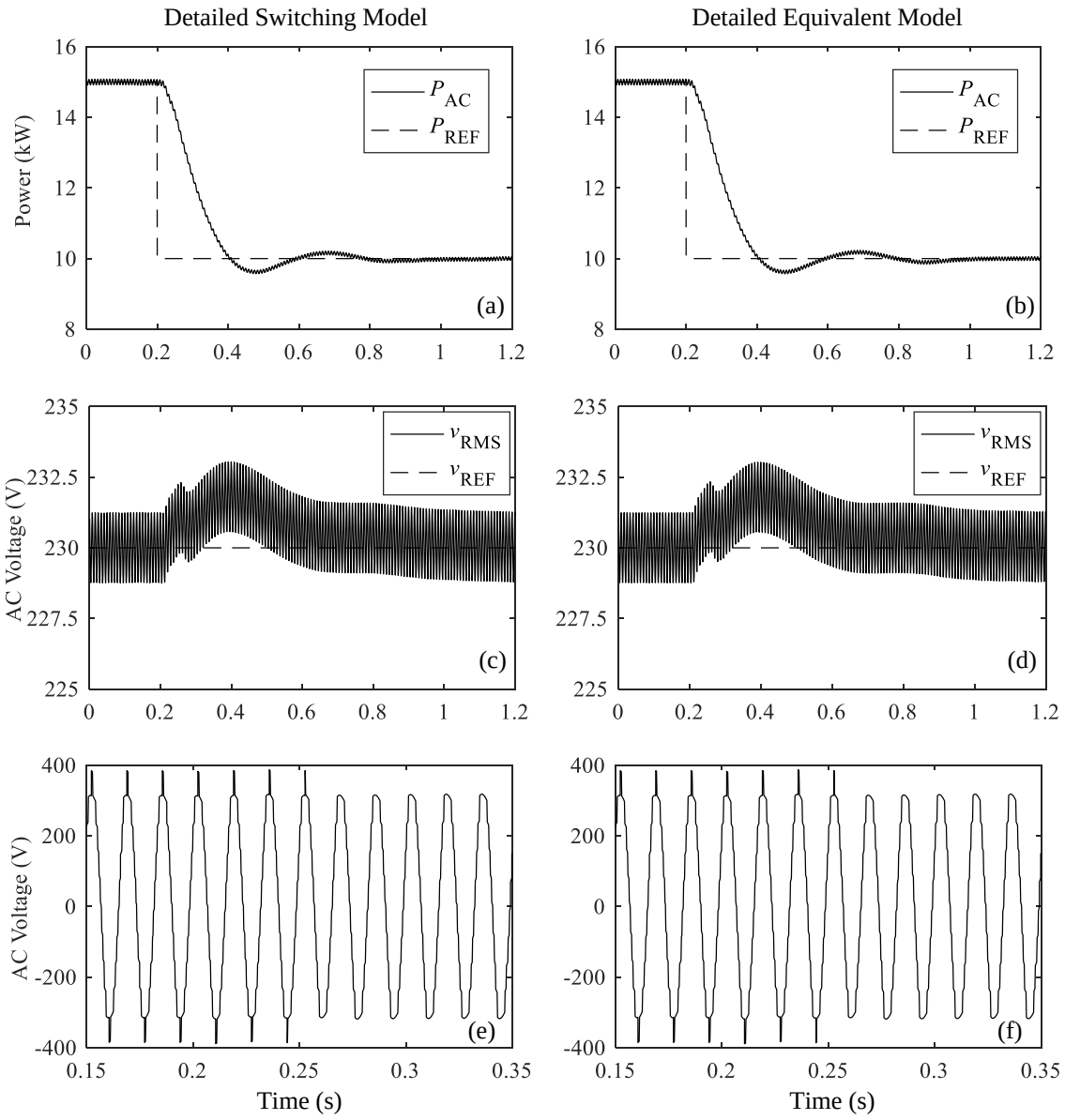


Figure 4.16: Comparison at power reference change: (a)-(b) Active power, (c)-(d) RMS voltage at PCC, (e)-(f) AC voltage at converter terminal.

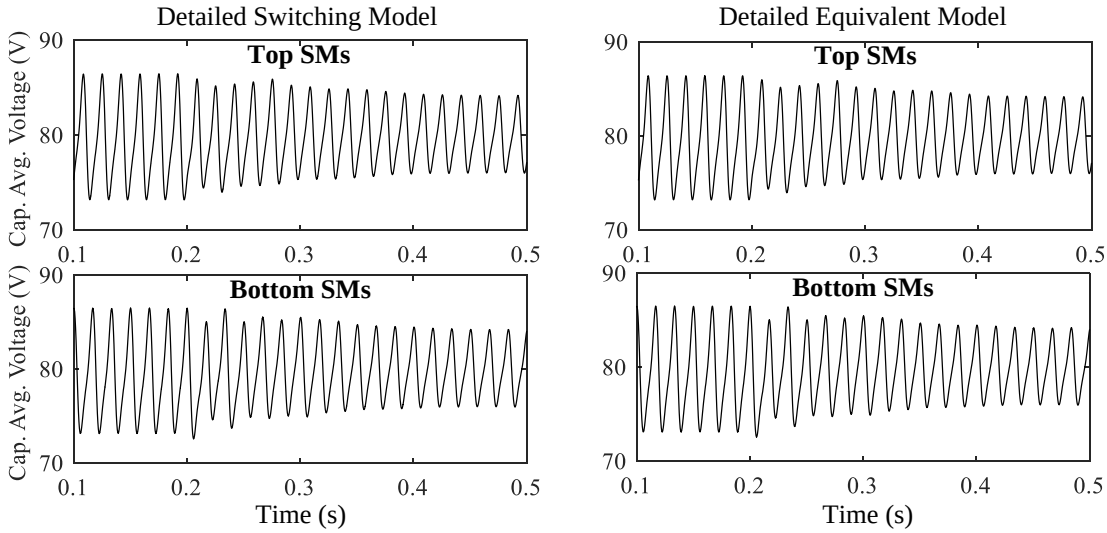


Figure 4.17: Comparison of average capacitor voltages when power reference change.

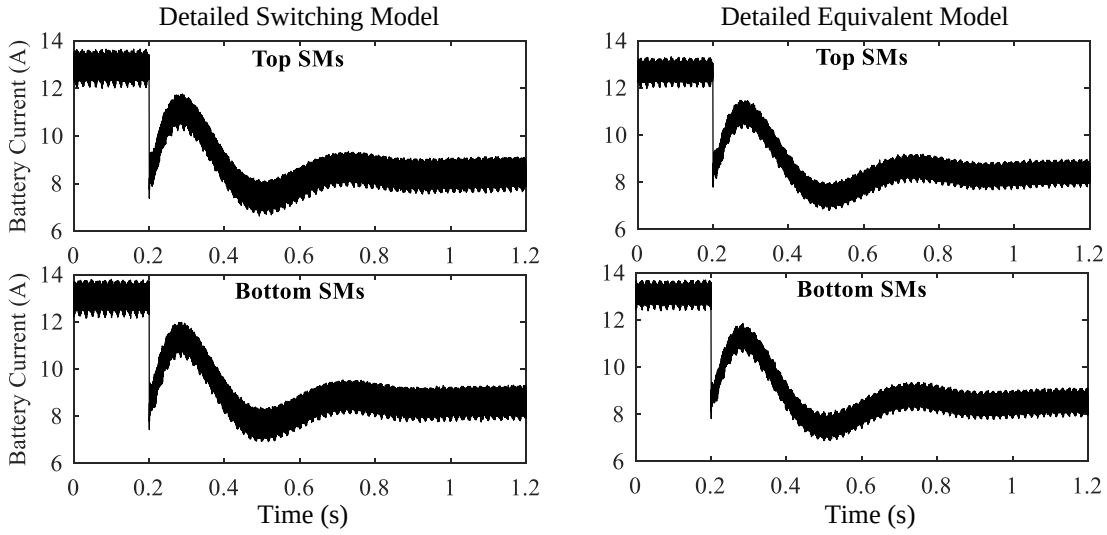


Figure 4.18: Comparison of average battery current when power reference change.

4.4.3 Comparison with a Solid Line-to-Ground Fault at PCC

One of the most important studies in EMT simulation of power systems is the study of the transients resulting from a fault in the system. For the true use of the model, the faults should be tracked exactly as they determine the converter's capability, converter design considerations, etc. For validating the performance during a fault, a solid line-to-ground (LG) fault for a duration of 0.05 s was applied at 0.2 s at the PCC. Figure 4.19 to Figure 4.21 show the AC voltages, AC

currents, average capacitor voltages, and average battery currents, respectively, around the fault time. The high-frequency transients caused by the fault are perfectly tracked in every aspect.

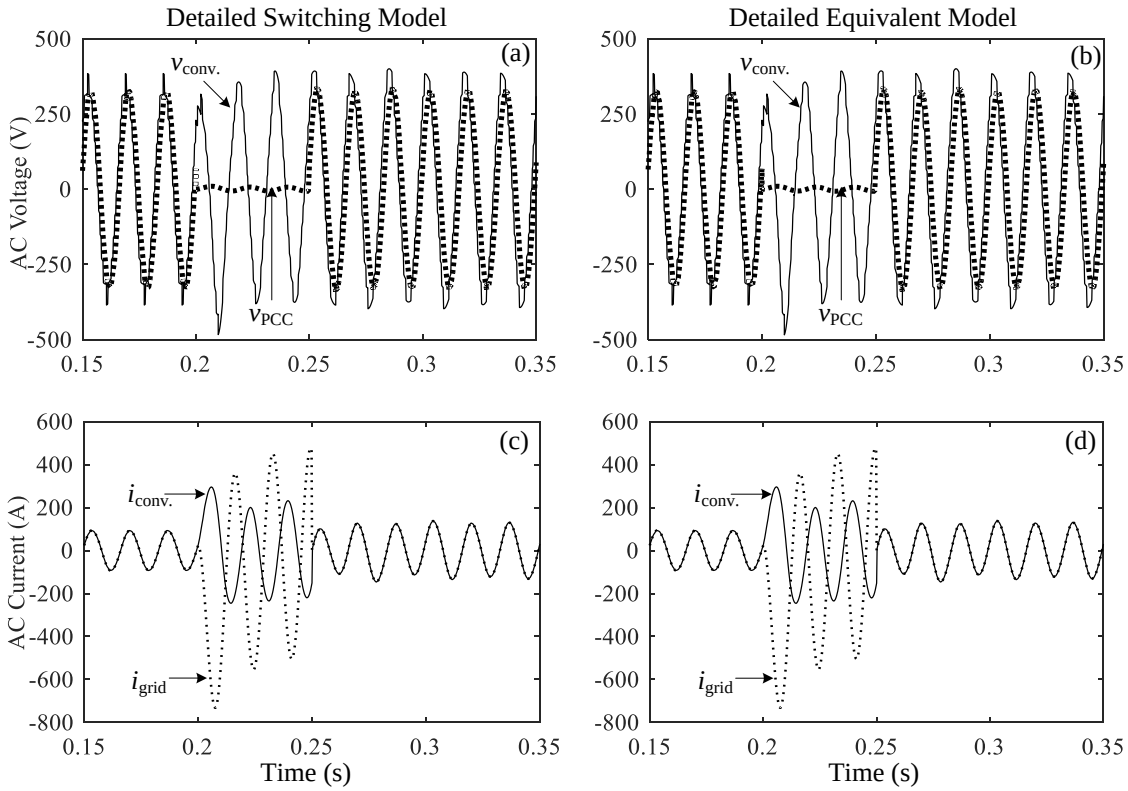


Figure 4.19: Comparison at line-to-ground fault: (a)-(b) converter voltage ($v_{conv.}$) and PCC voltage (v_{PCC}), (c)-(d) converter current ($i_{conv.}$) and current from grid (i_{grid})

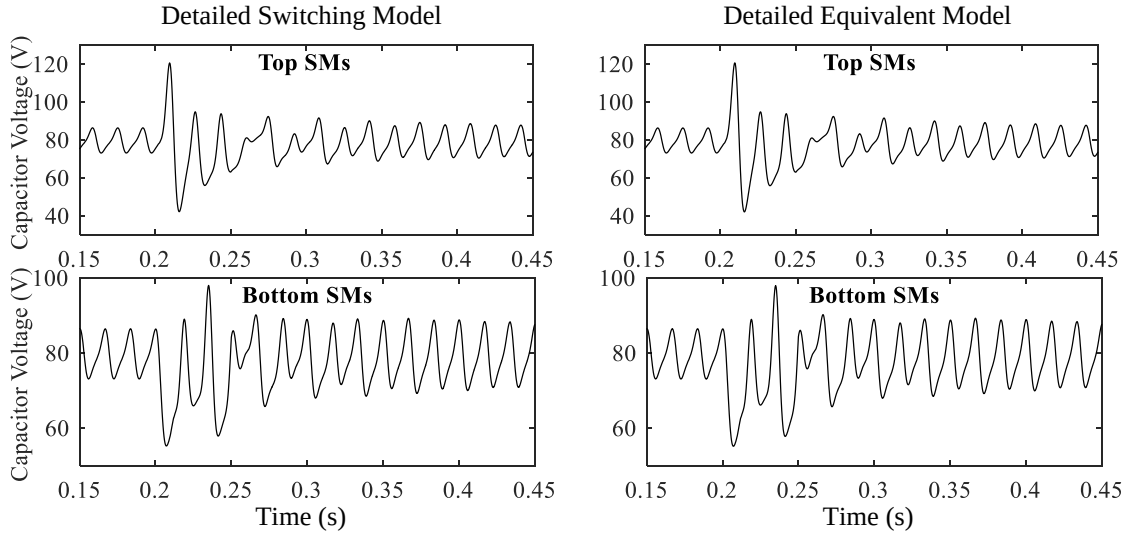


Figure 4.20: Comparison of average capacitor voltages during line-to-ground fault.

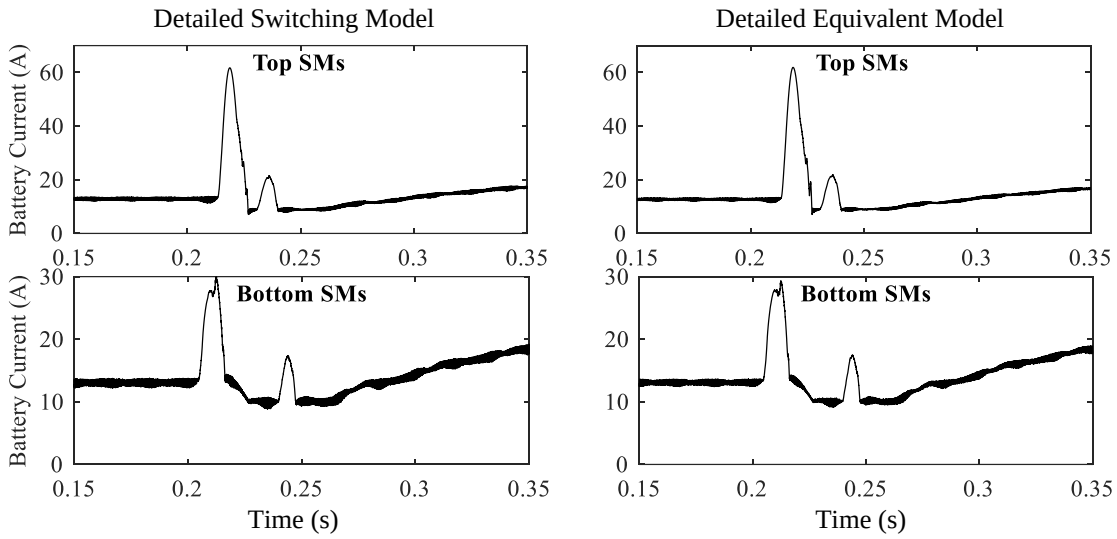


Figure 4.21: Comparison of average battery current during a line-to-ground fault

4.4.4 Fault at the Middle of the Multivalve.

A solid fault to ground is implemented in the top multivalve between the connection from 5th SM to the 6th SM. The fault was added to the detailed equivalent model case by implementing the first 5 SMs and the second 5 SMs separately using the detailed equivalent model. This simulation experiment shows that the detailed observations can still be made within the multivalve, even though the detailed equivalent model compresses the whole multivalve. Figure 4.22 to Figure 4.24 show the AC voltage, AC current, capacitor voltages, and battery currents. Transients due to the fault are captured accurately by the detailed equivalent model. The separate capacitor voltages and battery currents of each SM are shown in this example as their behavior is not uniform across the multivalve.

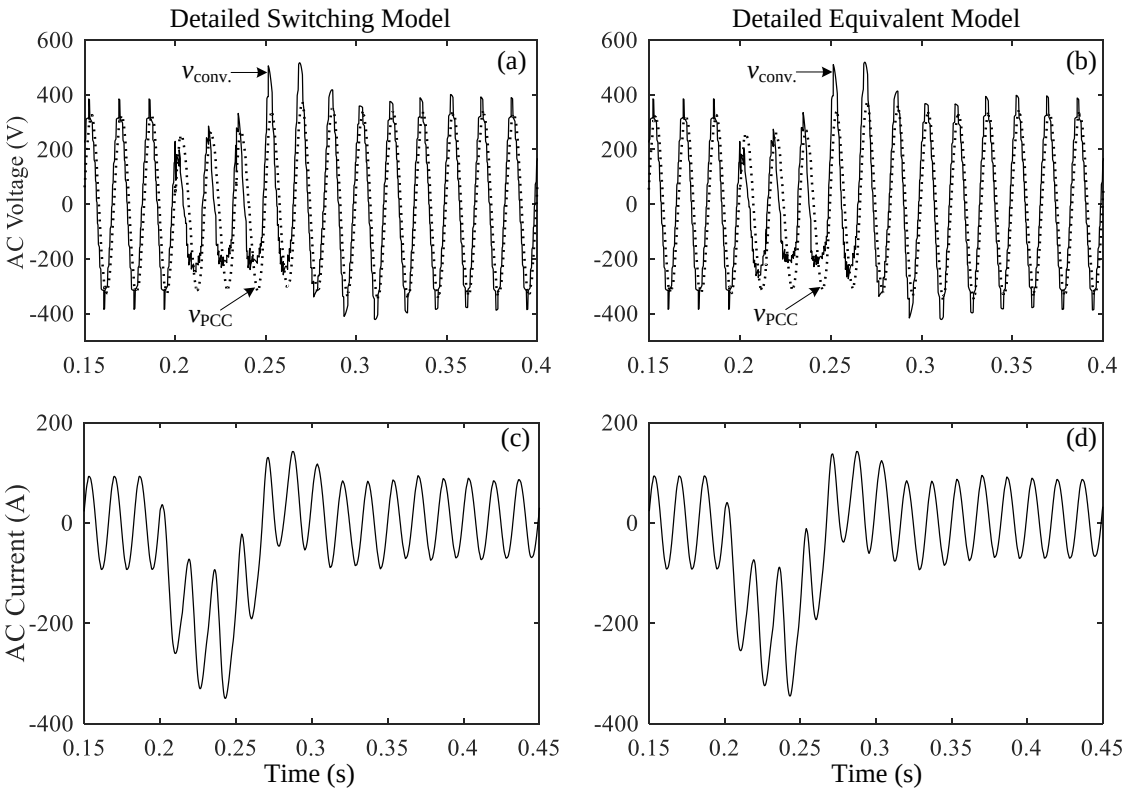


Figure 4.22: Comparison when fault is at the middle of multivalve: (a)-(b) converter voltage ($v_{conv.}$) and PCC voltage (v_{PCC}), (c)-(d) AC current

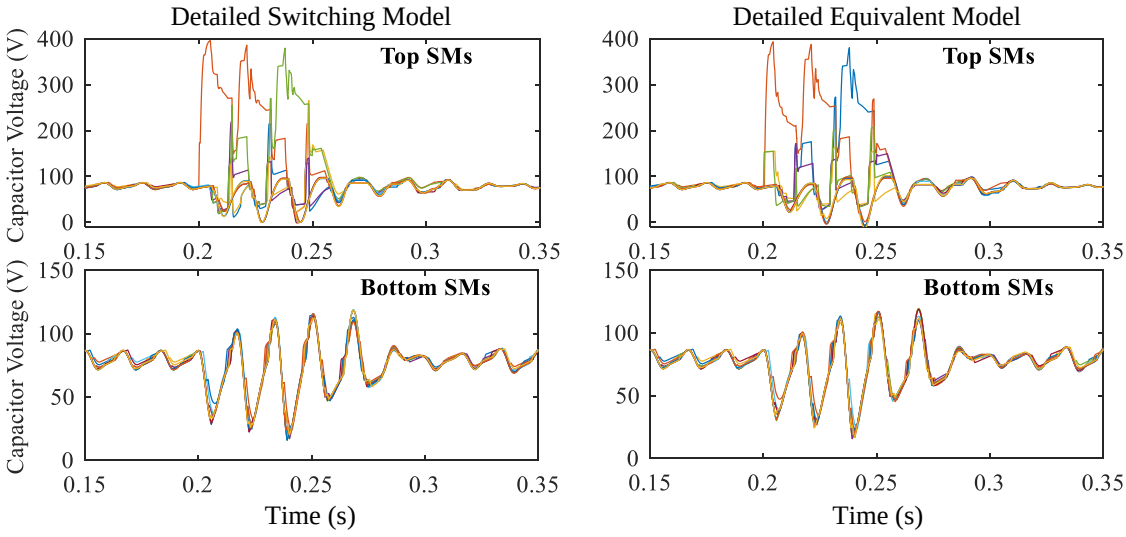


Figure 4.23: Capacitor voltages during a fault in the middle of the multivalve.

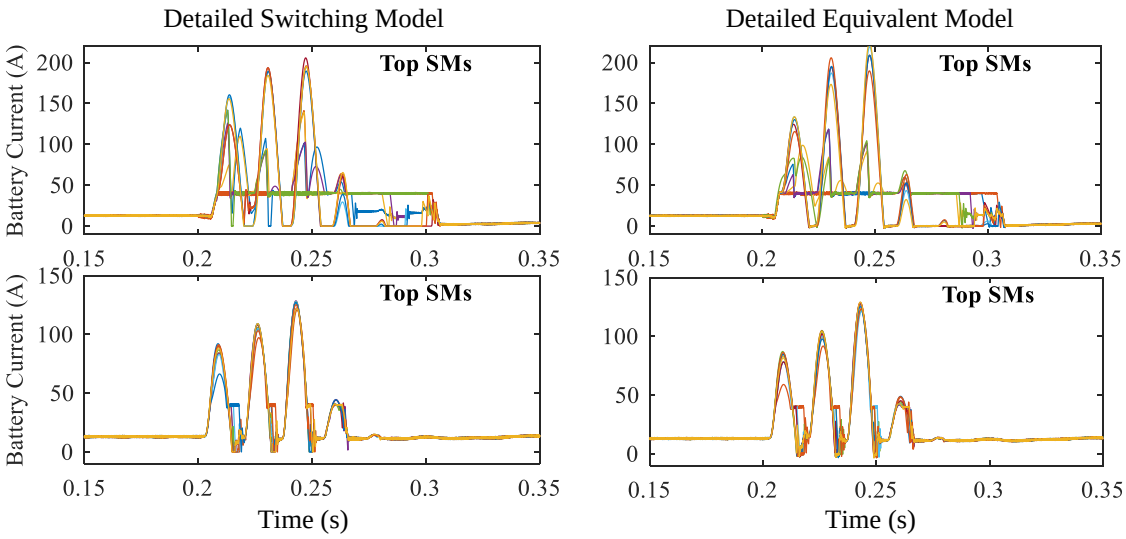


Figure 4.24: Battery currents during a fault in the middle of the multivalve.

For an MMC with embedded storage, this kind of fault is highly unlikely due to the small number of SMs and their physical layout and positioning; however, the simulations done verify that the model is fully able to capture the transients occurring during a fault inside the multivalve.

4.4.5 Comparison of Simulation Speed

The single phase MMC is started using the startup sequence described in Section 3.6 and simulated for a total time of 6 s with 5 µs time step until the MMC reaches steady state. A Lenovo® PC with an Intel® Xenon® X3430 CPU of 2.4 GHz and 16 GB RAM running Windows 7 64-bit operating system is used to compare the simulation speed. The detailed switching model took 928 s to simulate, while the detailed equivalent model only took 191 s to complete. Therefore, the detailed equivalent model has completed the simulations with a speedup factor of 480%.

4.5 Simulation of a Microgrid with an MMC with Embedded Storage

The MMC with energy storage was introduced to the IEEE 34 bus system [39] (Figure 4.25) to observe the impact of the MMC on the system. The MMC is a three-phase 0.6 MVA/0.5 MW system with 106.7 kWh capacity and was interconnected at the bus 844 of the IEEE 34 bus system. A step-up transformer of 2.75 kV/ 24.9 kV was used to interconnect the MMC to the microgrid. A three-phase balanced load of 0.416 + 0.2*j* pu was also connected to bus 844 through a breaker. The full ratings and parameters of the MMC with embedded storage used in this case is shown in Table 4.1.

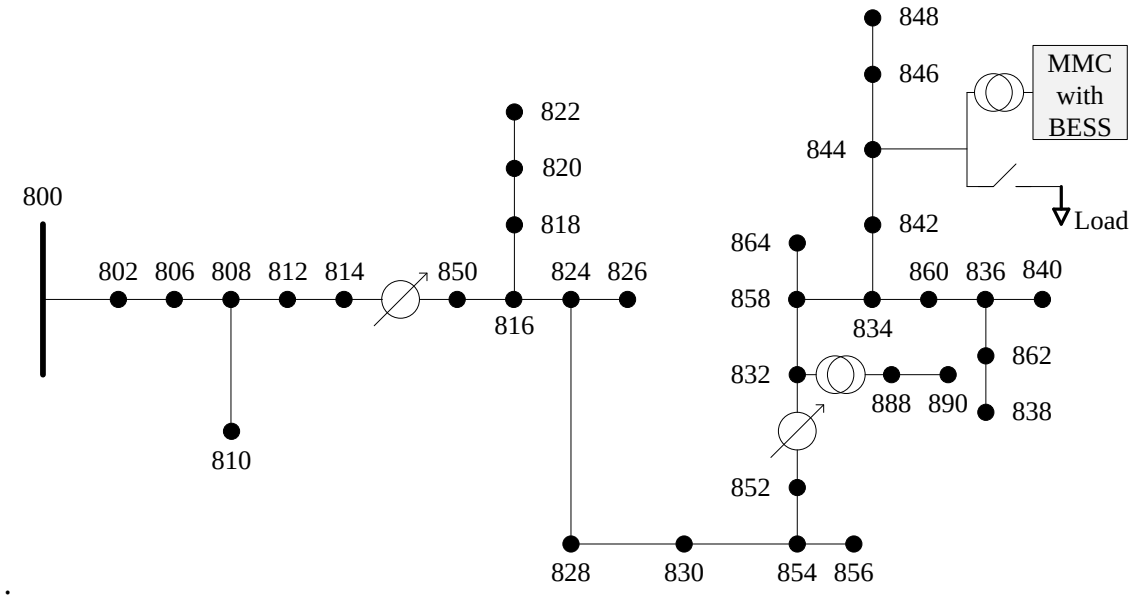


Figure 4.25: IEEE 34 bus system with the proposed MMC with BESS and switchable load.

Table 4.1: Parameters of the MMC with embedded storage

Symbol	Value	Description
$v_{\text{l-l}}$	24.9 kV	Microgrid line to line voltage
U_{DC}	5 kV	DC link voltage
S_{RATED}	0.6 MVA	Rated apparent power
$P_{\text{AC,RATED}}$	0.5 MW	AC rated active power
N	10	Number of SMs per arm
f_{SYS}	60 Hz	AC system frequency
f_{DCDC}	5 kHz	DC-DC converter switching frequency
L_{G}	0.25 pu	Grid interface inductance
L_{A}	0.124 pu	Arm inductance
C_{SM}	3.2 mF	SM capacitance
L_{SM}	7.815 mH	SM DC-DC converter inductance
v_{bat}	273.6 V	Battery nominal voltage
Q_{bat}	6.5 Ah	Energy stored in a battery

4.5.1 Load Energization

The MMC was operated to maintain AC bus voltage of bus 844 at 1.0 pu and supply 0.5 MW of power to the microgrid. After reaching the steady state the load was connected. The voltages of the buses 842, 844, and 846 were observed. This simulation was done with detailed EMT switching model, as well as using the detailed equivalent model. A simulation was also done to observe the voltage variation when the BESS is not available in the grid at the time of switching. Figure 4.26 shows the comparison of voltages achieved from the detailed switching model, detailed equivalent model and the case without BESS.

The BESS improve the voltage in busses when a load is connected. The system arrives at a voltage of 1.0 pu within 0.5 s. The voltage of the busses in the system without the BESS drops

to 0.97 pu. The detailed equivalent model has generated overlapping results to the detailed switching model as well.

4.5.2 Power Reference Change

After the system arrived at steady state, the power reference of the MMC was changed from 0.5 MW to 0.3 MW. The operation of the power controller to control the desired power as well as the voltage controller to regulate the voltage was observed. The case was simulated using detailed switching model as well as using the detailed equivalent model. Figure 4.27 shows the simulation results.

It is seen that the active power is regulated to the reference value in both the detailed switching model as well as in the detailed equivalent model. The ac voltage returns to the set value of 1.0 pu after a short transient due to the operation of the voltage controller.

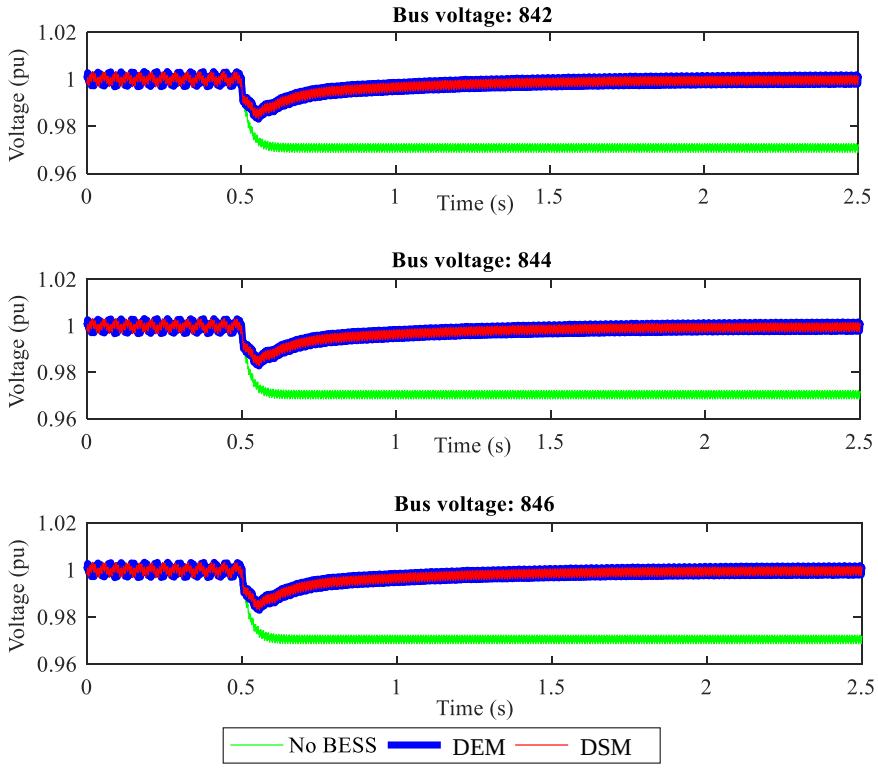


Figure 4.26: Bus voltage at load energization.

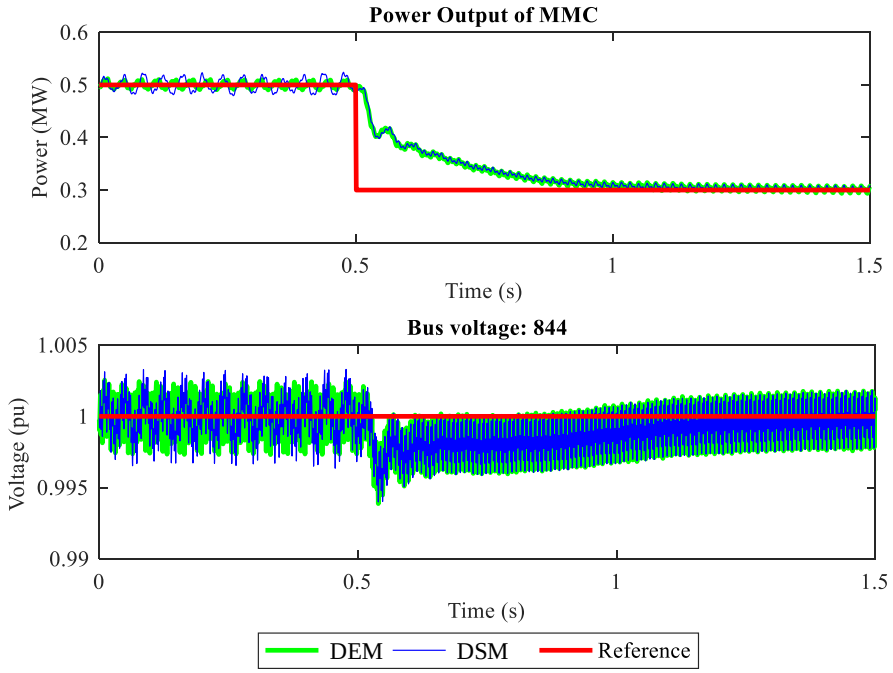


Figure 4.27: Power and voltage when the power reference is changed.

4.5.3 Simulation Efficiency

In the detailed simulation case for the microgrid, the MMC had 240 IGBTs and 240 anti-parallel diodes. Additionally, the microgrid introduces a large number of electrical nodes, which together make the admittance matrix very large. As the switchings occur frequently the re-inversion of the admittance matrix poses a significant computational burden. This is observable as to simulate 10 s of the detailed switching simulation takes 8 hour and 36 mins. The same MMC in the microgrid developed by the detailed equivalent model took only 11 mins 28 s, showing a speed-up factor of exceeding 4650%. Thus the detailed equivalent model is very useful to simulate large systems efficiently.

4.6 Summary

In this chapter, a brief introduction to EMT simulation of electrical networks was given covering basic principles. A battery model was developed for EMT simulation using Shepherds model and an example battery available in the market was used to test and validate the model. Detailed equivalent model of an MMC with embedded energy storage was developed for use in the efficient simulations. The accuracy of the model was verified using simulation of detailed cases developed in PSCAD/EMTDC. Application of the developed model to simulate a three-phase MMC in a microgrid was also shown.

Chapter 5: Experimental Implementation and Verification

5.1 Parameters of the Converter

For the validation of the developed model, an experimental setup of a single phase MMC with embedded energy storage was prepared in the lab. A small-scale model with four SMs per arm is designed to reduce the cost and complexity. The parameters of the converter were derived in a similar manner as described in Appendix B. The experimental setup used in [40] was used as a reference setup. Table 5.1 shows the parameters of the prototype. Figure 5.1 shows the schematic diagram of the experimental setup. Figure 5.2 shows the experimental setup.

Table 5.1: Parameters of the experimental setup.

Symbol	Value	Description
v_{S}	30 V	AC grid voltage
U_{DC}	100 V	DC link voltage
S_{RATED}	300 VA	Rated apparent power
$P_{AC\text{-}RATED}$	250 W	AC rated active power
N	4	Number of SMs per arm
f_{SYS}	60 Hz	AC system frequency
f_{DCDC}	15 kHz	DC-DC converter switching frequency
L_{G}	6.35 mH	AC filter inductance
L_{A}	3.4 mH	Arm inductance
C_{SM}	4.7 mF	SM capacitance
L_{SM}	700 µH	SM DC-DC converter inductance
V_{BAT}	12 V	Battery nominal voltage
Q_{bat}	7.5 Ah	Energy stored in a battery
R_{load}	10 Ω	Load resistor
C_{DC}	2200 µF	DC link capacitor

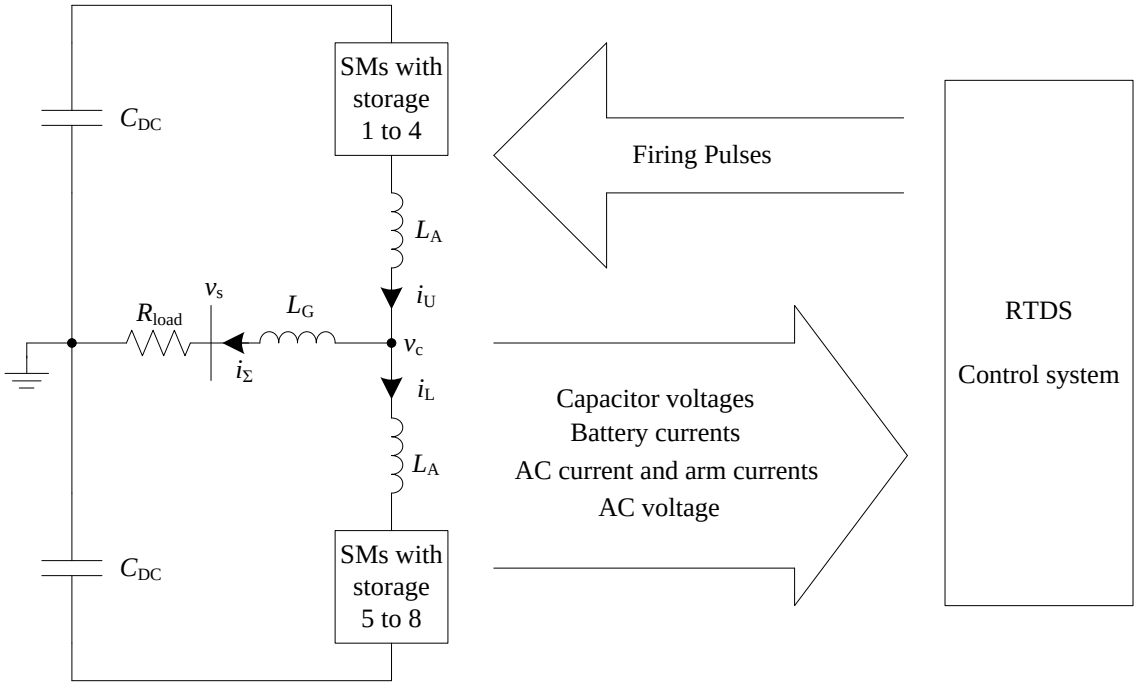


Figure 5.1: Schematic diagram of the prototype

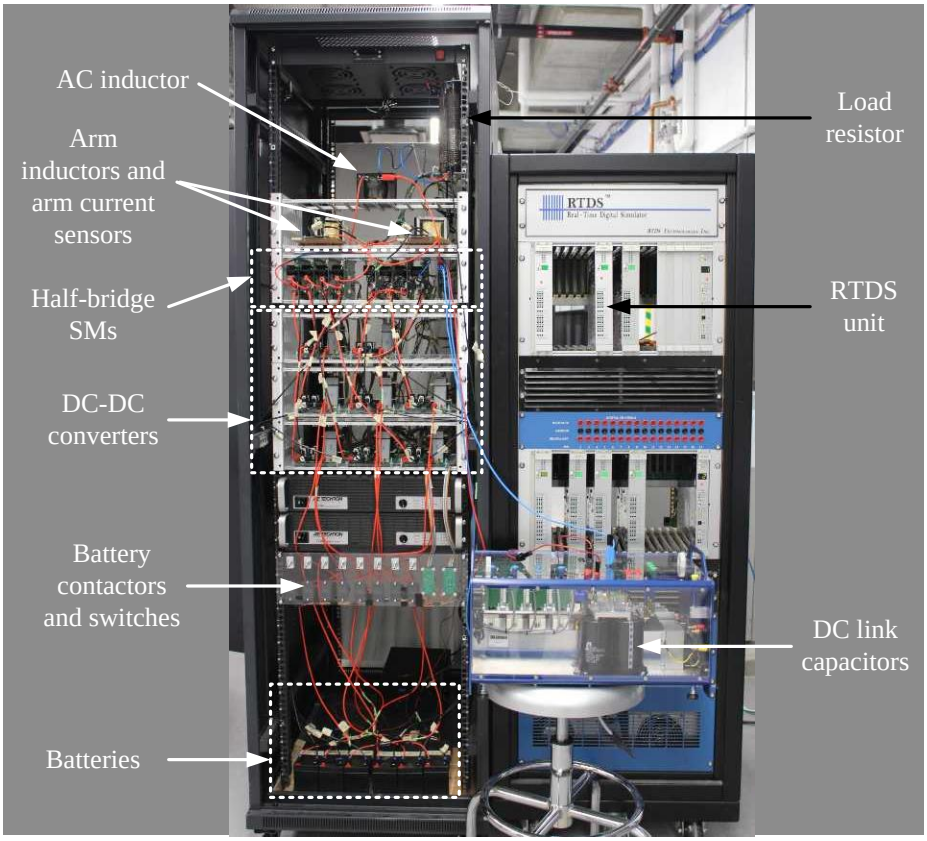


Figure 5.2: Prototype setup

5.2 Half-bridge SM

The half-bridge SMs were available in the lab and were used in a regular MMC (experimental work of Ms. X. Shi). A labeled photo of this SM is shown in Figure 5.3. The SM has two MOSFETs and two diodes, building a half-bridge across a capacitor. The SM circuit has a firing pulse generation circuit for MOSFETs using the logic signal provided from the RTDS. An isolated capacitor voltage measurement circuit is also in place. A mechanism to detect overvoltage in the SM capacitor is also installed and a capacitor discharge circuit is also in place.

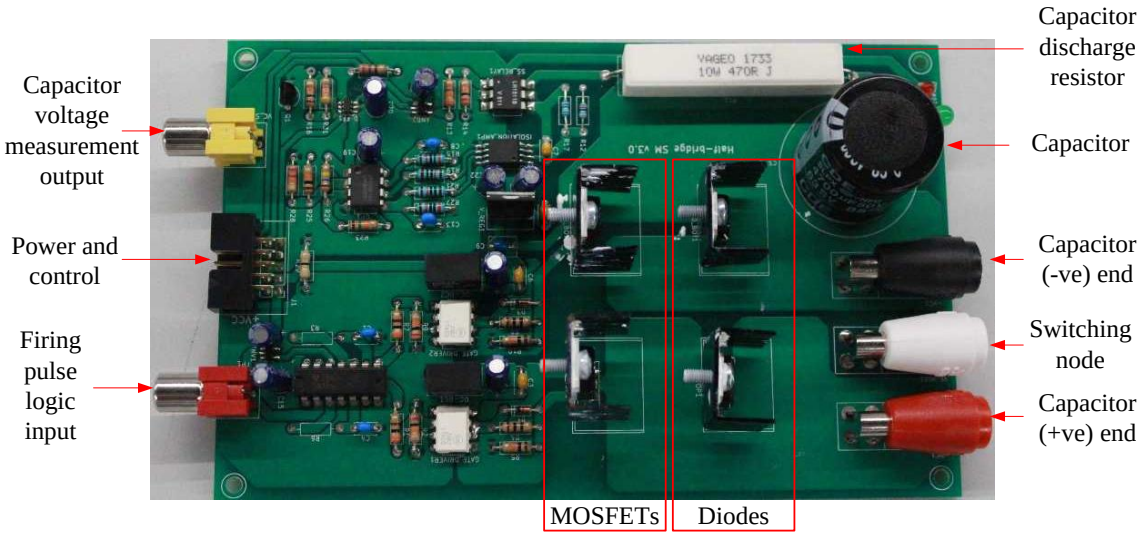


Figure 5.3: Half-bridge SM

5.3 Design of DC-DC converter

The DC-DC converter was designed to connect the battery with each SM. The specifications of a DC-DC converter are shown in Table 5.2.

Table 5.2: DC-DC converter specifications.

Specification	Value
Input voltage	12 V
Output voltage	25 V
Inductor current ripple	10% of the average rated current
Rated power	72 W

The size of the inductance can be reduced when the switching frequency is increased. A smaller inductance is lower in cost and in footprint. However, with the increase in frequency, switching losses, eddy current losses, and resistive losses (due to skin effect) increase. Therefore, 15 kHz was selected as the switching frequency after considering the competing factors.

Reviewing Section 2.4, a relationship between the input voltage (v_{BAT}) and the output voltage (v_{C}) of the DC-DC converter can be obtained by considering the volt-second balance across the inductor in the steady-state. From Figure 2.7(a),

$$v_{\mathrm{BAT}}DT + \left(v_{\mathrm{BAT}} - v_{\mathrm{C}}\right)\left(1-D\right) = 0 \tag{5.1}$$

Simplifying yields

$$\frac{v_{\mathrm{C}}}{v_{\mathrm{BAT}}} = \frac{1}{1-D} \tag{5.2}$$

Thus, steady-state duty ratio (D_{SS}) is given by:

$$D_{\mathrm{SS}} = 1 - \frac{v_{\mathrm{BAT}}}{v_{\mathrm{C}}} = 1 - \frac{12\mathrm{V}}{25\mathrm{V}} = 0.52 \tag{5.3}$$

Considering the power rating of the converter, the average rated input current, $I_{\mathrm{in,avg}}$ (or the average inductor current, $I_{\mathrm{L,avg}}$) can be represented as follows.

$$P_{\mathrm{rated}} = v_{\mathrm{BAT}} \times I_{\mathrm{L,avg}} \tag{5.4}$$

$$I_{\mathrm{L,avg}} = \frac{P_{\mathrm{rated}}}{v_{\mathrm{bat}}} = \frac{72\mathrm{W}}{12\mathrm{V}} = 6\mathrm{A} \tag{5.5}$$

Thus, the allowed inductor current ripple (ΔI_{L}) in the continuous conduction mode (CCM) is given by:

$$\Delta I_{\mathrm{L}} = 10\% \times I_{\mathrm{L,avg}} = 0.6\mathrm{A} \tag{5.6}$$

With the inductor current ripple calculated, the required inductance can be calculated using (2.16). The switching period T is 66.66 µs for a switching frequency of 15 kHz. Equation (5.7) shows (2.16) after substituting the values.

$$L_{SM} = \frac{v_{BAT} DT}{\Delta i_L} = \frac{12\text{V} \times 0.52 \times 66.66 \times 10^{-6}\text{s}}{0.6\text{A}} = 693\mu\text{H} \tag{5.7}$$

Inductors were designed to have an inductance of 700 µH. A Ferrite E-shaped core was selected for the inductor to cater the high DC bias and switching frequency at a low cost. The inductor required 45 turns of AWG 14 wire size to satisfy the required inductance and carry the current. The inductor was designed as per [41]. Appendix C gives a detailed design of the inductor. Figure 5.4 shows a labeled photo of the designed DC-DC converter. The DC-DC converter circuit has an inbuilt firing pulse generation circuit, which generates firing pulses for the two MOSFETS using the firing pulse logic input from RTDS. An isolated inductor current measurement circuit is also installed in the printed circuit board (PCB).

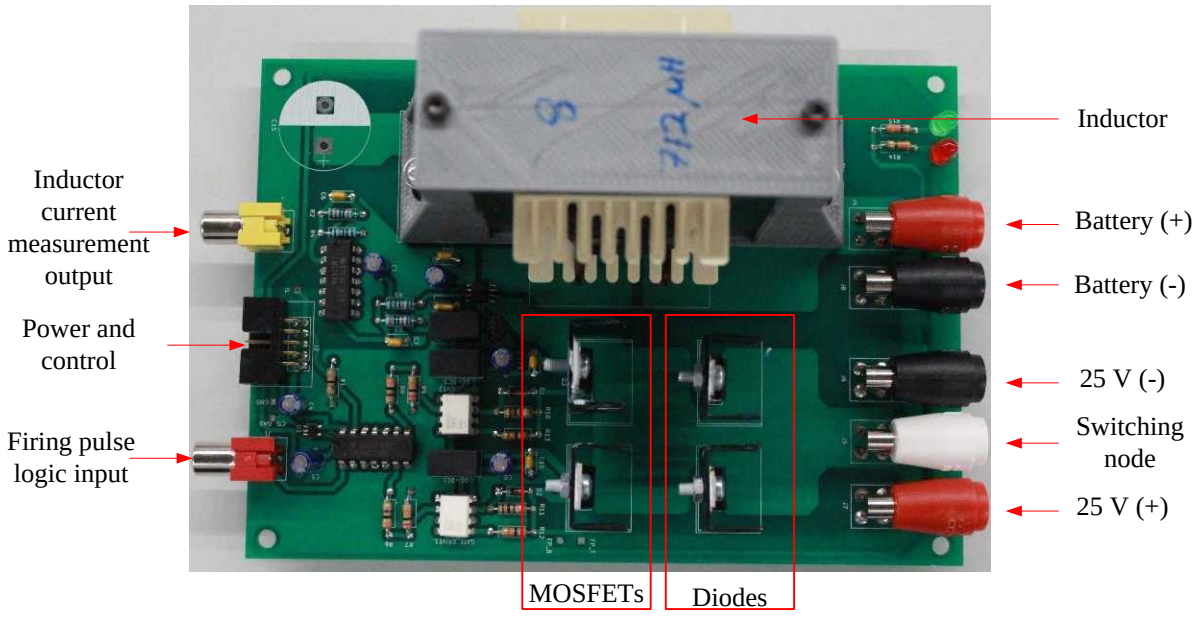
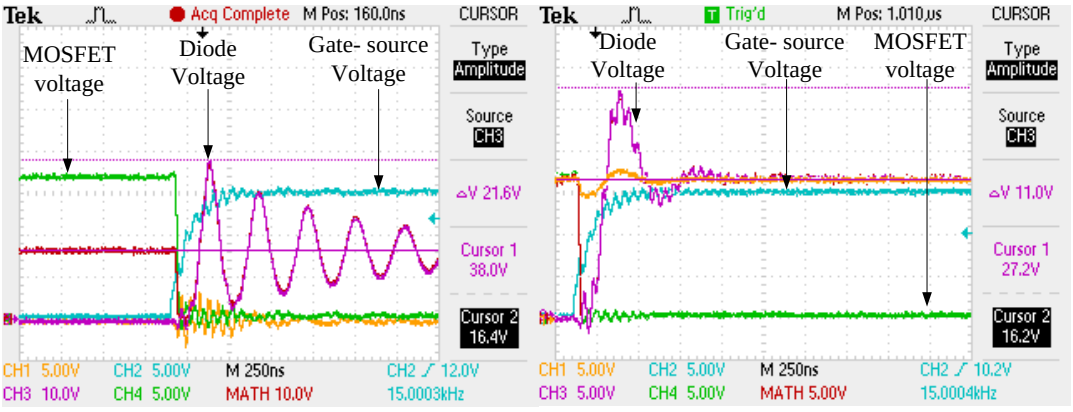


Figure 5.4: DC-DC converter.

5.3.1 Snubber Design

The power electronic switches in the DC-DC converter turn on with a non-zero voltage across them and turn off when current is flowing through them. Thus it is called a hard switched converter. Due to such switching, at turn off the switch observes a large voltage spike across its terminals followed by oscillations. This voltage spike and ripple could be so large it can reach the maximum drain to source voltage ($V_{DS,max}$) of a MOSFET or diode and destroy it. Figure 5.5(a) shows an oscilloscope capture of a diode voltage during its turn off. It can be seen that an overshoot of 38.0 V occurs when the steady state diode voltage is 16.4 V. This peak overshoot further increases when the steady state voltage is at its rated value, which is 25 V. The overshoot is 231% in the captured case and could damage the diode even if the steady-state operating voltage is less than the breakdown voltage when the rated voltage is applied across the switch.

A resistor-capacitor (RC) snubber was designed to reduce the voltage ripple appearing across the switches [42]. Figure 5.5(b) shows the switch voltage after connecting the snubber. It can be seen that the new overshoot is 27.2 V. The overshoot has reduced by 10.8 V and the oscillations die out really fast. For greater performance, RC snubbers were installed in the half-bridge SM as well. Figure 5.6 shows the full SM, after installing RC snubbers.



(a) (b)

Figure 5.5: Diode voltages (a) without snubber (b) with snubber

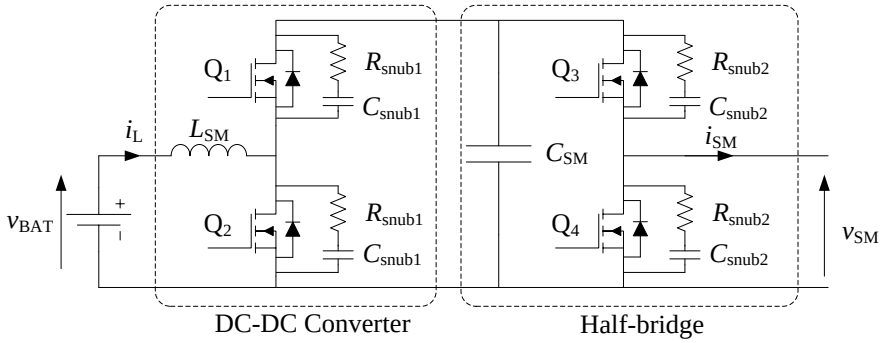
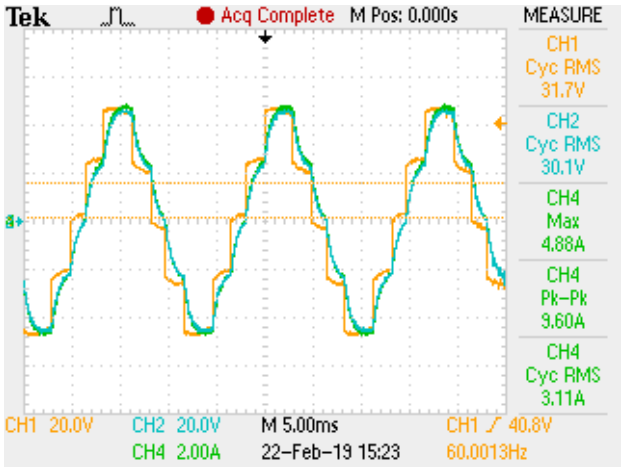


Figure 5.6: SM with the snubbers installed.

Installation of snubbers does not affect the detailed equivalent model developed for EMT simulations. The snubber shows low impedance when the frequency is in MHz range and only during switching transient. EMT simulations do not study the switching transients and thus the snubber can be left out safely from the simulation.

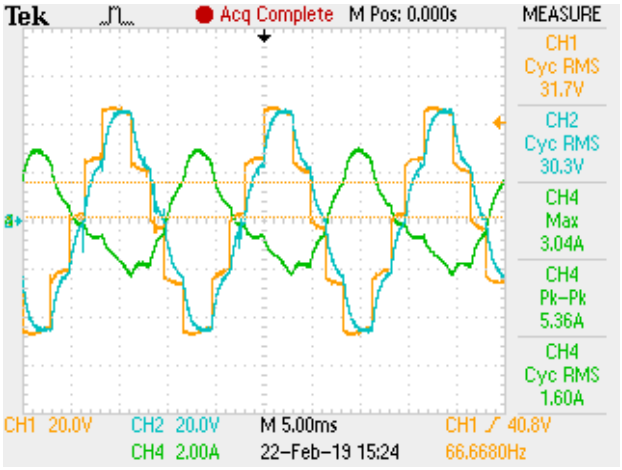
5.4 Observations from the Prototype

The prototype MMC was operated with SM voltage references in DC-DC converter voltage controllers to 25 V and the AC voltage controller reference kept at 30 V rms. The converter was kept to arrive at steady state. Then the following observations were captured.



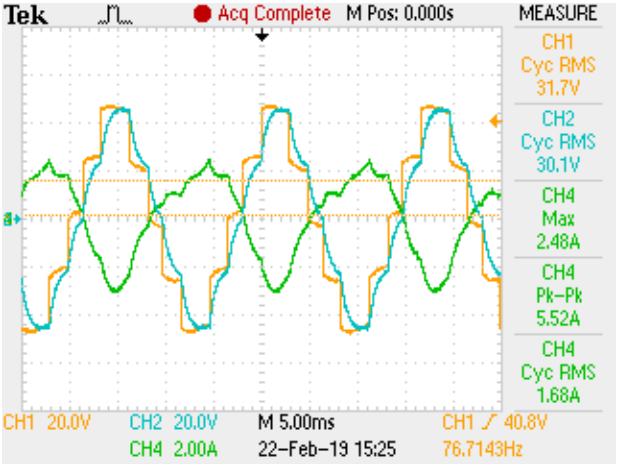
Ch1: MMC terminal voltage (v_c)
Ch2: Load voltage (v_s)
Ch4: AC current (i_Σ)

Figure 5.7: MMC ac voltage, load voltage and load current.



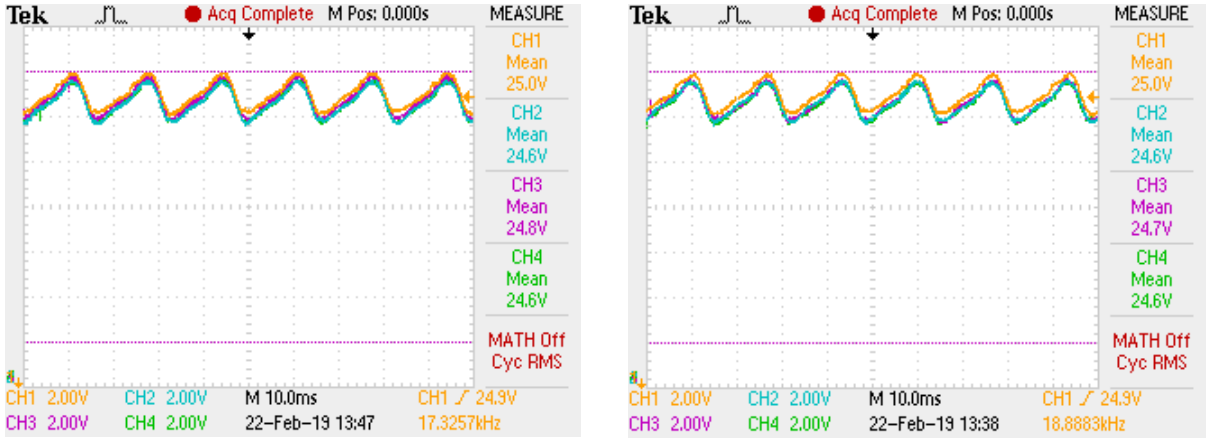
Ch1: MMC terminal voltage (v_c)
Ch2: Load voltage (v_s)
Ch4: Top arm current (i_U)

Figure 5.8: MMC ac voltage, load voltage and top arm current.



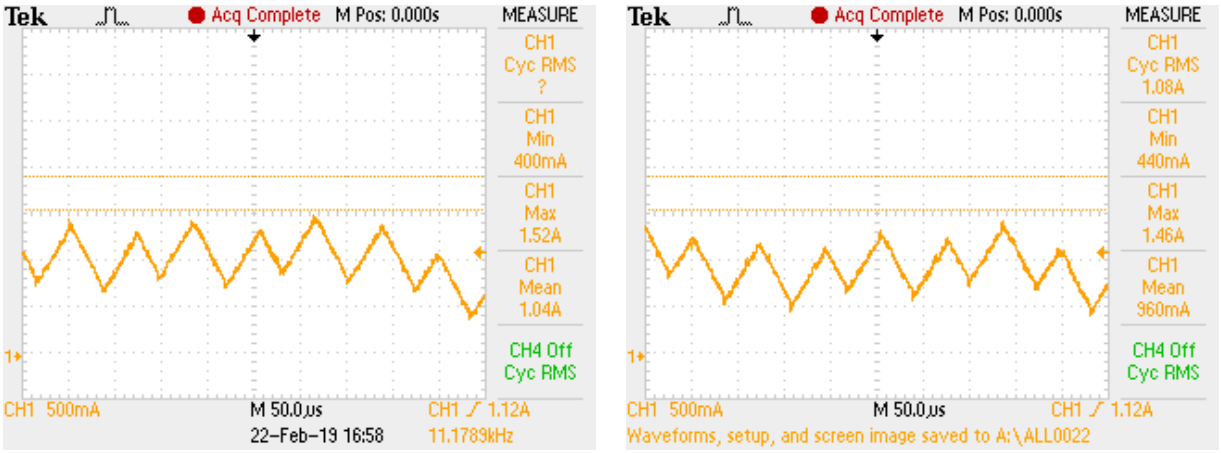
Ch1: MMC terminal voltage (v_c)
Ch2: Load voltage (v_s)
Ch4: Bottom arm current (i_L)

Figure 5.9: MMC ac voltage, load voltage and bottom arm current.



(a) (b)

Figure 5.10: Capacitor voltages (a) top arm (b) bottom arm



(a) (b)

Figure 5.11: Battery currents (a) top arm (b) bottom arm

Figure 5.7 to Figure 5.9 show that the ac voltage is regulated to the desired value and the ac currents are as expected. Figure 5.10 shows that the capacitor voltages are well balanced and at the value given by the reference with a ripple. Battery currents shown in Figure 5.11 shows that equal currents are drawn from batteries in the top arm and bottom arms.

5.5 Comparison of Experimental Results with the EMT Simulation

A PSCAD/EMTDC simulation case was developed to simulate the MMC with energy storage, which was developed as a prototype. The detailed equivalent model developed in this

thesis was used to model the MMC multivalve. Although main parameters used in the simulation were chosen with great care to match the values in the prototype, resistances due to skin effect, resistance from transmission paths, inductor core saturation characteristics, and stray effects were not modeled in the simulation. Figure 5.12 to Figure 5.14 show the comparison of experimental and simulation observations.

The comparison of observations shows that the simulation model was able to capture the steady state operation of the converter accurately. Figure 5.12(a) and (b) compare the AC voltages generated by the MMC. It can be seen that the two waveforms agree well. The widths of the top- and bottom-most steps are larger than the simulation value. This is due to the modulation index correction done by the AC voltage controller to make up for the unmodeled voltage drops. AC current and the two arm currents shown in Figure 5.12(c)-(e) further verify the developed model. The average capacitor voltages shown in Figure 5.13 agrees well with the simulation model.

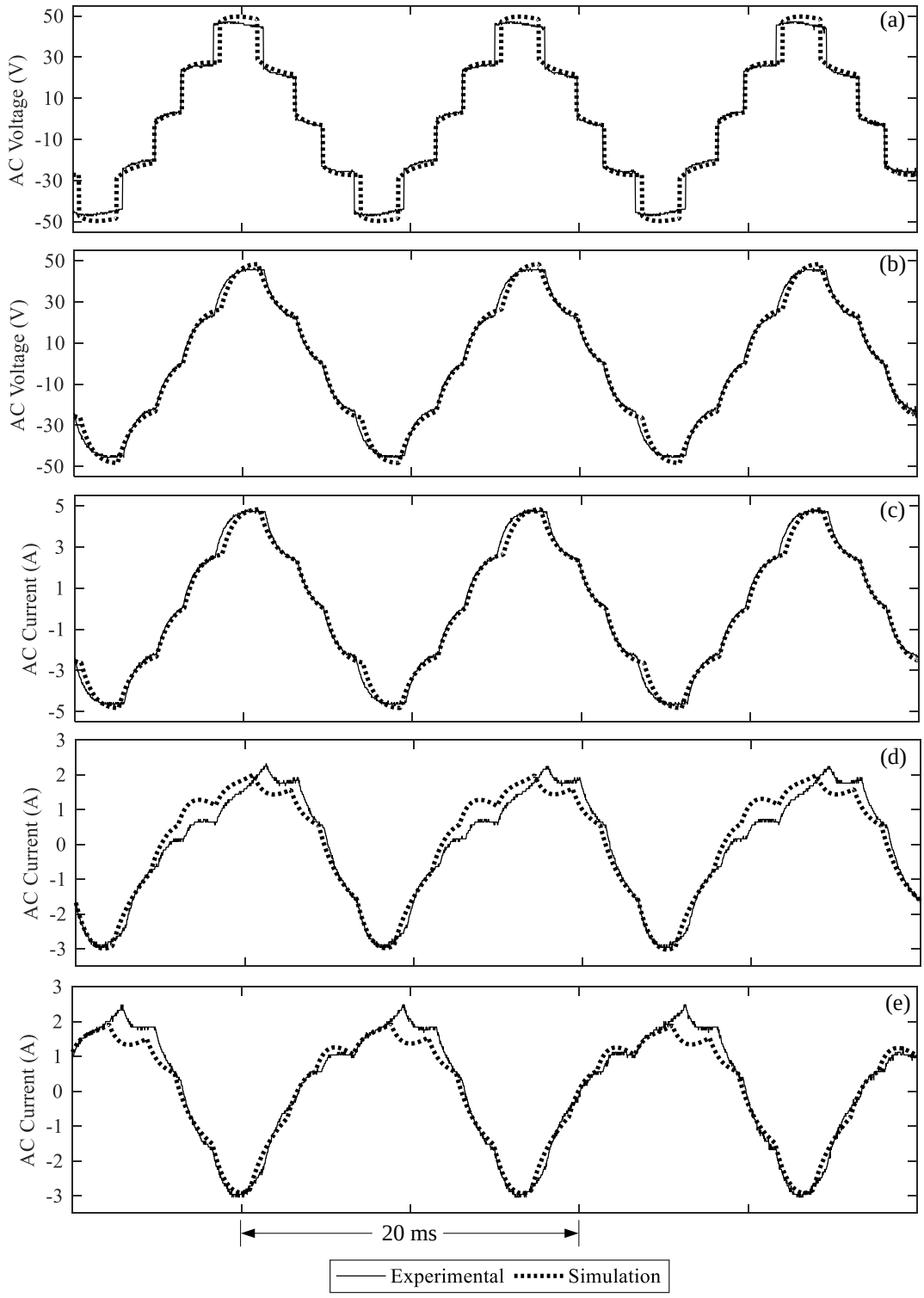


Figure 5.12: Comparison of experimental setup with simulation model: (a) converter voltage (b) load voltage (c) AC current (d) top arm current (e) bottom arm current

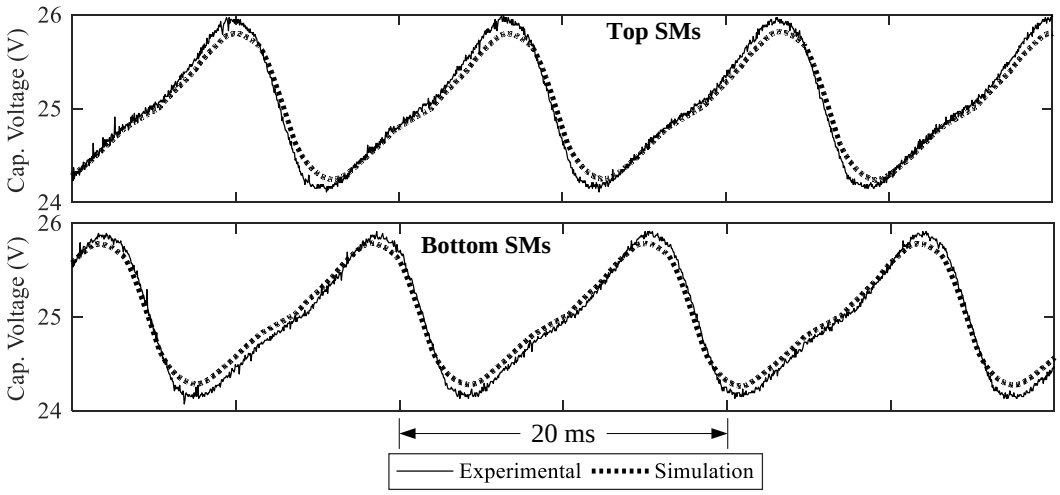


Figure 5.13: Comparison of average capacitor voltages

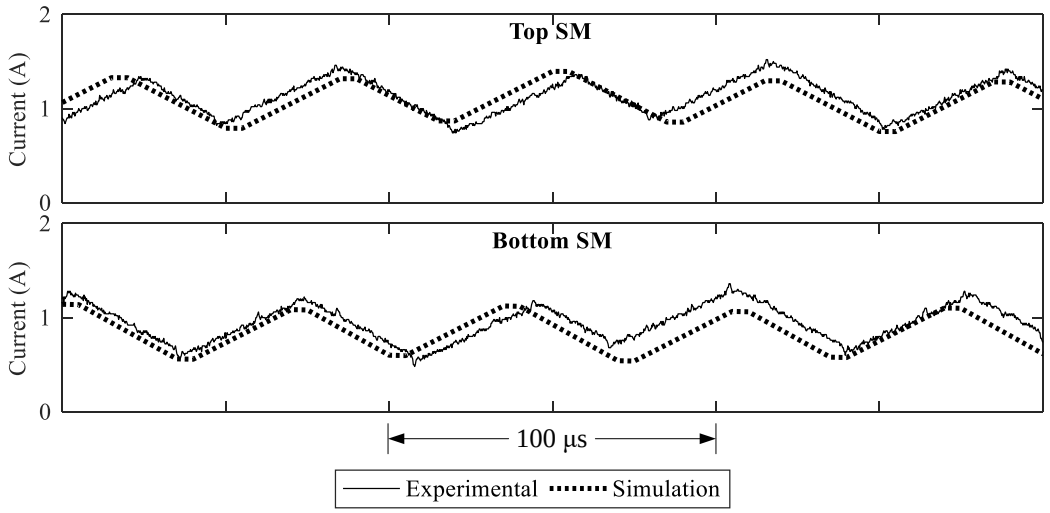


Figure 5.14: Comparison of battery currents.

The experimental battery currents shown in Figure 5.14 follow the simulation to a large extent, but due to the speed of the controllers, and noise captured from the measurements, they tend to deviate slightly. In the simulation model, the skin effect of inductors and the resistance in transmission paths were neglected. Calibration of measurement equipment was done as carefully as possible, to obtain accurate measurements, yet they still impose some error against calibration equipment. Noise is always present in measurement signals. Due to these reasons, slight mismatches can be observed between the results.

5.6 Summary

In this section, development of a prototype MMC with storage was presented. Design of the DC-DC converter was presented in detail. The prototype converter was allowed to arrive at steady state and the AC voltages, AC currents, capacitor voltages, and battery currents were observed. A comparison was done against the experimental observations and PSCAD/EMTDC simulations. The comparison showed that the detailed equivalent model was able to capture the most important parameters in the prototype converter accurately.

Chapter 6: Contributions, Conclusions, and Future work

6.1 Contributions and Conclusions

In this thesis, a novel method to integrate energy storage (battery storage, supercapacitors) using MMC topology was discussed. The power flow of the converter was studied, and the operation and control of the converter were presented. It was observed that due to the complexity of the converter, traditional methods used for EMT simulation of this converter would be greatly inefficient. As a solution, a detailed equivalent model of the multivalve of an MMC with embedded storage was developed.

The developed detailed equivalent model simplifies the multivalve to a single Thevenin equivalent and increases EMT simulation efficiency via reducing the number of switchable nodes, and thus the size of the admittance matrix of the system. Comparison of simulation results obtained from the detailed equivalent model and detailed switching model show that the developed model is accurate and does not lose any information. The model was used to simulate a three-phase MMC with storage in a microgrid. A comparison with the detailed switching model showed a 4700% improvement in simulation time.

A prototype of the MMC with storage was developed to verify the operation of the MMC with energy storage. The experimental observations show that the converter can operate only using the power from batteries in SMs without any net power coming from the DC link. The designed control systems also operated as expected. The comparison of experimental results against simulation results obtained using detailed equivalent model shows that simulation can be used to accurately predict real systems even though most of the stray values, line resistances are not modeled.

The following publications have resulted from the research reported in this thesis. The first paper addresses operating aspects of MMCs with energy storage using a detailed EMT simulation approach; the second one reports the development of the detailed equivalent model and its verification using simulation and experimental work.

[1] N. Herath, M. S. Toulabi, and S. Filizadeh, “Control and operation of a modular multilevel converter with embedded battery energy storage,” in *Proc. CIGRE Canada Conference*, Calgary, AB, Canada, Oct. 15-18, 2018.

[2] N. Herath, M. S. Toulabi and S. Filizadeh, "Modeling of a modular multilevel converter with embedded energy storage for electromagnetic transient simulations," *IEEE Transactions on Energy Conversion* (manuscript submitted for review, TEC-00257-2019)

6.2 Recommendations for Future Work

Interpolation of switching instants has not been implemented in the developed detailed equivalent model. Future research can introduce interpolation to eliminate numerical chatter, which occurs at large time steps. The MMC with embedded storage can be used in a power system to emulate artificial inertia. Future studies can be done using the developed detailed equivalent model to synthesize inertia and study its operation and efficacy. Future researchers could use the developed prototype to connect to an AC grid and test the inertia emulation through hardware-in-loop simulations.

Appendix A Linearization of Boost Converter Model in Continuous Conduction Mode (CCM)

Due to the operation of switches and diodes in a boost converter, a boost converter represents two states in CCM. Figure A.1 shows the two states of the boost converter.

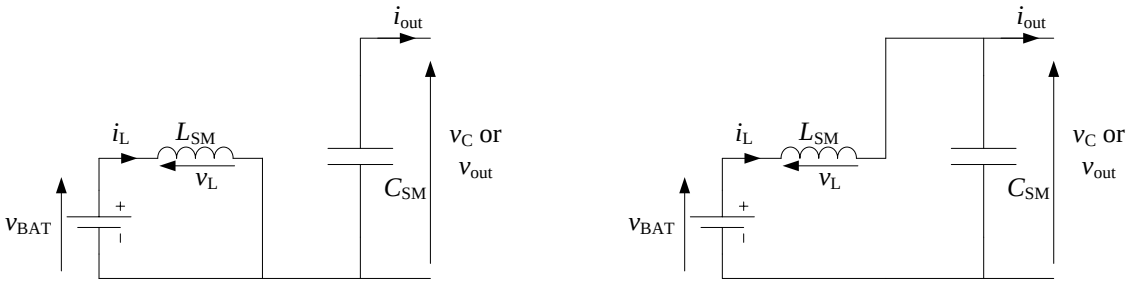


Figure A.1: Two states of the DC-DC converter. (a) switch on, diode off (b) switch off, diode on.

State equations can be written for the inductor and capacitor for the two states as follows.

state (a)

$$L_{SM}\frac{di_L(t)}{dt} = v_{BAT}(t) \tag{A.1}$$

$$C_{SM}\frac{dv_C(t)}{dt} = -i_{out}(t) \tag{A.2}$$

state (b)

$$L_{SM}\frac{di_L(t)}{dt} = v_{BAT}(t) - v_C(t) \tag{A.3}$$

$$C_{SM}\frac{dv_C(t)}{dt} = i_L(t) - i_{out}(t) \tag{A.4}$$

For a duty ratio of $d(t)$ and a switching period of T, state (a) is active for a length of $d(t)T$ and state (b) is active for the remainder of the switching period, i.e., (1- $d(t)$)T. Hence (A.1) to (A.4) can be averaged based on the time period they are active as follows.

$$L_{SM}\frac{di_L(t)}{dt} = v_{BAT}(t) - \big(1-d(t)\big)v_C(t) \tag{A.5}$$

$$C_{SM}\frac{dv_C(t)}{dt} = (1-d(t))i_L(t) - i_{out}(t) \tag{A.6}$$

The variables can be represented as a combination of a DC value (subscript O) and an AC value (denoted by ˜).

$$\begin{aligned} i_L(t) &= I_{L,O} + \tilde{i}_L(t) \\ i_{out}(t) &= I_{out,O} + \tilde{i}_{out}(t) \\ v_{BAT}(t) &= V_{BAT,O} + \tilde{v}_{BAT}(t) \\ v_C(t) &= V_{C,O} + \tilde{v}_C(t) \\ d(t) &= D_O + \tilde{d}(t) \end{aligned} \tag{A.7}$$

substituting the variables in (A.7)

$$L_{SM}\frac{d(I_{L,O} + \tilde{i}_L(t))}{dt} = (V_{BAT,O} + \tilde{v}_{BAT}(t)) - \big(1 - D_O - \tilde{d}(t)\big)(V_{C,O} + \tilde{v}_C(t)) \tag{A.8}$$

$$C_{SM}\frac{d(V_{C,O} + \tilde{v}_C(t))}{dt} = (1 - D_O - \tilde{d}(t))(I_{L,O} + \tilde{i}_L(t)) - (I_{out,O} + \tilde{i}_{out}(t)) \tag{A.9}$$

Considering the DC values only yields

$$L_{SM}\frac{dI_{L,O}}{dt} = V_{BAT,O} - \big(1 - D_O\big)V_{C,O} = 0 \tag{A.10}$$

$$C_{SM}\frac{dV_{C,O}}{dt} = (1 - D_O)I_{L,O} - I_{out,O} = 0 \tag{A.11}$$

Substituting (A.10) and (A.11) in (A.8) and (A.9) and neglecting products of AC values (as the AC values are small) one obtains:

$$L_{\mathrm{SM}} \frac{d\tilde{i}_{\mathrm{L}}(t)}{dt} = \tilde{v}_{\mathrm{BAT}}(t) - (1 - D_{\mathrm{O}})\tilde{v}_{\mathrm{C}}(t) + V_{\mathrm{C,O}}\tilde{d}(t) \tag{A.12}$$

$$C_{\mathrm{SM}} \frac{d\tilde{v}_{\mathrm{C}}(t)}{dt} = (1 - D_{\mathrm{O}})\tilde{i}_{\mathrm{L}}(t) - I_{\mathrm{L,O}}\tilde{d}(t) - \tilde{i}_{\mathrm{out}}(t) \tag{A.13}$$

Eventually, applying Laplace transform to (A.12) and (A.13) results in the following equations.

$$L_{\mathrm{SM}} s I_{\mathrm{L}}(s) = V_{\mathrm{BAT}}(s) - (1 - D_{\mathrm{O}})V_{\mathrm{C}}(s) + V_{\mathrm{C,O}}D(s) \tag{A.14}$$

$$C_{\mathrm{SM}} s V_{\mathrm{C}}(s) = (1 - D_{\mathrm{O}})I_{\mathrm{L}}(s) - I_{\mathrm{L,O}}D(s) - I_{\mathrm{out}}(s) \tag{A.15}$$

Appendix B Selection of Parameters for the MMC with Embedded Storage

For an MMC with energy storage, selection of the number of SMs, SM capacitance, arm inductance, and grid interface inductance are vital for the proper operation of the converter. This appendix gives a guide to select the above parameters.

Number of SMs

The number of SMs per phase should be selected based on the voltage quality required by the user and the maximum allowable capacitor voltage. The voltage and current quality increase with the number of SMs, but the switching losses also increase. A lower number of SMs will comparatively give lower-quality voltages and currents, although they may be improved using appropriate modulation techniques. A main drawback of a low number of SMs is the high capacitor voltage. In a practical implementation, capacitors that can withstand high voltages are expensive and it will increase the total cost of the converter. Equation (B.1) gives the nominal capacitor voltage, where U_{DC} is the pole to pole DC link voltage and N is the number of SMs per arm.

$$v_{\mathrm{C,nom}} = \frac{U_{\mathrm{DC}}}{N} \tag{B.1}$$

SM Capacitance

The SM capacitance is normally determined by the energy stored in the converter for the rated apparent power of the converter. The normal practice is to store 30-40 kJ/MVA in the capacitors.

The energy stored in capacitors for a single-phase converter can be calculated as follows.

$$\text{Energy Stored} = \underbrace{\left(\frac{1}{2} C_{\text{SM}} v_{\text{C,nom}}^2\right)}_{\text{Energy in a capacitor}} \times \underset{\text{Total SMs}}{2N} \tag{B.2}$$

At the same time,

$$\text{Energy stored} = 40\,\text{kJ/MVA} \times S_{\text{rated}} \tag{B.3}$$

The energy to apparent power ratio is taken from 3.68 kJ/MVA to 92.77 kJ/MVA in [13], [40]. The wide range used in the literature suggests starting from a more practical value of 30-40 kJ/MVA and fine tune the capacitance based on EMT simulation results.

Arm Inductance and Grid Interface Inductance

The arm inductance is typically used in the range of 0.3 pu and the grid interface inductance is around 0.2 pu. Tuning of these inductance values can help to limit the circulating currents and current quality.

Appendix C Design of DC-DC Converter Inductor

This section describes the design process of the DC inductor used in the DC-DC converter of the experimental setup. An inductor with an inductance of 700 µH and a current capability of 10 A is designed.

Selection of Inductor Core Material

The inductor is required to be operated at 15 kHz, which is a moderately high frequency. With increasing frequency, the core losses of the inductor increase. Thus, selection of proper core material is vital. Powder, Kool Mu®, and ferrite cores are typically used in this frequency range due to their low losses. Powder and Kool Mu® cores have exceptional performance regarding losses; however, they are quite expensive. Ferrite cores have low core losses (higher than Powder and Kool Mu® cores) but they are less expensive. Thus ferrite is selected as the core material.

Selecting Core Size and Type

Initially, the LI^2 value of the inductor is calculated. L is the inductance in mH with a DC bias and I is the rated maximum DC current.

$$LI^2 = 0.7\text{mH} \times (10\text{A})^2 = 70\text{mJ} \tag{C.1}$$

This LI^2 value is located in ferrite core selector charts available at [41]. The first curve to intersect this LI^2 value denotes the smallest core. For this value, inductor core 46527 is selected in "Lamination size E cores". The core offers an A_L value of 360 mH/1000 turns.

Calculating the Number of Turns

With the knowledge of required inductance and A_L value, the number of turns required in the inductor (N_{turns}) can be calculated.

$$N_{\text{turns}} = 10^3 \times \sqrt{\frac{L}{A_L}} = 44.1\,\text{turns} \tag{C.2}$$

To account for losses, 45 turns are used in the inductor.

Determining the Air Gap

An air gap is required to be maintained in the magnetic path to increase the magnetic reluctance, and thus allow a DC bias without core saturation. The gap length can be calculated by initially calculating the effective permeability (μ_e) of the core as in (C.3).

$$\mu_e = \frac{A_L l_e}{4\pi A_e} \tag{C.3}$$

Here l_e is the magnetic path length (in centimeter) and A_e is the effective cross-sectional area in cm^2. For the core 46527, l_e is 14.7 cm and A_e is 5.3 cm^2. An effective permeability of 79.46 is achieved for this core.

The air gap can be calculated by determining the equivalent reluctance ($\Re$) of the magnetic path. The relationship between core parameters and reluctance is shown in (C.4) and the equivalent reluctance is calculated in (C.5) and (C.6)

$$\Re = \frac{l_e}{\mu A_e} \tag{C.4}$$

for the magnetic path with a series air gap and an initial permeability of μ_i

$$\Re_{eq} = \Re_{core} + \Re_{gap}$$

$$\frac{l_e + l_g}{\mu_e \mu_0 A_e} = \frac{l_e}{\mu_i \mu_0 A_e} + \frac{l_g}{\mu_0 A_e} \tag{C.5}$$

simplifying and $l_g << l_e$

$$\frac{1}{\mu_e} = \frac{1}{\mu_i} + \frac{l_g}{l_e} \tag{C.6}$$

The core 46527 has a μ_i of 2500. Thus the calculated air gap is 1.79 mm.

References

[1] E. N. Foster and F. J. Parker, “Hydro-electric machines,” *IEE Proc. C - Transm. Distrib. Gener.*, vol. 133, no. 3, pp. 126–136, Apr. 1986.

[2] "RENEWABLES 2018 GLOBAL STATUS REPORT", Ren21.net, 2019. [Online]. Available: http://www.ren21.net/gsr-2018. [Accessed: 23-Aug-2018].

[3] W. Su, J. Wang, and J. Roh, “Stochastic energy scheduling in microgrids with intermittent renewable energy resources,” *IEEE Trans. Smart Grid*, vol. 5, no. 4, pp. 1876–1883, Jul. 2014.

[4] Y. Ghiassi-Farrokhfal, S. Keshav, C. Rosenberg, and F. Ciucu, “Solar power shaping: an analytical approach,” *IEEE Trans. Sustain. Energy*, vol. 6, no. 1, pp. 162–170, Jan. 2015.

[5] R. Karki, P. Hu, and R. Billinton, “A simplified wind power generation model for reliability evaluation,” *IEEE Trans. Energy Convers.*, vol. 21, no. 2, pp. 533–540, Jun. 2006.

[6] H. Gu, R. Yan, and T. K. Saha, “Minimum synchronous inertia requirement of renewable power systems,” *IEEE Trans. Power Syst.*, vol. 33, no. 2, pp. 1533–1543, Mar. 2018.

[7] J. Harasawa and T. Ikegami, “Load leveling effects by massively introduced residential battery storage systems,” in *Proc. IEEE Innovative Smart Grid Technologies - Asia (ISGT-Asia)*, Auckland, New Zealand, 2017, pp. 1–6.

[8] H. Mahmood, D. Michaelson, and J. Jiang, “A power management strategy for PV/battery hybrid systems in islanded microgrids,” *IEEE J. Emerg. Sel. Top. Power Electron.*, vol. 2, no. 4, pp. 870–882, Dec. 2014.

[9] S. J. Hossain, T. G. Paul, R. Bisht, A. Suresh, and S. Kamalasadan, “An integrated battery optimal power dispatch architecture for end-user-driven microgrid in islanded and grid-connected mode of operation,” *IEEE Trans. Ind. Appl.*, vol. 54, no. 4, pp. 3806–3819, Jul. 2018.

[10] D. Bazargan, S. Filizadeh, and A. M. Gole, “Stability analysis of converter-connected battery energy storage systems in the grid,” *IEEE Trans. Sustain. Energy*, vol. 5, no. 4, pp. 1204–1212, Oct. 2014.

[11] C. Kim, M. Kim, H. Park, and G. Moon, “A modularized two-stage charge equalizer with cell selection switches for series-connected lithium-ion battery string in an HEV,” *IEEE Trans. Power Electron.*, vol. 27, no. 8, pp. 3764–3774, Aug. 2012.

[12] A. Lesnicar and R. Marquardt, “An innovative modular multilevel converter topology suitable for a wide power range,” in *Proc. IEEE PowerTech Conference*, Bologna, 2003, vol. 3, pp. 6 pp. Vol.3-.

[13] T. Soong and P. W. Lehn, “Internal power flow of a modular multilevel converter with distributed energy resources,” *IEEE J. Emerg. Sel. Top. Power Electron.*, vol. 2, no. 4, pp. 1127–1138, Dec. 2014.

[14] T. Soong and P. W. Lehn, “Evaluation of emerging modular multilevel converters for BESS applications,” *IEEE Trans. Power Deliv.*, vol. 29, no. 5, pp. 2086–2094, Oct. 2014.

[15] I. Trintis, S. Munk-Nielsen, and R. Teodorescu, “A new modular multilevel converter with integrated energy storage,” in *Proc. Annual Conference of the IEEE Industrial Electronics Society (IECON)*, Melbourne, VIC, Australia, 2011, pp. 1075–1080.

[16] R. Mo and H. Li, “Hybrid energy storage system with active filter function for shipboard MVDC system applications based on isolated modular multilevel DC/DC converter,” *IEEE J. Emerg. Sel. Top. Power Electron.*, vol. 5, no. 1, pp. 79–87, Mar. 2017.
[17] Y. Wu, C. Gao, X. Liu, Z. Chen, and X. Mao, “A power router based on modular multilevel converter integrating ultracapacitor energy storage system,” in *Proc. International Conference on Electrical Machines and Systems (ICEMS)*, Sydney, Australia, 2017, pp. 1–6.
[18] U. N. Gnanarathna, A. M. Gole, and R. P. Jayasinghe, “Efficient modeling of modular multilevel HVDC converters (MMC) on electromagnetic transient simulation programs,” *IEEE Trans. Power Deliv.*, vol. 26, no. 1, pp. 316–324, Jan. 2011.
[19] Qingrui Tu, Zheng Xu, H. Huang and Jing Zhang, "Parameter design principle of the arm inductor in modular multilevel converter based HVDC," in *Proc. International Conference on Power System Technology (POWERCON)*, Hangzhou, China, 2010, pp. 1-6.
[20] T. Soong and P. W. Lehn, “Assessment of fault tolerance in modular multilevel converters with integrated energy storage,” *IEEE Trans. Power Electron.*, vol. 31, no. 6, pp. 4085–4095, Jun. 2016.
[21] L. Huang *et al.*, “The evolution and variation of sub-module topologies with DC-fault current clearing capability in MMC-HVDC,” in *Proc. IEEE International Future Energy Electronics Conference and ECCE Asia (IFEEC - ECCE Asia)*, Kaohsiung, Taiwan, 2017, pp. 1938–1943.
[22] S. Debnath, J. Qin, B. Bahrani, M. Saeedifard, and P. Barbosa, “Operation, control, and applications of the modular multilevel converter: a review,” *IEEE Trans. Power Electron.*, vol. 30, no. 1, pp. 37–53, Jan. 2015.
[23] M. Saeedifard and R. Iravani, “Dynamic performance of a modular multilevel back-to-back HVDC system,” *IEEE Trans. Power Deliv.*, vol. 25, no. 4, pp. 2903–2912, Oct. 2010.
[24] M. Hagiwara and H. Akagi, “Control and experiment of pulsewidth-modulated modular multilevel converters,” *IEEE Trans. Power Electron.*, vol. 24, no. 7, pp. 1737–1746, Jul. 2009.
[25] F. Deng and Z. Chen, “A control method for voltage balancing in modular multilevel converters,” *IEEE Trans. Power Electron.*, vol. 29, no. 1, pp. 66–76, Jan. 2014.
[26] J. Qin and M. Saeedifard, “Predictive control of a modular multilevel converter for a back-to-back HVDC system,” *IEEE Trans. Power Deliv.*, vol. 27, no. 3, pp. 1538–1547, Jul. 2012.
[27] R. H. Park, “Two-reaction theory of synchronous machines generalized method of analysis-part I,” *Trans. Am. Inst. Electr. Eng.*, vol. 48, no. 3, pp. 716–727, Jul. 1929.
[28] N. Herath, P. Binduhewa, L. Samaranayake, J. Ekanayake, and S. Longo, “Design of a dual energy storage power converter for a small electric vehicle,” in *Proc. IEEE International Conference on Industrial and Information Systems (ICIIS)*, Peradeniya, Sri Lanka, 2017, pp. 1–6.
[29] P. J. Binduhewa, “Microsource interface for a microgrid,” *[Ph.D Thesis]. Manchester, UK: The University of Manchester; 2010.*, 08-Jul-2010. [Online]. Available: https ://www.escholar.manchester.ac.uk/uk-ac-man-scw:86106. [Accessed: 17-Jan-2018].
[30] Q. Chen, R. Li, and X. Cai, “Analysis and fault control of hybrid modular multilevel converter with integrated battery energy storage system,” *IEEE J. Emerg. Sel. Top. Power Electron.*, vol. 5, no. 1, pp. 64–78, Mar. 2017.
[31] S. Howell, S. Filizadeh, and A. M. Gole, “Unidirectional HVDC topology with DC fault ride-through capability,” *Can. J. Electr. Comput. Eng.*, vol. 40, no. 1, pp. 41–49, 2017.

[32] H. W. Dommel, “Digital computer solution of electromagnetic transients in single-and multiphase networks,” *IEEE Trans. Power Appar. Syst.*, vol. PAS-88, no. 4, pp. 388–399, Apr. 1969.
[33] H. W. Dommel and N. Sato, “Fast transient stability solutions,” *IEEE Trans. Power Appar. Syst.*, vol. PAS-91, no. 4, pp. 1643–1650, Jul. 1972.
[34] C.-W. Ho, A. Ruehli, and P. Brennan, “The modified nodal approach to network analysis,” *IEEE Trans. Circuits Syst.*, vol. 22, no. 6, pp. 504–509, Jun. 1975.
[35] “Measuring State-of-charge - Battery University.” [Online]. Available: https://batteryuniversity.com/learn/article/how_to_measure_state_of_charge. [Accessed: 19-Nov-2018].
[36] A. A. H. Hussein and I. Batarseh, “An overview of generic battery models,” in *Proc. IEEE Power and Energy Society General Meeting*, Detroit, MI, USA, 2011, pp. 1–6.
[37] O. Tremblay, L. A. Dessaint, and A. I. Dekkiche, “A generic battery model for the dynamic simulation of hybrid electric vehicles,” in *Proc. IEEE Vehicle Power and Propulsion Conference*, Arlington, TX, USA, 2007, pp. 284–289.
[38] E. Raszmann, K. Baker, Y. Shi, and D. Christensen, “Modeling stationary lithium-ion batteries for optimization and predictive control,” in *Proc. IEEE Power and Energy Conference at Illinois (PECI)*, Champaign, IL, USA, 2017, pp. 1–7.
[39] “Resources | PES Test Feeder.” [Online]. Available: http://sites.ieee.org/pes-testfeeders/resources/. [Accessed: 16-Feb-2019].
[40] M. Vasiladiotis and A. Rufer, “Analysis and control of modular multilevel converters with integrated battery energy storage,” *IEEE Trans. Power Electron.*, vol. 30, no. 1, pp. 163–175, Jan. 2015.
[41] “Magnetics - Ferrite Cores.” [Online]. Available: https://www.mag-inc.com/Products/Ferrite-Cores. [Accessed: 29-Sep-2018].
[42] “Resistor-Capacitor (RC) Snubber Design for Power Switches | DigiKey.” [Online]. Available: https://www.digikey.ca/en/articles/techzone/2014/aug/resistor-capacitor-rc-snubber-design-for-power-switches. [Accessed: 24-Feb-2019]